BESSY

Highlights 2005

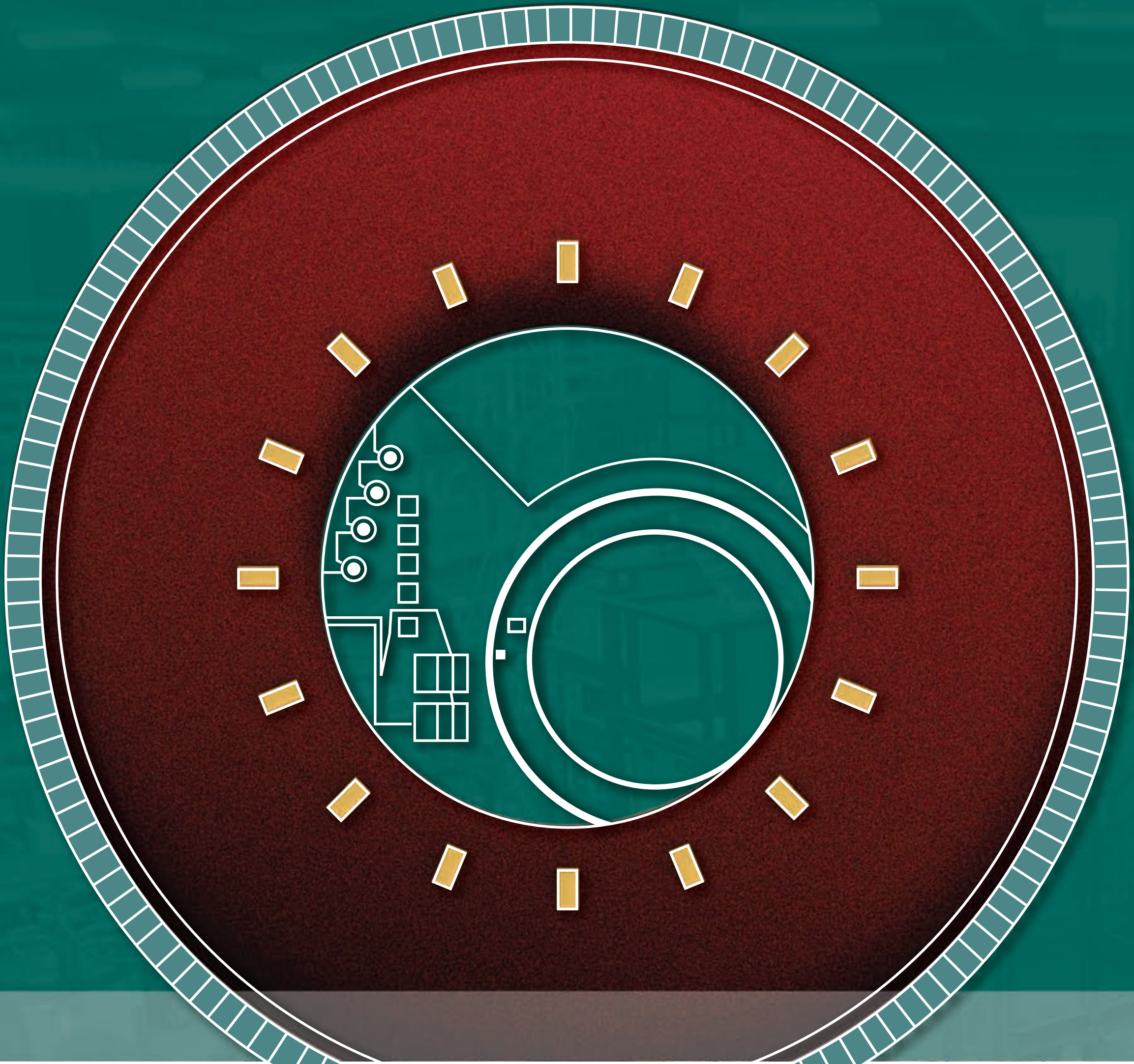

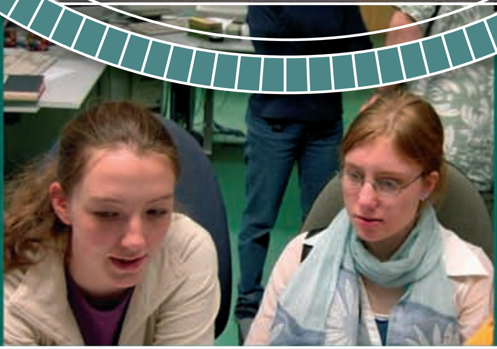

Berliner Elektronenspeicherring-Gesellschaft für Synchrotronstrahlung m.b.H.

Member of the Leibniz Association

Published by:
Berliner Elektronenspeicherring-Gesellschaft für
Synchrotronstrahlung m.b.H. – BESSY

Albert-Einstein-Straße 15
12489 Berlin, Germany
phone +49 (0)30 / 6392 2999
fax +49 (0)30 / 6392 2990

www.bessy.de
info@bessy.de

Board of Directors:
Prof. Dr. Dr. h.c. Wolfgang Eberhardt,
Prof. Dr. Eberhard Jaeschke,
Thomas Frederking

Editors:
Dr. Heike Henneken,
Dr. Markus Sauerborn

Layout:
Annette Weber
Stitz & Betz GmbH

ISSN Number: 1611-6127

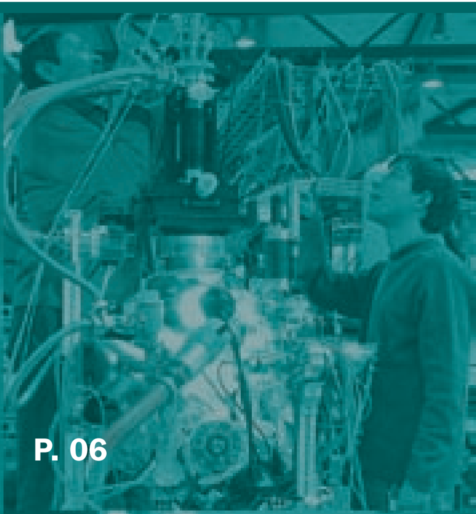

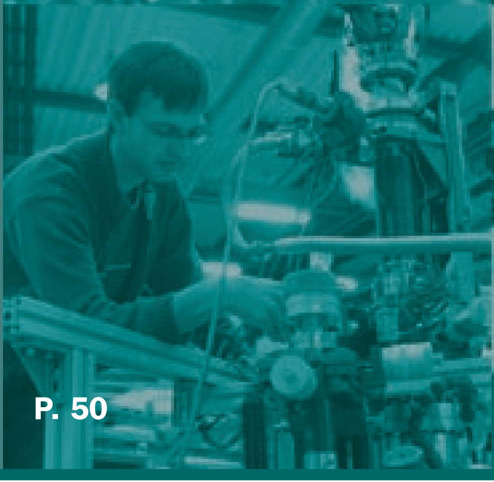

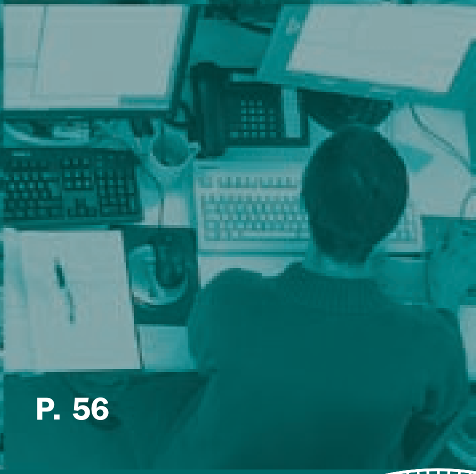

Berliner Elektronenspeicherring-Gesellschaft für Synchrotronstrahlung m.b.H.

Member of the Leibniz Association

Content

Introduction

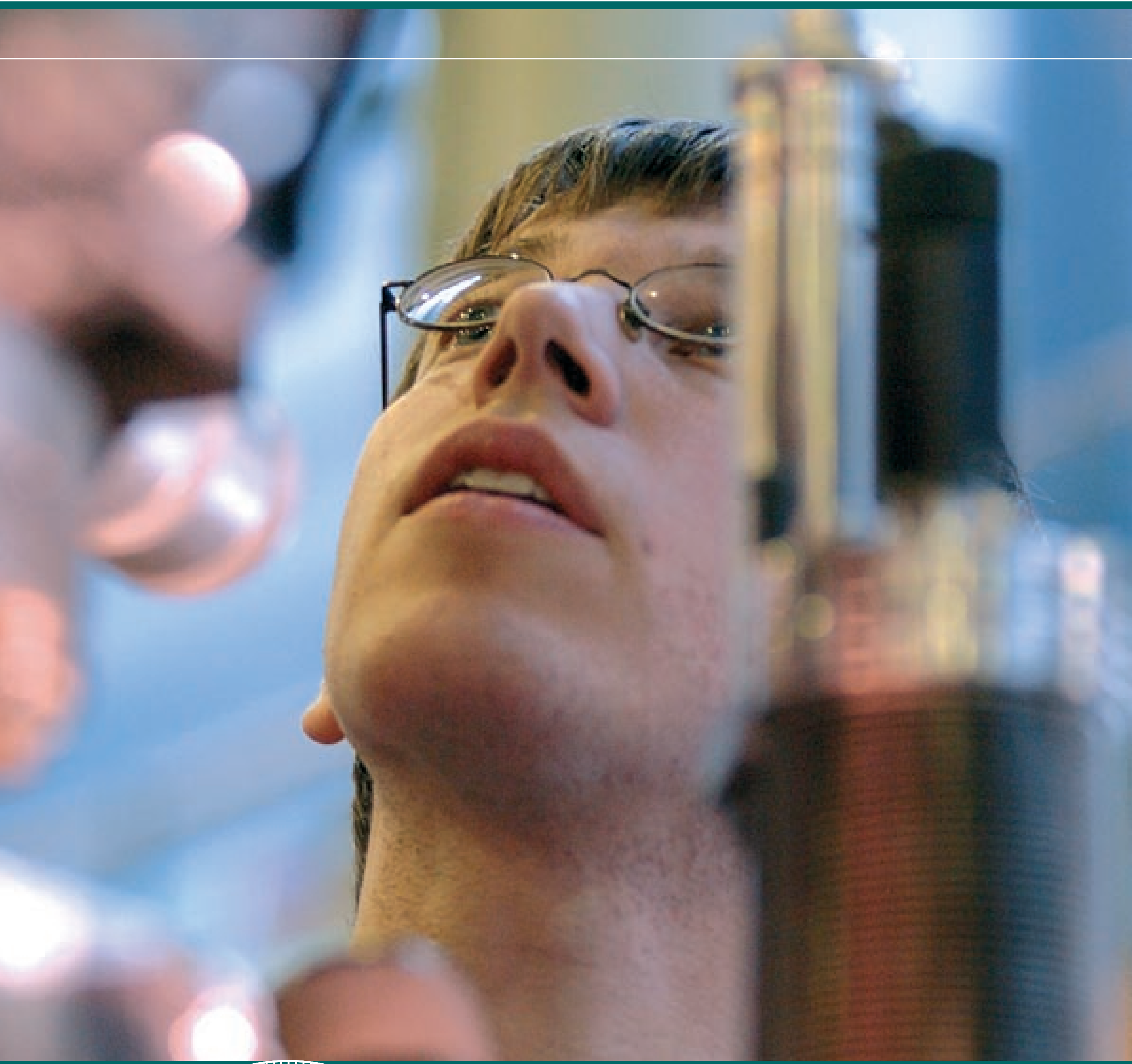

BESSY Inside

‘Physics is not one of the favorite subjects of German school children!’ titled a newspaper recently. This is not a surprise. It probably never was during the last decades – but it became more apparent that physics education in schools and pre-schools is lacking time, interest and enthusiasm. This is a dramatic issue also for a scientific institution such as BESSY, since science needs well educated students. For the realization of our future plans, like our soft X-ray Free Electron Laser, we also need clever new scientists ready to eagerly venture into new fields and address entirely new scientific questions.

In order to involve the public especially young people more in science and what scientists do, several initiatives have been started in recent years reaching back to the Year of Physics in 2000 and finding another climax celebrating the centennial of Einstein’s ‘magic five papers’ in 1905. During this ‘Einstein Year’, BESSY was involved in manifold activities. We demonstrated the photoelectric effect with hands-on experiments on the exhibition ship MS Einstein. The exhibition ‘Highlights der Physik’ and likewise the events ‘Lange Nacht der Wissenschaften’ and ‘Physik zum Frühstück’ had a focus on Einstein’s work. The television science programme – ‘nano’- visited Adlershof with their ‘nanoCamper’, an group of twelve selected high school students who were introduced to the daily work of scientists. At their day at BESSY they took control of the machine, injecting electrons in the storage ring and kicking them out afterwards. They crystallized proteins and built a 3D protein model from scratch, and they learned about non-destructive material analysis using X-rays. Every event has been very successful and we feel encouraged to keep on introducing children and students of all age into the fascinating world of physics, chemistry and biology.

That even ‘good old’ school and textbook science can be exciting, especially when this science is revamped by the use of new experimental evidence has been shown by Uwe Becker’s group from Fritz-Haber-Institute. They downsized the classical double slit experiment onto atomic scale leaving electrons ‘in doubt’ of their state of origin (see Highlights). This is only one of the exciting research results obtained by our steadily increasing user community.

'Einstein enthusiasts' at BESSY and 'NanoCampers' in Adlershof

There is good news for our current and future users. The construction of the Willy-Wien-Labor is proceeding with the new Metrology Light Source of the PTB which will start operations in 2007. BESSY itself passed the stringent evaluation of the Leibniz Association with flying colors in the year 2005 and we are very pleased that following the positive evaluation report we received funding to hire more desperately needed beamline scientists to improve our user support.

Finally, we would like to thank all our users and staff members who through their efforts and dedication made 2005 yet another successful year. Enjoy browsing through the Highlights 2005.

Prof. Dr. Dr. h.c. Wolfgang Eberhardt

Prof. Dr. Eberhard Jaeschke

Thomas Frederking

Scientific Highlights

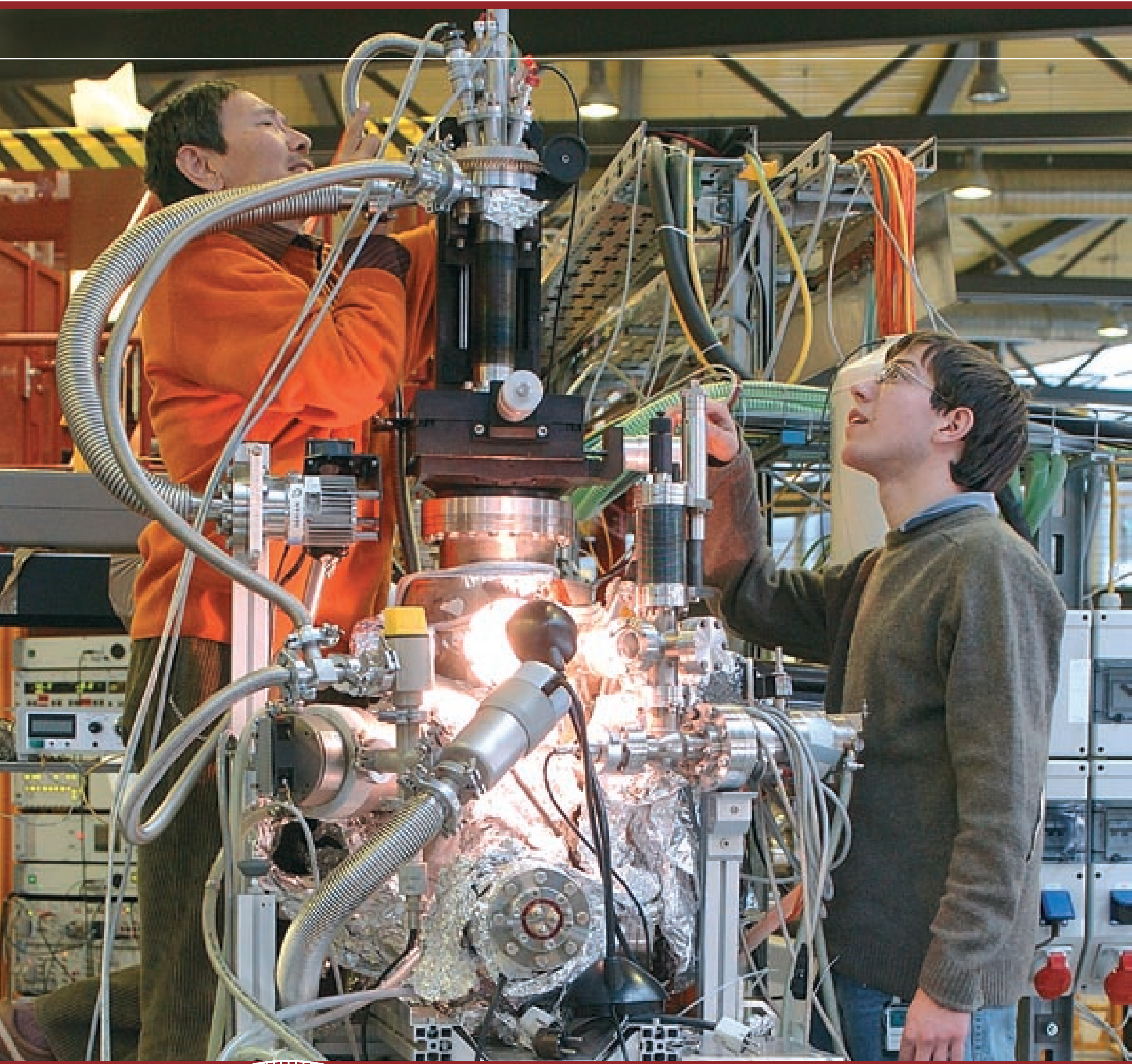

[1]
Fritz-Haber-Institut der
Max-Planck-Gesellschaft, Berlin

[2]
California Institute of
Technology, Pasadena, USA

Electrons in doubt: The double-slit experiment on molecules

D. Rolles [1], M. Braune [1], R. Hentges [1], S. Korica [1], B. Langer [1], A. Reinköster [1], J. Viefhaus [1], B. Zimmermann [2], V. McKoy [2], U. Becker [1]

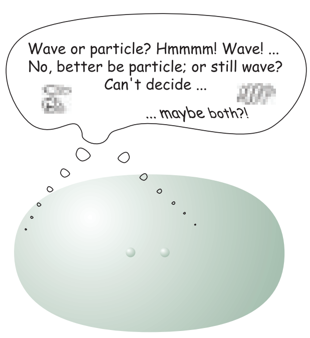

Electrons in doubt

The double-slit experiment, in particular performed with single electrons, is one of the key experiments of quantum mechanics. In 2002, the readers of the journal 'Physics World' even voted it to be the 'most beautiful experiment in physics' [1]: Although the electrons pass through the slits one at a time and appear as a single 'click' or speck on a screen, their sum still forms an interference pattern (Fig. 1). It seems as if each electron divides itself when passing through the double-slits, only to reunite again on the screen. However, if one slit is closed or if an observer determines which slit each electron passes through, the electrons behave like normal particles, that can only be at *one* point in space at a certain time, and the interference pattern disappears. In other words, depending on how the experiment is performed, the electron either appears to be at point A, or point B, or at *both* at the same time.

This apparent quandary is resolved by the particle-wave dualism and Bohr's complementary principle [2], which requires however that only *one* of the two forms of appearance, either particle *or* wave, can be observed at the same time. In recent times, scientists have questioned the validity of the complementary principle for photons as well as compound systems such as atoms [3] and fullerenes [4] as experiments have shown situations where matter appeared as particles and as waves at the same time – a gray area of complementarity. Would this gray area, or rather this area of coexistence, also be observable for structureless, non-compound particles like electrons?

We addressed this question in a 'molecular double-slit experiment' (Fig. 2) employing molecular nitrogen, N_2, as double-slit on atomic scale. We ionized the highly localized K-shell electrons in molecular nitrogen with polarized synchrotron radiation, knocking out one electron from each molecule. Because of the mirror symmetry of N_2, this electron belongs to both sides of the molecule in equal parts, and its emission is supposed to be coherent (i.e. phase-locked with phase 0 or π) from both atomic sides. The wave function ψ of the remaining ion is denoted with *g*, *gerade* (for phase 0), and *u*, *ungerade* (for phase π), in Fig. 2.

Until recently, it was impossible to separate the two wave functions concerning their angular dependence. However, this task has been achieved in the present experiment and it is now possible to observe each wave function separately. Both wave functions describe a state in which the electron exists at both sides simultaneously. Depending on the state, the wave function has either the same or the opposite sign on each side. The *gerade* case with equal signs corresponds to the classical double-slit experiment where the two sides of the molecule represent the two slits. Modern double-slit experiments with polarized photons can also generate the phase-shifted *ungerade* state. In that case, the interference pattern consists of so-called anti-fringes, where the dark and light areas are the inverse of the well-known interference fringes [5].

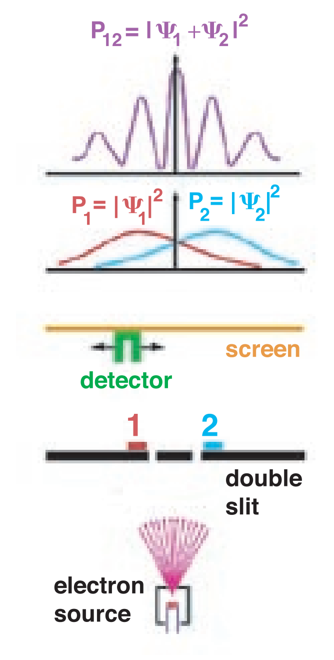

Fig. 1:
Double-slit experiment with single electrons. If one of the two slits is closed, a bell shaped shadow of the other slit is visible on a screen behind the slits. However, if both slits are open, an interference pattern of bright and dark stripes appears, from which no information can be inferred on the way the electron took to the screen.

References:

[1] R.P. Crease, Physics World Sep 2002; http://physicsweb.org/articles/world/15/9/2

[2] N. Bohr, Nature ***121****, 580 (1928).*

[3] S. Dürr et al., Nature ***395****, 33 (1998).*

[4] L. Hackermüller et al., Nature ***427****, 711 (2004).*

[5] S.P. Walborn et al., American Scientist ***91****, 336 (2003).*

[6] D. Rolles et al., Nature ***437****, 711 (2005).*

Acknowledgements:

Supported by the BMBF. D.R. also acknowledges support through the Feodor-Lynen program of the Alexander-von-Humboldt-Stiftung.

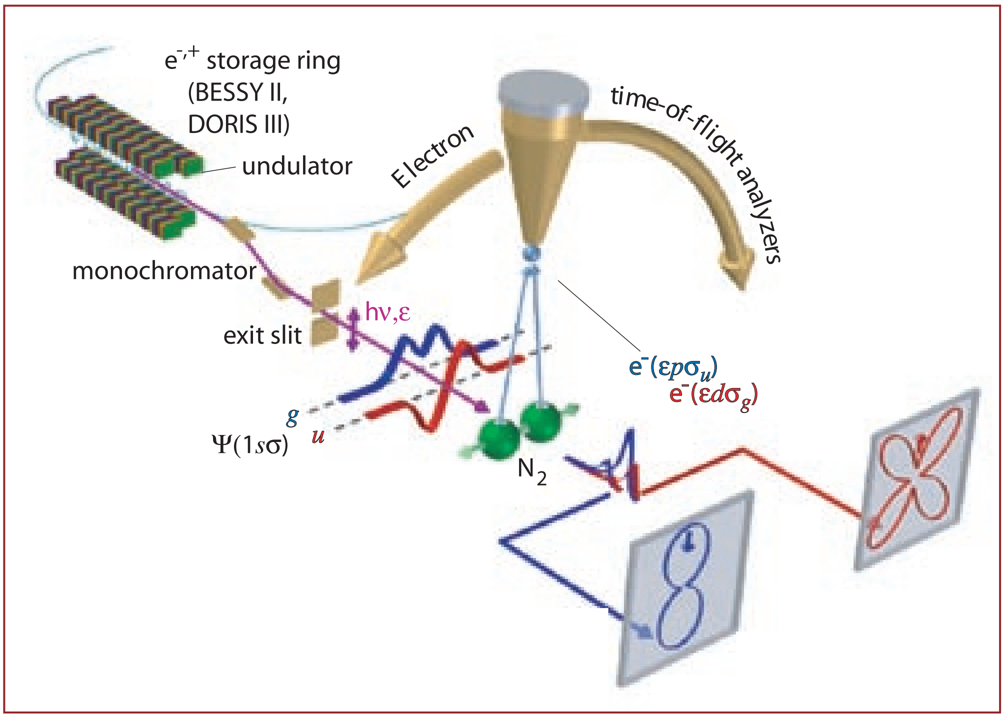

Fig. 2:
N_2-molecules are ionized with synchrotron radiation, and each molecule emits an electron from its inner-most shell. Depending on the phase-coupling inside the molecule, the electron is emitted with a slightly different energy, indicated by the red and blue spectral lines between the N_2-molecule and the 'screens' (right). Each one of those electron lines, called *gerade* ***(g) and*** *ungerade* ***(u), has a characteristic emission pattern, shown schematically on the corresponding 'screens'.***

In the molecular double-slit experiment, the molecular axes are statistically distributed in space. Therefore it is necessary to detect the electron in coincidence with the fragment ions created by the ionization. This allows measuring the angular distribution of the emitted electrons with respect to a fixed molecular axis. One can call this method a dynamical orientation of the molecules in the gas phase, where the orientation of each molecule at the instant of the electron emission is determined via the ionic fragmentation of the molecule. Fig. 3 shows the resulting electron angular distribution for the two states *g* and *u*.

In addition to demonstrating the coherent electron emission, an extra twist in the experiment also proved that breaking the molecular mirror symmetry leads to a loss of coherence. When repeating the experiment with a molecule made up of one lighter and one heavier isotope, in this case ^{14}N and ^{15}N, the electrons started to localize on one of the two, now distinguishable atoms. The electron distributions lost their strict parity-determining character and started to become more similar [6]. The shape of both angular distributions changed towards their common sum, as indicated by the arrows on the screens in Fig. 2.

Fig. 3:
Angular distribution of the *gerade* ***and*** *ungerade* ***electrons with respect to the molecular axis m for the 'perpendicular case' with the electric vector E of the ionizing radiation being perpendicular to m. The measurement shows the pure p- and d-character of the emitted electron waves. It is a direct proof for the existence of the non-local*** *gerade* ***and*** *ungerade* ***states in the molecule.***

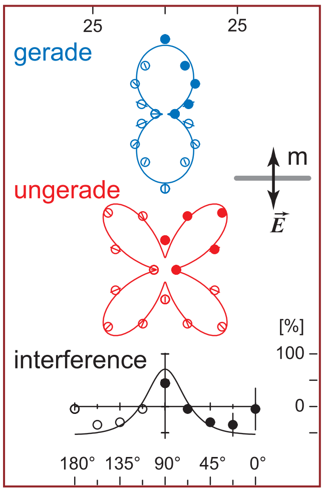

This situation corresponds a *partial* marking of one of the slits in the double-slit experiment and proves that even for electrons, the complementary principle is not valid in its original form as exclusion principle. The electrons are wave and particle at the same time.

While these results certainly demonstrate very fundamental properties of quantum mechanics, they may also be of importance for more practical applications such as the study and control of 'artificial molecules', which consist of semiconductor quantum dots and which are envisioned as possible building blocks of future quantum computers.

Contact:
Uwe Becker
becker_u@fhi-berlin.mpg.de

Reluctant to leave parent: A different spectroscopic look at salty liquid water

B. Winter [1], I. V. Hertel [1], C. Pettenkofer [2], S. E. Bradforth [3], M. Faubel [4]

[1] Max-Born-Institut, Berlin

[2] Hahn-Meitner-Institut, Berlin

[3] University of Southern California, Los Angeles

[4] Max-Planck-Institut für Dynamik und Selbstorganisation, Göttingen

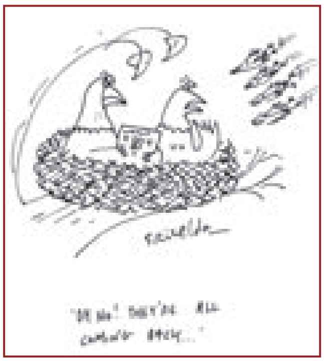

The environment always matters – or, what a nest and salty water have in common. Just like the chickens keep their eggs in a nest, salt ions in water can also form a nest to keep their electrons. This explains why an extra electron does not wander away from the parent ion in lukewarm water without a thought. The polar water molecules (with their large dipole moment) that surround a simple salt anion (like a chloride ion contained in ordinary table salt) to form the solvation shells, simply provide comfortable accommodation for electrons on the move. In the so-called Charge-Transfer-To-Solvent (CTTS) state the photoexcited excess electron resides in a diffuse orbital that protrudes from the anion into a cavity consisting of solvent molecules that belong to the first and second solvation shell. [1] This state is stabilized by the pre-existing orientation of the solvent dipoles that leads to an attractive potential for the electron. Hence these states are not a property of the anion, and there is no analogous in crystalline salt. CTTS processes can be considered the simplest condensed-phase photoinduced electron transfer reactions. They thus serve as models for electron transfer reactions found, for instance, in aqueous biology. The phenomenon has been known for long time, [2] when it was realized that halide solutions exhibit a characteristic absorption deep in the UV, which leads to a halogen atom plus an electron (Fig. 1). However, only recent developments of tunable ultrafast laser systems have enabled us to study CTTS reactions. This includes CTTS electron detachment and the subsequent production of a solvated (free) electron. Since the halides have no internal vibrational or rotational degrees of freedom, the measured spectroscopic dynamics can directly be associated with the motion of solvent molecules in response to the movement of charge. Even though many important studies in this field have been published in recent years, in particular by transient absorption measurements from aqueous solutions using ultrafast spectroscopy [1], the subject remains extremely attractive, and progress has not slowed down to date. Many questions remain open, among them the speed and modes of relaxation of the solvent shells, and the rate of electron detachment. Whether in the CTTS state or in any other transient configuration, we are still very much at the beginning of a thorough understanding.

Although electronic structural information can be readily obtained from photoemission, only recently such measurements have become possible in the high-vapor-pressure aqueous environment [3,4]. The experimental difficulty is to give the 'aqueous' electrons the chance to travel far enough to reach the electron detector, instead of losing their kinetic energy in multiple inelastic scattering processes with gas-phase water molecules above the liquid surface. This problem can be surmounted by using a flowing liquid microjet in ultrahigh vacuum.

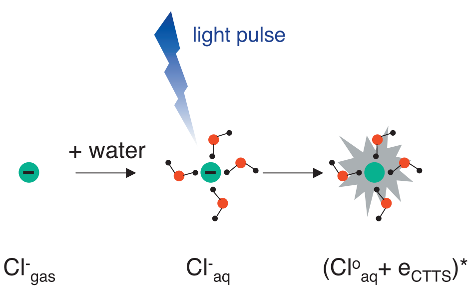

Fig. 1: The Cl^- anion with its hydration shell, and the Charge-Transfer-To-Solvent state created upon irradiation.

Only very few photoemission (PE) studies from liquid aqueous solutions have been reported to date but none with laser excitation. Fig. 2A shows four PE spectra from 3 molar aqueous LiCl solution, obtained for photon energies between 200.5 and 204.0 eV. The measurements were performed at the U41 undulator beamline. Traces *a-c* (200.5 eV, 201.0 and 201.5 eV) are PE spectra, measured at photon excitation energy below the ionization energy of aqueous Cl^- (2p). The Cl^- (2p) photoemission spectrum (Fig. 2B), which was obtained at much higher photon energy (400 eV), shows that the electron binding energies of aqueous Cl^- ($2p_{3/2,1/2}$) are 204.2 and 205.7 eV. For excitation energies at the onset of Cl^- (2p) ionization (trace *d,* 204.0 eV) a broad doublet feature appears in the spectrum, peaking near 177.2 and 178.4 eV (purple box).

References:

*[1] R. A. Crowell et al., J. Chem. Phys., **120**, 11712 (2004).*

*[2] M. J. Blandamer et al., Chemical Reviews, **70**, 59 (1970).*

*[3] M. Faubel et al., In Photoionization and Photodetachment; Ng, C. Y., Ed.; World Scientific: Singapore, **Vol. 10A**, Part 1; pp 634 (2000).*

[4] B. Winter et al., V. Journal of Physical Chemistry A, 108, 2625 (2004).

*[5] W. Wurth et al. Chemical Physics, **251**, 141 (2000).*

*[6] O. Karis et al., Physical Review Letters, **76**, 1380 (1996).*

[7] D. Nordlund, Core Level Spectroscopy of Water and Ice; Thesis, Stockholm University, (2004).

*[8] W. Eberhardt et al.; Phys. Rev. Lett., **41**, 156 (1978).*

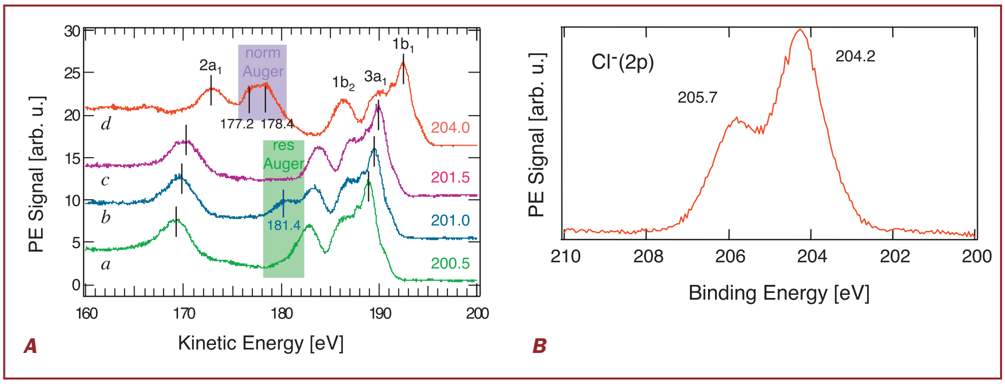

Fig. 2:
(A) Photoemission spectra of aqueous LiCl. Normal and spectator Auger features are indicated. The latter are observed for excitation of $Cl^-(2p)$ core electrons into the CTTS state. Photon energies are indicated.

(B) Photoemission spectrum of aqueous Cl^- at 400 eV.

Yet, most of the signal in the spectrum arises from water. The characteristic emission features originating from the four H_2O valence orbitals ($1b_1$, $3a_1$, $1b_2$, $2a_1$) in liquid water are labeled. The structure near 178 eV is assigned to an Auger decay (energy relaxation) process in which an outer-shell electron fills the Cl^- (2p) core hole.

For an illustration of the latter we consider the schematic in Fig. 3, which shows the relevant energy levels of the chloride anion in different situations: isolated Cl^-, Cl^- in water, and in CTTS state. The large energy shift of the lowest binding-energy level (3p) reflects the energy penalty associated with the re-orientation of water molecules when forming the solvation shell. This is the origin of the above mentioned optical CTTS absorption spectrum (wide arrow in center sketch). Electron photo-detachment of the Cl^- (2p) core levels (blue arrow) leads to the ejection of a direct photoelectron, and a missing 2p electron. Energy gained by subsequent (ultrafast) electron refill of the 2p hole (bent arrow) is used to eject a second valence electron (center sketch). In contrast to this non-resonant Auger process, in the case of resonant absorption the kinetic energy of the Auger electron gets larger. This is illustrated in the right sketch of Fig. 3, where the photon energy is somewhat below the Cl^- (2p) detachment energy, just sufficient to promote a Cl^- (2p) electron to the (unoccupied) CTTS level. In this case the additional CTTS electron remains as a spectator electron during the Auger decay (the CTTS lifetime is much longer than the core-hole lifetime), which causes an increase of the kinetic energy of the Auger electron due to Coulomb repulsion. Experimental evidence for this process is the appearance of a second Auger feature, near 181 eV (Fig. 2A trace *b*).

Spectator Auger decays have been previously observed in certain solid-state adsorption systems [5,6], including ice [7], but not yet for CTTS systems. The earliest report of this effect was more than 25 years ago [8]. We can expect that this newly identified core level-to-CTTS absorption will contribute to better understand of the fundamental details on electrons in aqueous solution, for instance, on how far the electron spatially extends, and at what rate it eventually detaches from the CTTS state - at which point the electron has really left the parent.

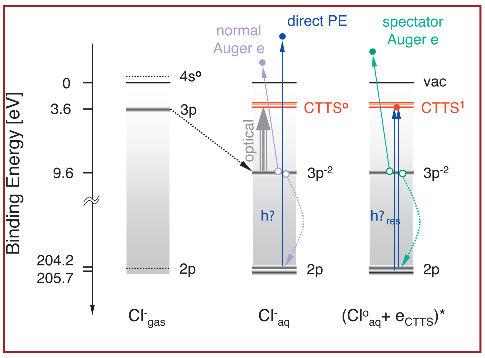

Fig. 3:
The electron energy levels for aqueous Cl^-. Optical and X-ray absorption transitions into the CTTS state are indicated.
The normal and spectator Auger processes are illustrated.

Contact:
Bernd Winter
bwinter@mbi-berlin.de

How to magnetize a soft-magnetic particle with microwaves

H.J. Elmers [1], A. Krasyuk [1], F. Wegelin [1], S. A. Nepijko [1], G. Schönhense [1], M. Bolte [2], C. M. Schneider [3]

[1] Johannes Gutenberg-Universität Mainz
[2] Universität Hamburg
[3] Forschungszentrum Jülich

A piece of iron or other so-called soft magnetic material does not necessarily show a spontaneous magnetisation like a compass needle. Even though locally the spins of the electrons are orientated in the same direction, the ferromagnetic order often decomposes the magnet in domains. In the different domains, the spins are oriented in different directions, in order to minimize the energy stored in the magnetic stray field outside of the magnet [1]. The magnetization can be saturated if a static external magnetic field is applied, i.e. all spins are then oriented in the same direction. Here we show that alternatively an electromagnetic microwave field can magnetize a small particle. Surprisingly, the particle is magnetized perpendicular to the direction of the magnetic microwave field (Fig. 1). Even more striking is the fact that by magnetizing the particle shows effectively an increased order against the common trend of increasing disorder and entropy. An open system with a constant throughput of energy, however, allows for an increase of local order. Life is a prominent example of this phenomenon.

Exciting micron-sized Permalloy particles with an oscillating external field, we found a similar example for this phenomenon that relies on the non-linear character of magnetization dynamics [2]. The samples are Permalloy ($Ni_{80}Fe_{20}$) platelets with 16 µm width, 32 µm length, and 10 nm thickness, placed on a coplanar waveguide. We measured the time dependent spatial distribution of the magnetization within the rectangular particle using a photoemission electron microscope (PEEM) [3]. X-ray magnetic circular dichroism (XMCD) images at the Ni L_3 absorption edge are obtained from two images taken with opposite polarization calculating the asymmetry at each pixel. Because of the grazing incidence of the X-rays, we are most sensitive to the in-plane magnetization component along the short side of the platelet. A microwave pulse generator injects a high-frequency ac current into the waveguide thus generating the magnetic field of 0.2 mT. Time-resolved images are taken by stroboscopic illumination of the sample by X-ray pulses produced by electron bunches in the synchrotron ring ($t_{FWHM} = 3$ ps, low-alpha mode) with a repetition rate of 500 MHz. The ac driving current and the probe pulses are synchronized via a variable electronic delay *t*.

Snapshots of the time evolution of the magnetization ***M*** in the Permalloy platelet are shown in Fig. 2. The orientation within the domains are indicated in Fig 3. An 180°-Neél wall along the y-axis separates the two large ones. In the Neél wall, ***M*** is oriented to the left; thus, the Neél wall appears black.
The intensity in the two large domains varies periodically, indicating the predominant excitation mode of a precession of the magnetization around the effective field axis directed parallel to the long side of the platelet (Fig. 2).

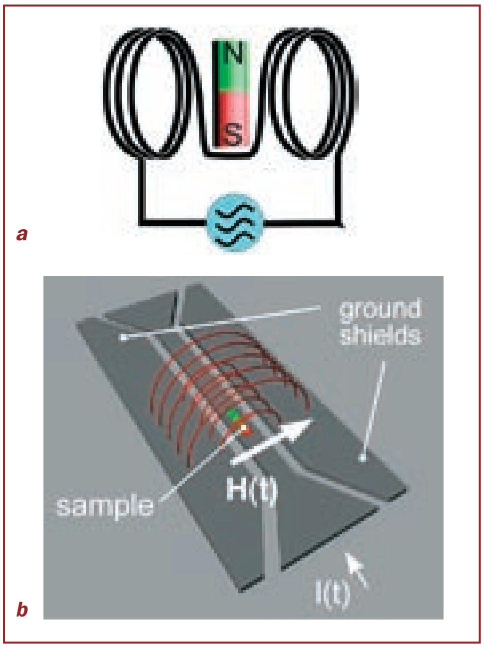

Fig. 1:
Cartoon of the experimental geometry (a) and a more realistic sketch (b).

References:

[1] A. Hubert and R. Schäfer, Magnetic Domains (Springer, Berlin, 1998).

*[2] A. Krasyuk et al., Phys. Rev. Lett. **95**, 207201 (2005).*

*[3] C. M. Schneider et al., Rep. Prog. Phys. **65**, 1785(R) (2002).*

*[4] S.-B. Choe et al., Science **304**, 420 (2004).*

*[5] J. Raabe et al., Phys. Rev. Lett. **94**, 217204 (2005).*

[6] K. Perzlmaier et al., Phys. Rev. Lett. 94, 057202 (2005).

*[7] H. Stoll et al., Appl. Phys. Lett. **84**, 3328 (2004).*

*[8] J. P. Park et al., Phys. Rev. B **67**, 020403(R) (2003).*

Acknowledgements:

Funded by the DFG (priority program 1133 'magnetization dynamics') and the BMBF (03N6500). Thanks to I. Mönch and J. Vinzelberg (IFW Dresden) for preparing the samples.

The system resembles a driven oscillator, and we observe the dynamical answer of the system to the periodic excitation. The domain walls and, particularly, the 180°-Neél wall move only very little throughout the series shown in Figs. 2. However, we observe a mean shift of the central wall out of its symmetrical position to the right. This shift increases with increasing amplitude of the exciting field and vanishes for large enough amplitudes (Fig. 3).

The basic mechanism, revealed by both stroboscopic imaging and computer simulation, is the decrease of the resonance frequency in the larger domain. This leads to larger energy dissipation in the magnetic particle, allowing increasing order with decreasing local entropy. The magnetization precession in the large domains mainly controls the energy dissipation in the particle. The system is excited with a significant oscillating field component of 1 GHz, i.e., just below the resonance frequency of the free running system of about 1.25 GHz. If the domain wall shifts to the right, the effective field determining the precession frequency and, consequently, the resonance frequency will decrease in the left domain and vice versa in the right domain. Therefore, the amplitude of the precession will increase in the left domain and decrease in the right domain. Since the precession energy is proportional to the square of the amplitude, the total energy has increased. Moreover, the domain with the larger amplitude has grown, which also helps to increase the deposited energy. The stray field energy resulting from the increasing magnetization finally balances the domain wall shift. The change of energy with the wall position can be interpreted as forces. That means above a threshold, the near-resonance spin wave mode causes an effective force perpendicular to the central 180°-Neél wall balanced by the restoring force of the stray field energy. The initial domain wall movement can occur to the left or to the right. However, we observed exclusively a shift to the right. Small inhomogeneities or a small vortex motion could be the reason [4].

This striking effect, although reproduced in simulations, would never have been found and explained without the joined effort of producing ultra short X-ray pulses at BESSY and setting up a time-resolved (TR-) PEEM experiment. The knowledge in the field of magnetization dynamics becomes increasingly important [4-8]. For example in magnetic memory devices, in which logical bits are recorded by setting the magnetization vector either ‘up’ or ‘down’, the fastest and most efficient recording method involves precessional switching. TR-PEEM is likely to contribute significantly to this field.

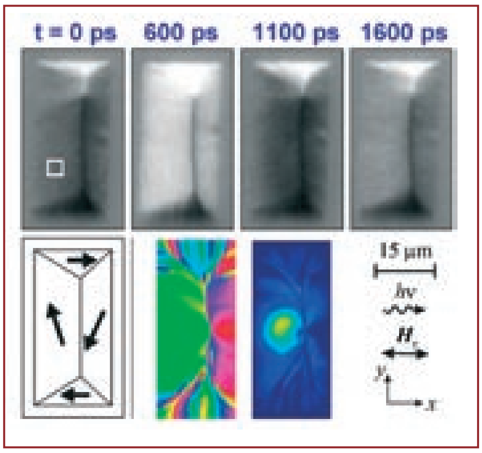

Fig. 2:
Top: XMCD images showing the time evolution of the x-component of the magnetization (bright areas are magnetized to the right, dark areas to the left, white square indicates largest domain) in a Permalloy platelet. Bottom (from left to right): Sketches of the corresponding domain pattern, micromagnetic simulation with color-coded phase and amplitude of the dominating 1 GHz oscillation mode and sketch of the geometry.

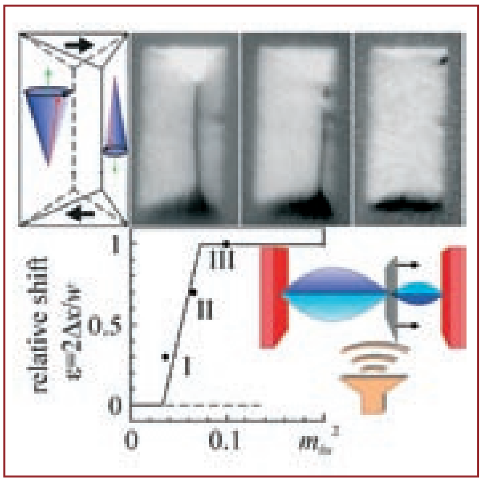

Fig. 3:
Top: Sketch and snapshots of magnetic domain patterns at the time t = 0 excited with increasing amplitudes I, II and III as indicated in the bottom panel. The bottom panel shows comparison of an analytical model and experimentally observed mean shift of the central domain wall. The inset shows an analog mechanical model.

Contact:
Hans-Joachim Elmers
elmers@uni.mainz.de

Single molecule magnets – building blocks for the future?

***M. Mannini* [1], *D. Gatteschi* [1], *R. Sessoli* [1], *L. Zobbi* [2], *A. Cornia* [2], *Ch. Cartier dit Moulin* [3], *Ph. Sainctavit* [3], *J.-P. Kappler* [4]**

1
INSTM & University of Florence, Italy

2
INSTM & University of Modena and Reggio Emilia, Italy

3
CNRS/UPMC, Paris, France

4
CNRS/ULP, Strasbourg, France

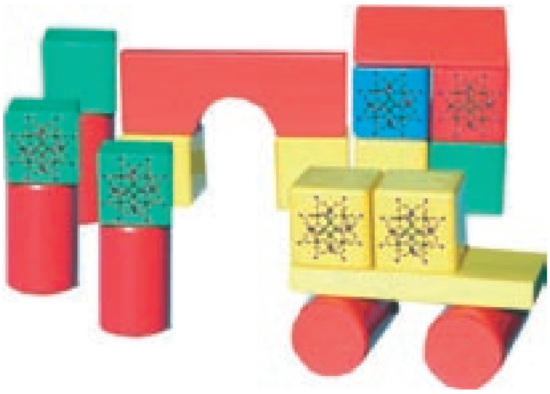

Nowadays chemists are able to produce molecules having properties of bulk materials or even capable to execute a function. Thus, molecules can constitute the building blocks for the growing little world of nanotechnologies. Since the early nineties of the last century a new kind of molecules has been investigated that individually behaves like a magnet and for this reason they are called Single Molecule Magnets (SMMs) [1]. The interesting potentiality of this kind of materials resides in the magnetic memory of the individual molecule. If it would be possible to address each individual molecule, the density of a computer memory could be increased dramatically. SMMs show a magnetic hysteresis that, contrarily to traditional materials is not a cooperative effect but rather a feature of the molecule on its own. SMMs are polynuclear metal complexes comprising paramagnetic transition metal centres lying in a high spin ground state thanks to exchange interactions inside the molecule. The magnetization freezes at low temperature when a large spin in the ground state is associated with a large magnetic anisotropy on the easy axis. Due to their reduced dimensions quantum effects are important and in principle SMMs could be exploitable in quantum devices.

The first and most investigated SMM is a cluster constituted by twelve Mn atoms (called Mn12, Fig. 1) organized in an internal tetrahedron of four Mn^{IV} ions and an external ring of eight Mn^{III} ions. All the Mn ions are connected to oxygen ions in an octahedral coordination. The Mn12 molecule growth is systematically blocked by an external organic shell (16 carboxylic acids) creating a perfectly monodisperse set of magnetic particles. The Mn^{IV} magnetic moments are antiparallel to those of the Mn^{III} ions, resulting in a ferrimagnetic structure with a total molecular spin S=10. Up to now, single molecule properties have been extrapolated from those of bulk samples (single crystal, powder, diluted solution). The simplest strategy to reach individual addressing of the clusters is to organize SMMs on surfaces and use techniques such as Scanning Probe Microscopy (SPM) that indeed have the high spatial resolution required for single–molecule addressing.

A crucial step is to show that during the deposition procedure the complex molecule still retains its structure and, above all, its peculiar magnetic behaviour. Traditional techniques for magnetic characterization lack the necessary sensitivity while XMCD has shown to be able to detect the magnetism of a submonolayer of magnetic atoms. In XMCD very fine details can be seen if they are not smoothed by the sample temperature. Cooling the sample to temperatures for which only a specific magnetic ground state is occupied has an incidence on the various cross-sections. This is particularly true in the field of molecular magnetism where complicated phenomena such has quantum spin tunneling where observed below 4 K in well chosen molecules [1,2]. Moreover, by recording the magnetic dichroic signal at the manganese $L_{2,3}$ edges in Mn12 clusters, one has immediate access to the magnetic structure of the cluster since the contributions from Mn^{III} and Mn^{IV} ions have opposite signs due to the antiferromagnetic coupling [3].

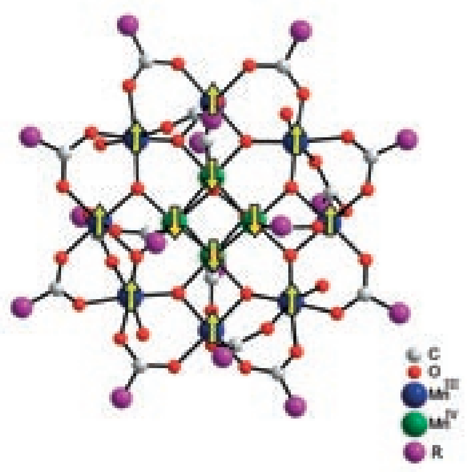

Fig. 1:
Magnetic structure of a Mn12 Single Molecule Magnet.

References:

[1] D. Gatteschi et al. Molecular Nanomagnets, Oxford University Press, Oxford 2006.

*[2] Ph. Sainctavit and J.-P. Kappler. Magnetism and Synchrotron Radiation, Lecture Notes in Physics, **Vol. 565**. Springer, Berlin, pp235-253 (2001)*

*[3] R. Moroni et al. Phys. Rev. B **68**, 064407 (2003)*

*[4] L. Zobbi et al. Chem. Comm. **12**, 1640 (2005)*

Acknowledgements:

Funding by IPCMS and European network of excellence MAGMANet. We warmly thank Paolo Imperia for instrumental support during the experiments.

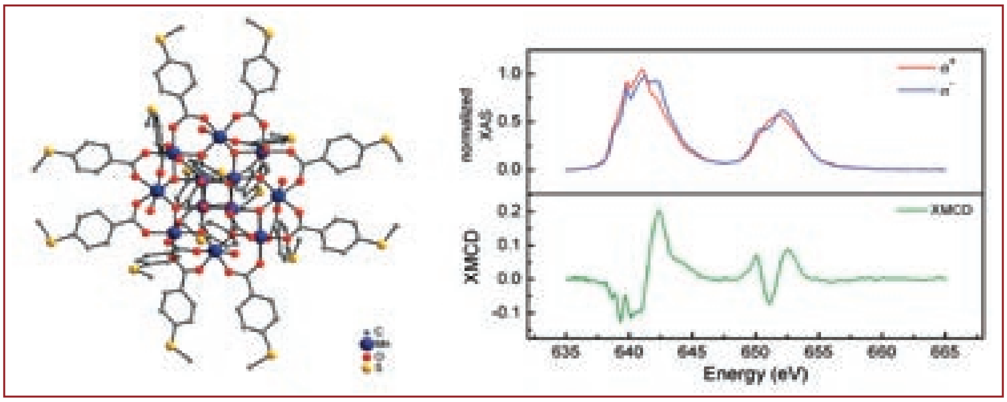

Fig. 2:
Mn12TE single molecule magnet. Left panel: structure of the functionalized molecule. Right panel: XMCD signal at Mn $L_{2,3}$ edges in bulk Mn12TE.

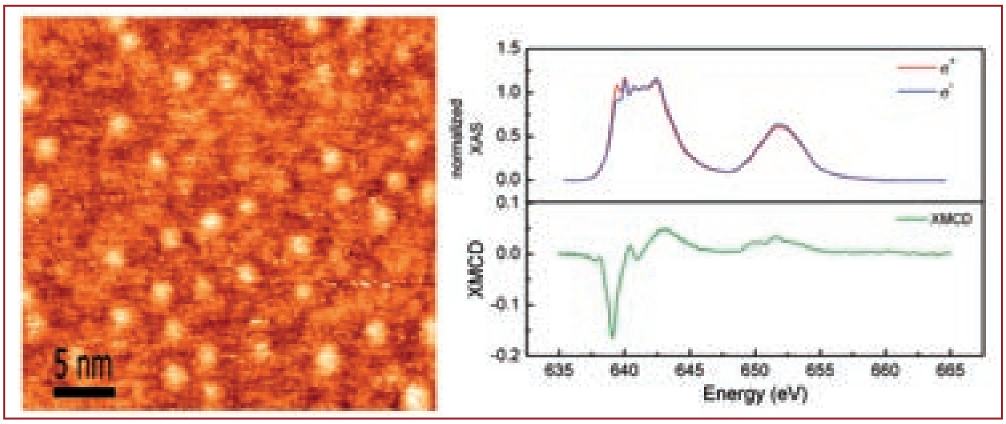

Fig. 3:
Mn12TE molecules deposited on Au(111) surface. Left panel: STM image from a submonolayer of Mn12TE deposited on Au(111). Right panel: XMCD signal at Mn $L_{2,3}$ edges in Mn12TE individual molecules deposited on Au(111).

We have used the XMCD technique to characterize the bulk properties of Mn12TE = ($[Mn_{12}O_{12}(OOCPhSCH_3)_{16}(H_2O)_4]$), a more complex Mn12 derivative that is able to bind gold surfaces through sulphur atoms (Fig. 2 left panel). XAS and XMCD characterizations obtained at 4.2 K and in an induction of 4 T show the persistence of the ferrimagnetic spin structure (Fig. 2, right panel). For a single layer of molecule, photo-reduction is likely to be encountered due to the high photon flux. In order to cope with that, UE46-PGM beamline is ideal since it is possible to reduce the number of photons on the sample by a factor of 500 (cooled aperture closed to 0.2x0.2 mm^2 and exit slit equal to 20 µm) and the photon density (extra factor of 400) thanks to a toroidal mirror providing a parallel beam. We could then characterize samples prepared ex situ starting from a solution of Mn12TE adsorbed on Au(111). The Mn12TE clusters form a submonolayer of isolated molecules (Fig. 3 right panel) [4]. The sample was inserted inside the XMCD cryostat and no evidence of significant photo-reduction was ever noticed after one day of measurements.

Preliminary results show that XAS spectra of the Mn12TE bulk molecule (Fig. 2 right panel) strongly resemble those of the Mn12 bulk sample [3]. A slight increase of the signal is due to some spurious Mn^{II} contributions. This result suggests that the chemical modifications of the original external Mn12 organic shell do not modify the magnetic properties of the Mn clusters. The antiparallel alignment of the Mn^{III} and Mn^{IV} spins is conserved.

Surprisingly, the dichroic signal is substantially modified after the deposition on the Au surface (Fig. 3, left panel). A qualitative analysis points that the negative XMCD peak at 638 eV in Fig. 3 can be attributed to Mn^{II} ions. This suggests that a quite large Mn^{II} component is present in addition to Mn^{III} and Mn^{IV} ones. This is to be confirmed by Ligand Field Multiplet calculations that are still in progress. Moreover the typical fingerprint of antiparallel alignment of Mn^{III} and Mn^{IV} is not easily detected from the submonolayer. Interactions with the gold substrate, as well as a reduction during the deposition, might be the origin of this observation. This intriguing result that is beyond the sensitivity of STM images does not however reduce the interest in this kind of innovative materials but suggests us to continue this investigation by playing on the deposition conditions and by exploiting different substrates.

Contact
Philippe Sainctavit
Philippe.Sainctavit@impmc.jussieu.fr

BESSY

How dirty tungsten tidies up the nanoworld

A. Varykhalov, O. Rader, W. Gudat

Much more than anything it is the sight of scientists wrapped up in clean room garments which tells us that nanoscience comes along with extreme demands on purity. Semiconductor lithography nowadays uses several hundred individual processing steps and is able to create objects of lateral dimensions as small as 50 nm. In order to answer questions on the limitations of the principles of electronic circuits and magnetic storage, one has to reach even smaller structures. Because conventional lithographic techniques fail to provide electronic components of atomic dimensions, one has to switch over from the 'top-down' to a 'bottom-up' approach. This means the employment of self-assembly tendencies during atomic growth. There is an aspect of self organization which occurs during growth on a clean crystalline substrate: additional atoms tend to agglomerate at step edges and it is well known that a rough or regularly stepped surface leads to faster growth. This wisdom has also been used to create wires of single-atom width on regularly stepped Cu, W, and Pt surfaces [1]. In some cases, also flat surfaces form a long-range reconstruction of their surface which leads to the self-assembly of atomic clusters. This has been observed for Co on Au(111) [2] and for In and Pb on Si(111)-(7×7) [3]. This works, however, only for particular substrate-adsorbate pairs.

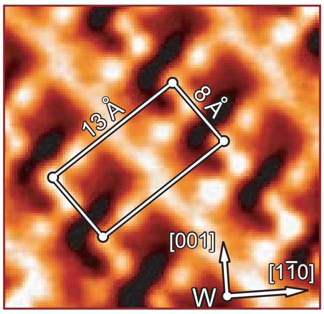

***Fig. 1:* STM image of the two-dimensional surface carbide. It constitutes a nanomesh of carbon atoms embedded into the surface atomic layer of W(110).**

We have discovered a unique template which universally supports self-organization of nanostructures with very different atomic and electronic properties ranging from metallic wires to molecular clusters. The substrate is the (110) surface of tungsten and the template, which plays the role of the mask in conventional and X-ray lithography, is a carbide overlayer, the so-called R(15×3) structure. This structure typically forms as unwanted contamination when the surface of a new W(110) crystal is prepared by heating. Carbon then segregates from the volume to the surface. In our case, to be more reproducible, we have prepared the structure by cracking of propylene.

An STM picture is shown in Fig. 1 [4]. This nanomesh of carbon consists of knee-shaped atomic chains and the superstructure has a periodicity of 8 Å × 13 Å. Such specific potential profile is accompanied by significant mechanical strain due to strong W-C chemical bonding. We believe that this strain contributes to the large variety of self-organization phenomena on this surface.

The most fascinating examples of such effects are presented below. Au atoms deposited at room temperature on W(110)/C-R(15×3) do not form any particular crystalline structure but when being heated they self-assemble into Au nanowires [5].
Fig. 2 shows STM images of these nanowires developed from the mass equivalent of 2 monoatomic layers (ML) of Au. From the large-scale image in Fig. 2(a) it can be seen that the wires appearing in pairs, are perfectly straight and continuous on a length scale of hundreds of nanometres. Important is that the wires are much wider (~1 nm each) than atomic chains. For such wires, one dimensionality and quantum size effects have not yet been reported in electron spectroscopy. According to our STM experiment the wires form on the surface for Au coverages up to 4 ML. Moreover, their periodicity slightly varies with the thickness of the deposited Au. For coverages above 1 ML they merge and appear as one-dimensional nanowire-like surface reconstruction of the Au film. Fig. 2b displays the STM image of 2 ML-thick Au on the surface carbide revealing dramatic changes in the surface atomic structure.

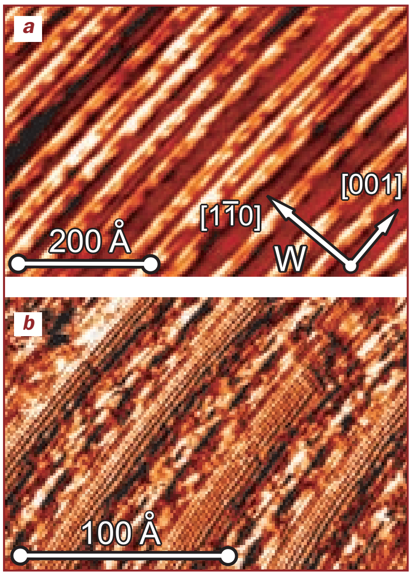

***Fig. 2:* STM evidence of metallic nanowires self-assembled from (a) 0.7 ML Au and (b) 2 ML Au.**

References:

*[1] P. Gambardella et al., Nature **416**, 301 (2002).*

[2] B. Voigtländer et al., Phys. Rev. B 44, 10354 (1991).

*[3] S.-C. Li et al., Phys. Rev. Lett. **93**, 116103 (2004).*

*[4] A. Varykhalov et al., Phys. Rev. B **72**, 115440 (2005).*

*[5] A. Varykhalov et al., Phys. Rev. B **72**, 241404 (R) (2005).*

Acknowledgements:

Fig. 5a taken from P.A. Brühwiler et al., cond-mat/0108111.

We have probed the electronic properties of the wires by angle-resolved photoelectron spectroscopy (ARPES) at beamlines UE56/1 PGM and UE52/SGM. Fig. 3 reports original ARPES spectra (a,b) and extracted band dispersions E(k) (c,d) which supply information about the energy-momentum relations for the electrons in the nanostructure. In our particular case the Au band structure is strongly anisotropic. For the electrons propagating along the wires the dispersion of the band at 5 eV binding energy (red line) is expectedly parabolic (Fig. 3a,c).

In the direction perpendicular to the wires their periodic potential works now to confine the electrons to the wires. This leads to quantization in the lateral direction and splitting up of the dispersion into the constant energy levels E_1 and E_2 (Fig. 3d).

In another experiment, we have studied the behaviour of C_{60} on top of the surface carbide. C_{60} is famous as the carbon molecule with highest symmetry in its class and has the structure of a hollow sphere like a soccer ball (Fig. 4a).

According to results of our STM characterization of C_{60} molecules on W(110)/C-R(15×3) they self-organize into nanoclusters. These nanoclusters consist of a 'magic' number N of molecules.

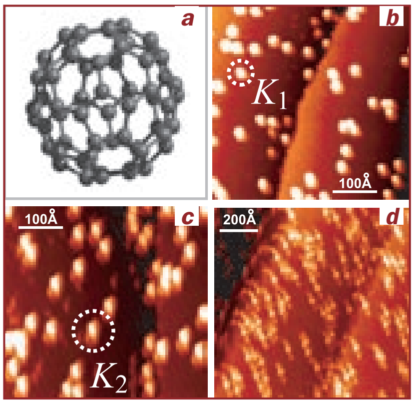

Fig. 4:
Model of C_{60} molecule (a) and STM pitures of C_{60} nanostructures self-assembled on the surface carbide. $(C_{60})_4$ (b), $(C_{60})_7$ (c), and C_{60} chains (d).

The 'magic' number is apparently so efficient that at a given deposited amount, only one cluster type out of two K_1 (N=4) and K_2 (N=7) with perfectly uniform dimensions and shapes are formed (Fig. 4b,c). At further increased nominal coverage a collective rearrangement of self-assembled nanoclusters takes place creating cluster chains which are tens of nanometers long (Fig. 4d).

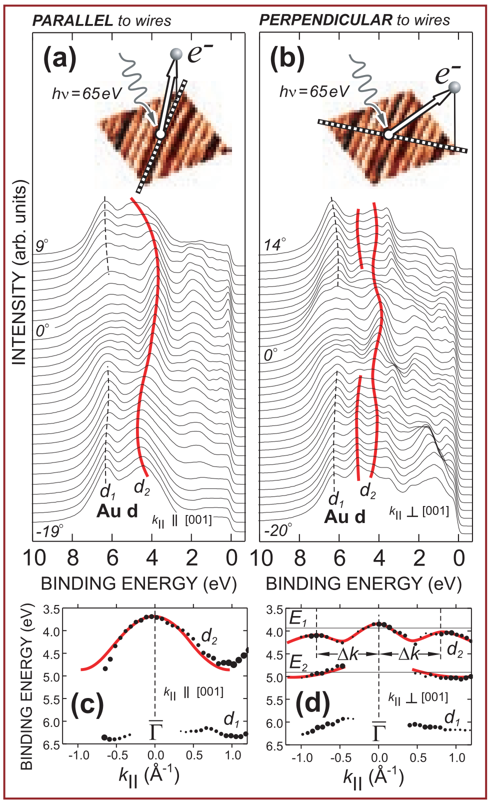

Fig. 3:
Angle-resolved photoemission from Au wires; one-dimensional dispersion and lateral quantization of the d-band at 5 eV binding energy are observed.

To understand the mechanism which determines the observed phenomena we performed a photoemission study of C_{60} clusters. Fig. 5 compares the spectra from C_{60} on W(110)/C-R(15×3) (b) and C_{60} deposited onto clean W(110) (c). It can evidently be seen that electronic states of C_{60} on the surface carbide are unperturbed with no charge transfer to the carbide, just exactly the same as for C_{60} on graphite (Fig. 5a) – which serves as reference system where van der Waals interactions are established. Based on this we described nanoclusters in terms of self-organization in a molecular gas of C_{60} which is reduced to two dimensions by a weak sticking potential of the carbon nanomesh. Using the Lennard-Jones pairwise potential for description of C-C interactions we have determined two energetically favorable cluster structures with 4 and 7 molecules in the configurations K_1 and K_2, respectively. These results are in good agreement with our STM studies.

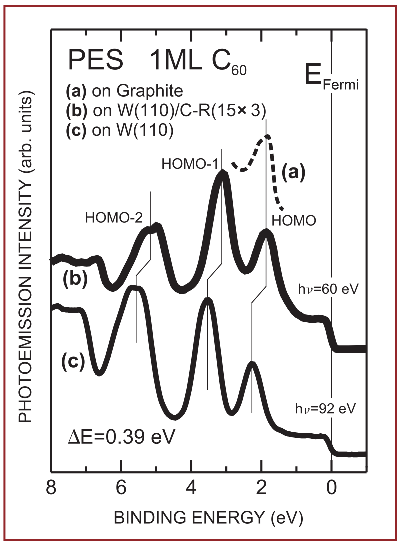

Fig. 5:
Photoemission from fullerene nanoclusters reveals van der Waals forces as dominant interaction with the template.

Contact:
Andrei Varykhalov
andrei.varykhalov@bessy

**Universität
Erlangen-Nürnberg**

Silver decoration of platinum step edges – tuning the complexity of surfaces

R. Denecke, B. Tränkenschuh, R. Streber, C. Papp, H.-P. Steinrück

Realistic surfaces of catalytic systems are usually far away from the flat, low-index single-crystal surfaces commonly used in surface science studies. In order to bridge this “complexity gap”, regularly stepped single-crystal surfaces are used to study the influence of step edges on surface reactions. By varying the terrace width and the step orientation, possible mechanisms present on realistic surfaces can be studied in a controlled way. An elegant approach to further increase the complexity is to successively decorate the steps and finally the terraces by small amounts of inert metals, such as silver.

To tackle these questions, we have chosen a sample family comprising Pt(111), Pt(355), and Pt(322) surfaces. The latter two stepped surfaces have (111) terraces which are nominally five atom rows wide; the difference lies in the step orientation, being (111) on Pt(355) and (100) on Pt(322). The model surface reaction studied is the CO oxidation, with CO adsorption being a fundamental reaction step.

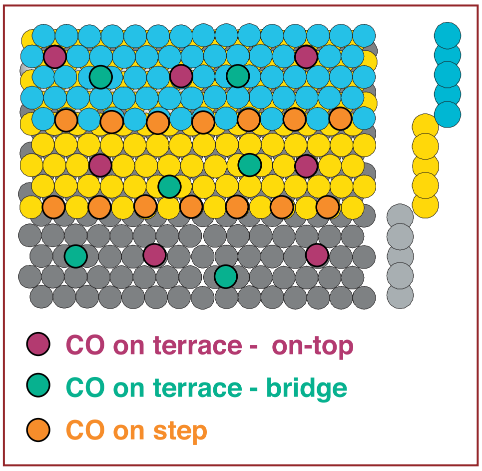

***Fig. 1:* Schematic depiction of the Pt(355) surface with highly symmetric adsorption sites for CO.**

Applying high-resolution X-ray photoelectron spectroscopy (XPS) using synchrotron radiation at BESSY (U49/2-PGM1), we can identify various highly symmetric adsorption sites of CO, such as step sites and terraces sites. A selection of these sites is shown in Fig 1. Occupation of these sites can be monitored *in situ* in a time-dependent way during adsorption and reaction by quantitatively analyzing C 1s spectra (examples shown in the inset to Fig. 2).

On the flat Pt(111) surface, CO adsorbs at two adsorption sites, on-top and bridge [1]. These sites are also observed on the terraces of the stepped sisters, where additional adsorption sites are identified by their C 1s binding energy. While only one such step site is found on Pt(355) [2], with CO most likely in on-top geometry on the upper step edge, two such step sites (likely to be on-top and bridge) are observed on Pt(322). During the adsorption process, the step sites are occupied first, as shown in the top part of Fig. 2, reflecting the stronger bonding of the CO molecules there. The terrace sites follow, with the occupation ratio between on-top and bridge sites depending on step orientation, being in general different to the Pt(111) surface [2] (e.g., showing relatively higher bridge occupation for low CO coverages on Pt(355)).

It is now interesting to investigate the influence of Ag decoration on CO adsorption. In scanning tunneling microscopy (STM) studies, Ag is found to nucleate preferably on the edges of (111) oriented steps for room temperature deposition [3]. In particular, besides other Ag coverages, a row of Ag atoms can be prepared along the Pt step edge. Some fundamental question arise: how does Ag influence CO adsorption on the step sites? Is there an influence on the terraces, too (by changing the free Pt terrace width)? And does CO in turn have some influence on the Ag? From our current understanding we can state that the situation is rather complex, due to small energetic differences between the various adsorption configurations. In the following, we will sketch some of the observations.

For temperatures, where CO does usually not adsorb on Ag (here we used ~130 K), the total amount of CO on the surface should be directly proportional to the free Pt surface area, for the proposed two-dimensional Ag growth [4]. This is indeed the case for both stepped surfaces, as can be seen from the upper part of Fig. 3. In fact, this 'CO titration' is a nice way to calibrate the Ag monolayer coverage, which is reached when no (or nearly no) CO adsorbs any more. The relative coverages of terrace and step sites, however, differ significantly for the two surfaces (lower part of Fig. 3). Starting with the clean surfaces, the amount of CO

References:

*[1] M. Kinne et al., J. Chem. Phys. **117** 10852 (2002) and references therein.*

*[2] B. Tränkenschuh et al., J. Chem. Phys. **124** (2006) 074712.*

*[3] P. Gambardella et al., Phys. Rev. B **61** (2000) 2254; P. Gambardella, PhD thesis, Lausanne (2000).*

*[4] Davies et al., Surf. Sci. **121** 290 (1982).*

Acknowledgements:

Work was supported by DFG (STE620/4-3).

found on step sites on Pt(322) is smaller by about 50% as compared to Pt(355). This is compensated by a higher terrace occupation on Pt(322). Adding now Ag atoms to the surface, changes the geometric and electronic situation even further (lower part of Fig. 3). It seems as if the CO step population on Pt(355) is reduced by a Ag row to the value on Pt(322), while the terrace population stays unchanged, in spite of the reduced free Pt terrace area. We interpret this as a conversion in terms of electronic behavior (this is what the C 1s binding energy measures) of step bound CO into “terrace-like CO”. Ag atoms decorating the Pt step edge would, in this sense, mimick Pt atoms for the CO, which finds itself away from the new step edge. On Pt(322), this channel seems to be absent.

The fate of the residual CO step population on both surfaces reveals itself in the coverage-dependence of the site population. As an example, we show in Fig. 2 (lower part) results for a single Ag row on the stepped samples. Ag indeed keeps the CO molecules away from the more favourite step sites on both surfaces, but only for low CO coverages. The re-occupation of these sites at higher coverages could be explained, if the Ag atoms respond to the new situation by partially moving away from the step edge to form (most likely step-attached) Ag islands. A cartoon to visualize these steps is shown in Fig. 4. This process is enhanced by higher temperatures, present, e.g., during thermal annealing of these layers. However, from a variation of the Ag coverage it becomes obvious, that larger amounts of Ag are harder to move; therefore, a smaller or no step population is observed then.

The detailed processes, which are in the focus of our current analysis, are driven by the subtle interplay of molecular (CO) and atomic (Ag) surface species and the interactions among them, with all relevant energetic terms being very similar (within 150 meV at most). Using our spectroscopic magnifying glass together with real space information from STM studies allows shedding light on situations which are expected to be governing key players on real catalytic systems. In this way new parameters could be identified to further optimize these systems.

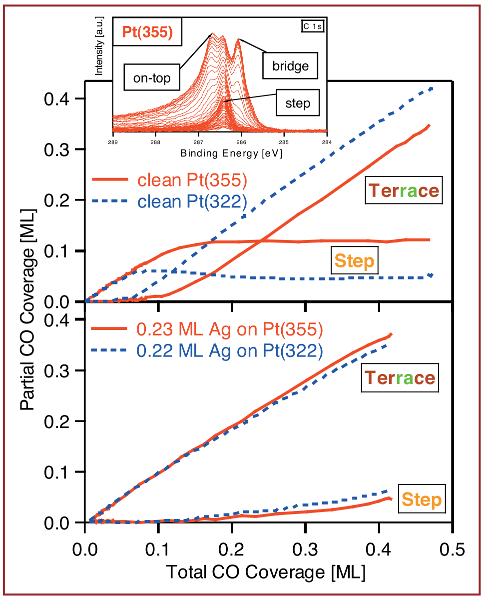

Fig. 2:
Coverage dependent site occupation for CO adsorption at 130 K on Pt(355) (red, solid lines) and Pt(322) (blue, dashed lines). Top: Results for clean surfaces. Bottom: Results for 0.23 ML of Ag evaporated at 300 K, resulting in a single atomic Ag row at the Pt step edges. Inset: C 1s spectra taken during CO adsorption on clean Pt(355); hν=380 eV.

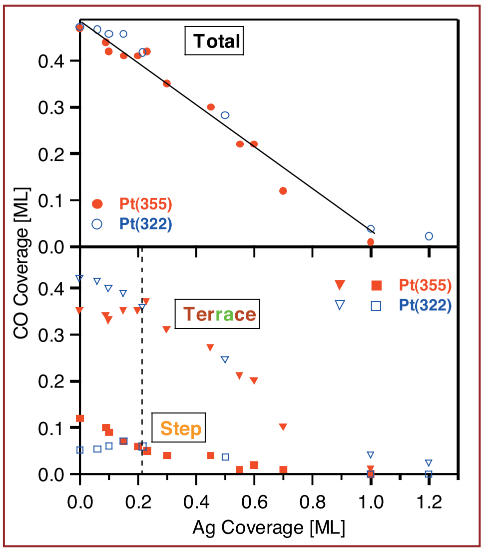

Fig. 3:
Total (upper part) and partial (terrace and step – lower part) CO coverages for saturation at 130 K, as a function of Ag coverage. Ag was evaporated at 300 K. Red, filled symbols denote results for Pt(355), blue, open symbols such for Pt(322).

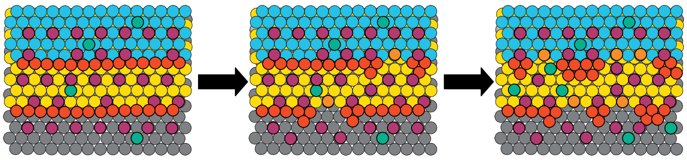

Fig. 4:
Schematic picture of the CO adsorption situation on Pt(355), decorated with a single Ag row, for increasing CO coverage. Red filled circles denote Ag atoms, CO molecules are given in the color code established in Fig. 1.

Contact:
Reinhard Denecke
reinhard.denecke@chemie.uni-erlangen.de

1
Humboldt-Universität zu Berlin

2
BESSY

3
Universität Hamburg

A flexible future: Controlling interface energetics for organic electronics

N. Koch [1], S. Duhm [1], A. Vollmer [2], R. L. Johnson [3], J. P. Rabe [1]

When you look at modern mobile phone displays or flat TV-screens you may already see a new disruptive technology. This technology, summarized by the term 'Organic Electronics', is based on conjugated organic materials as active layers in electronic and opto-electronic devices. Current mobile phone displays utilize just organic light emitting diodes (OLEDs), but other organic-based devices currently being investigated include a multitude of functionalities such as solar cells, thin film transistors, and memory cells.

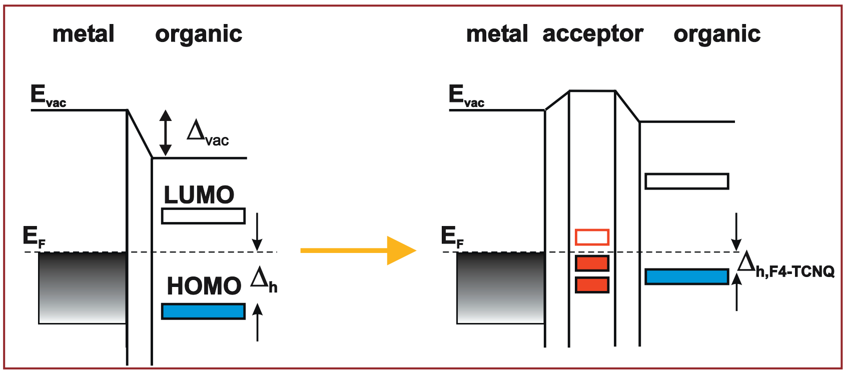

***Fig. 1:* Schematic energy levels at organic/metal interfaces without (left) and with electron acceptor pre-coverage (right).**

References:

*[1] A. Kahn, et al., J. Polym. Sci. B **41**, 2529 (2003).*

*[2] N. Koch, et al., Phys. Rev. Lett. **95**, 237601 (2005).*

*[3] N. Koch, et al., Appl. Phys. Lett. **87**, 101905 (2005).*

*[4] A. Vollmer, et al., Eur. Phys. J. E **17**, 339 (2005).*

Acknowledgements:

Supported partly by the Sfb448 (DFG). NK acknowledges financial support by the Emmy Noether-Program (DFG).

The conjugated organic materials employed in such devices can be small molecules or polymers. Consequently, organic electronic devices allow for mechanical flexibility, paving the way for entirely new applications, such as displays that can be rolled up or follow the contour of any given surface. In particular, the integration of opto-electronic devices into clothing appears highly attractive ('Smart Clothing'). Just imagine outdoor-jackets with integrated solar cells on the back and GPS plus display and mobile phone in your arm sleeves.

Other advantages of Organic Electronics over conventional technology include the light weight of organic materials and comparably cost-effective manufacturing. For instance, thin film structures of organic materials can be fabricated by vacuum sublimation, spin-coating, or various direct printing techniques.

Functional organic electronics structures often comprise multiple layers of organic materials and contacts for electron or hole injection. Metal-organic and organic-organic interfaces are therefore ubiquitous in small molecule and polymer devices alike. They are the key - but quite often also the bottle-neck - for efficient injection of charge carriers into the films. Given their obvious importance, these interfaces have been the subject of multiple fundamental and phenomenological investigations aimed to understand their electronic and chemical properties, to control interface energy barriers, and to optimise the injection of charge carriers [1].

The hole injection barrier (Δ_h) is a key parameter determining device performance. It can be measured experimentally using ultraviolet photoelectron spectroscopy (UPS) as the energy difference between the metal electrode Fermi-energy (E_F) and the low binding energy onset of photoemission from the organic material, its highest occupied molecular orbital – HOMO (Fig. 1). For a given pair of electrode and organic material, rational routes for optimizing Δ_h have to be developed. Recently, we have shown that the insertion of a (sub-)monolayer of strong electron accepting molecules, such as tetrafluoro-tetracyanoquinodimethane (F4-TCNQ) (Fig. 2), between a metal electrode and virtually any conjugated organic material can be used to adjust Δ_h predictably over wide ranges [2,3].

We performed photoemission experiments at the SurICat end-station (beamline PM4) [4]. Small molecular organic materials were evaporated *in situ* from resistively heated pinhole sources. UPS spectra of polycrystalline Au

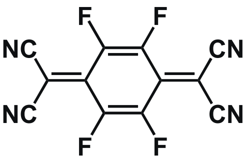

***Fig. 2:* Chemical structure of tetrafluoro-tetracyanoquinodimethane (F4-TCNQ).**

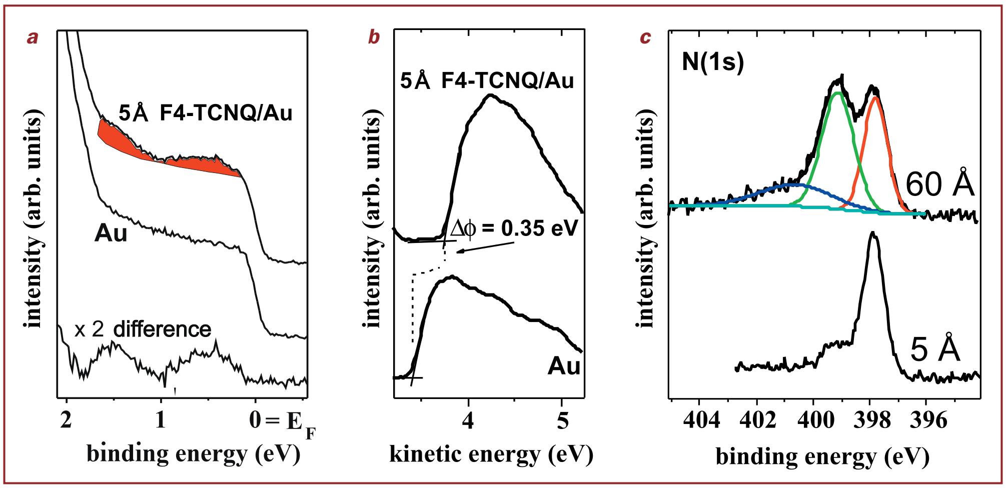

Fig. 3:
Ultraviolet photoelectron spectra of the F4-TCNQ/Au system. (a) Valence region. The difference spectrum of the shaded area and the Au spectrum is shown on the bottom of the graph. (b) Secondary electron cut-off. (c) N1s core levels for 5 Å and 60 Å layers F4-TCNQ adsorbed on Au.

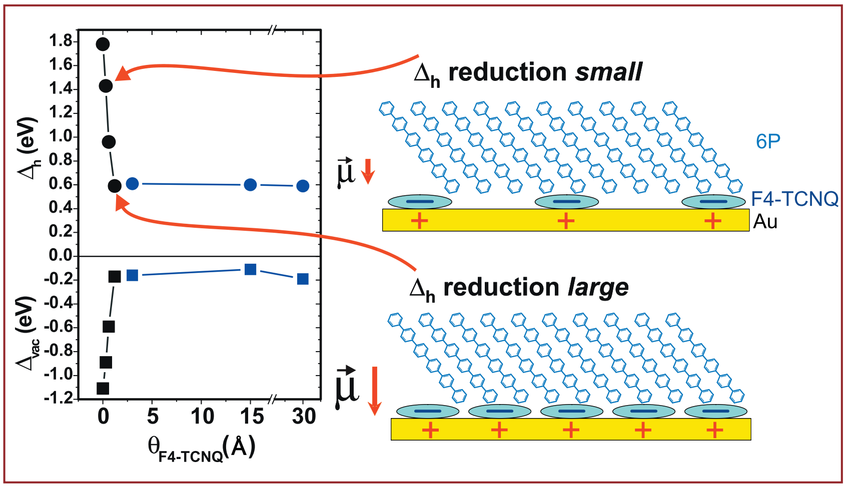

Fig. 4:
Δ_h (hole injection barrier) and Δ_{vac} (sample work function change) for p-sexiphenyl (6P) as function of F4-TCNQ pre-coverage on Au ($\theta_{F4\text{-}TCNQ}$). The steep part of the curves (black) represents the (sub-) monolayer of F4-TCNQ. The sketch shows surface dipoles μ induced by F4-TCNQ on Au in the low- and high-coverage range.

before and after deposition of nominally 5 Å F4-TCNQ are shown in Fig. 3a. The shaded areas indicate new photoemission features, which can be clearly seen in the difference spectrum (bottom). The sample work function (ϕ) increased from 5.25 eV (for pristine Au) to 5.6 eV (5 Å F4-TCNQ) as revealed by the shift of the secondary electron cut-off (Fig. 3b). X-ray photoelectron spectroscopy measurements for 5 Å F4-TCNQ/Au showed two peaks in the N(1s) region at 397.8 eV and 399.15 eV binding energy (Fig. 3c). Further deposition of F4-TCNQ to 60 Å led to an intensity increase in the higher binding energy component in the N(1s) spectrum.

We assign the lower binding energy peak to the anion F4-TCNQ which is in direct contact with Au and the higher binding energy N(1s) peak to neutral species in the multilayer. The third broad component centred at approx. 400.5 eV binding energy is attributed to shake-up processes, in which relaxation energy is used to excite electrons from valence level to bound states. Our results indicate a significant electron transfer from Au to F4-TCNQ.

In subsequent experiments, we measured the hole-injection barriers at interfaces between F4-TCNQ/Au and three electroactive conjugated organic materials as a function of F4-TCNQ pre-coverage ($\theta_{F4\text{-}TCNQ}$). We found significant reduction of Δ_h in all cases, for the blue electroluminescent *p*-sexiphenyl the reduction of Δ_h was up to 1.2 eV (Fig. 4). This effect is independent of charge transfer complex formation between the conjugated organic materials and F4-TCNQ. Furthermore, in the system *p*-sexiphenyl/F4-TCNQ/Au Δ_h could be tuned systematically over a wide range by appropriate adjustment of $\theta_{F4\text{-}TCNQ}$ from 0 to around 2 Å, which is about a monolayer of 4F-TCNQ (Fig. 4). This is explained in terms of the $\theta_{F4\text{-}TCNQ}$-dependence of the area-averaged surface potential of F4-TCNQ/Au substrates. Higher pre-coverage did not result in further reduction of Δ_h.

Our results indicate that by using (sub-) monolayer coverages of strong electron acceptors on metal surfaces the hole-injection barriers at virtually any organic/metal interface can be optimised in a flexible and predictable way.

Contact:
Norbert Koch
norbert.koch@physik.hu-berlin.de

Darmstadt University of Technology

Alignment in the solvent - unique experiments at the solid/liquid interface

K. Schwanitz, E. Mankel, R. Hunger, T. Mayer, W. Jaegermann

Liquids and ultra high vacuum? This is an antagonism, the liquid would just evaporate! But so many interfaces between solids and liquids are of technological interest. Typical examples are corrosion and etching processes, batteries, fuel cells and biosensors. For a fundamental understanding, these processes need to be analyzed with modern ultrahigh vacuum (UHV) surface science techniques. But how can we keep the liquid on the surface under UHV conditions? We freeze it! Either a liquid film just a few molecules thick is frozen after the interface has been separated from the liquid under normal pressure or a thin layer is condensed from the gas phase onto the solid surface that is cooled to low temperature [1].

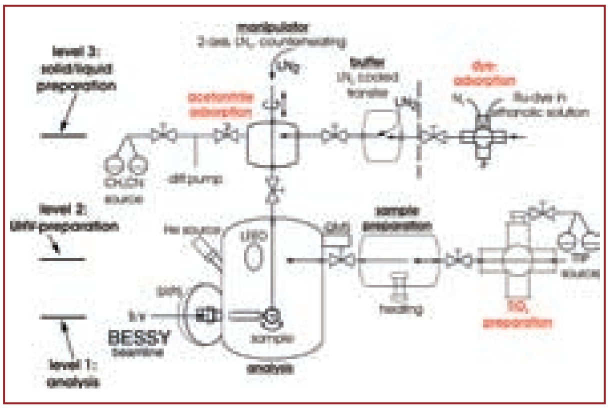

***Fig. 1:* Schematic of the solid/liquid analysis system SoLiAS. The liquid nitrogen cooled manipulator allows investigating frozen liquids under UHV conditions. The buffer chamber enables sample transfer without contact to ambient air.**

If we want to analyze atomically thin surface layers with highest surface sensitivity and spectroscopic resolution, very special measures have to be taken in order to avoid contamination by ambient air or ubiquitous hydrocarbons. Therefore it is required to carry out the entire wet processing under normal pressure in a high purity inert gas atmosphere in a system directly attached to the UHV system – the **Solid/Liquid Interface Analysis System SoLiAS** (Fig.1). Without contact to ambient air the sample is transferred via a buffer chamber vented with high purity inert gas as well. SoLiAS also allows to deposit thin films in integrated UHV chambers e.g. in order to provide clean substrates.

We use this assembly to study dye sensitized solar cells (DSSC). The working principle of the DSSC and its electronic interface structure are shown schematically in Fig. 2. In our case we first have to deposit polycrystalline TiO_2 from the single molecular precursor titanium-tetraisopropoxide TTIP. The sensitizer Ru-dye molecules (Fig. 2) are then chemisorbed to the TiO_2 surface from ethanol solution. A broad S2p emission is measured for a dry dye layer (spectrum A in Fig. 3a). A drastic effect on the line shape is observed upon co-adsorption of acetonitrile, the solvent used in the DSSC: The line width is dramatically reduced and after initial damping, the intensity increases albeit more acetonitrile has been adsorbed (spectra B and C in Fig. 3a).

The S2p core level changes are accompanied by changes in the valence band region. The highest occupied electron state HOMO of the dye molecule shows increased intensity while the substrate gap states which are due to TiO_2 surface defects of Ti3d character are quenched (spectra A-C in Fig. 3b).
A simple geometric model can be deduced from these measurements (Fig. 3c): The sensitizer Ru-dye molecule shows a distinct asymmetry with the HOMO located around the NCS groups and the lowest unoccupied electron state LUMO around the COOH groups, two of which are known to bind to TiO_2 under deprotonation (Fig. 2). In the absence of solvent, the Ru-dye molecules lie disordered on the TiO_2 surface with their NCS groups interacting with the surface and neighbouring sensitizer molecules causing statistical broadening of the S2p level. Co-adsorbed solvent molecules evidently penetrate the sensitizer layer and force the Ru-dye molecules to stand upright pointing their NCS groups away from the substrate, thereby reducing the statistical broadening. The geometric rearrangement of the dye molecules is accompanied by a change in the binding energy of their valence states as indicated by the line following the HOMO position in Fig. 3b. The solvation induced alignment is completely reversible as demonstrated by spectra D in Fig. 3a,b which have been taken after desorption of acetonitrile at room temperature.

We consider the structural reordering with the HOMO orbital pointing towards the bulk of the electrolyte (I_2/I_3^- in acetonitrile) as most important for the photovoltaic efficiency of the solar cell. It promotes the refilling of the HOMO with an electron from the electrolyte after light absorption and electron injection into TiO_2 and thereby prevents the back-reaction of the photo-excited electron (Fig. 2). In addition, recombination of photogenerated electron hole pairs is considered

References:

*[1] W. Jaegermann and Th. Mayer, Solar Energy Materials & Solar Cells **83**, 371-394 (2004).*

*[2] Th.Mayer et al., J. Phys. Chem **110**, 2293 (2006) .*

Acknowledgements:

Supported by the BMBF and the DFG. We thank our research partners D. Schmeißer (TU-Cottbus), Ch. Pettenkofer, and H. J. Lewerenz (HMI, Berlin) for their cooperation.

to be minimized by reducing direct dye-dye interaction and by quenching TiO_2 surface gap states. Accordingly the solvent not only serves as the medium, in which ionic charge can move providing a closed circuitry, but plays a decisive role in the adsorption geometry of the sensitizer molecules and thereby promotes the kinetics of the photo-excited charge transfer. Current developments in DSSC to substitute the liquid electrolyte by a solid (organic) hole conductor must find a way to mimic the organizing effect of the liquid electrolyte on the sensitizer dye molecules.

The versatility of SoLiAS can be used to investigate the electronic properties of very different electrochemical interfaces.
A number of successful cooperation projects on solid / liquid interface puzzles have been realized e.g. within the framework of INTERCALNET (European Research and Training Network). Further investigation challenges are under consideration and interested collaboration partners are invited to directly contact the authors.

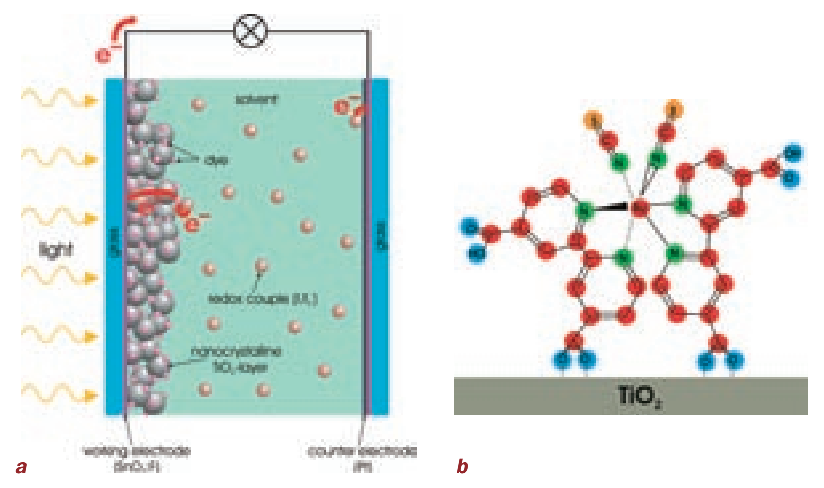

Fig. 2:
(a) Working principle of the dye sensitized solar cell DSSC. TiO_2 nanoparticles are sensitized to sunlight with a monolayer of dye molecules. By absorption of sun light an electron is excited in the dye and injected to the conduction band of TiO_2. (b) Molecular structure of the sensitizer Ru-dye molecule.

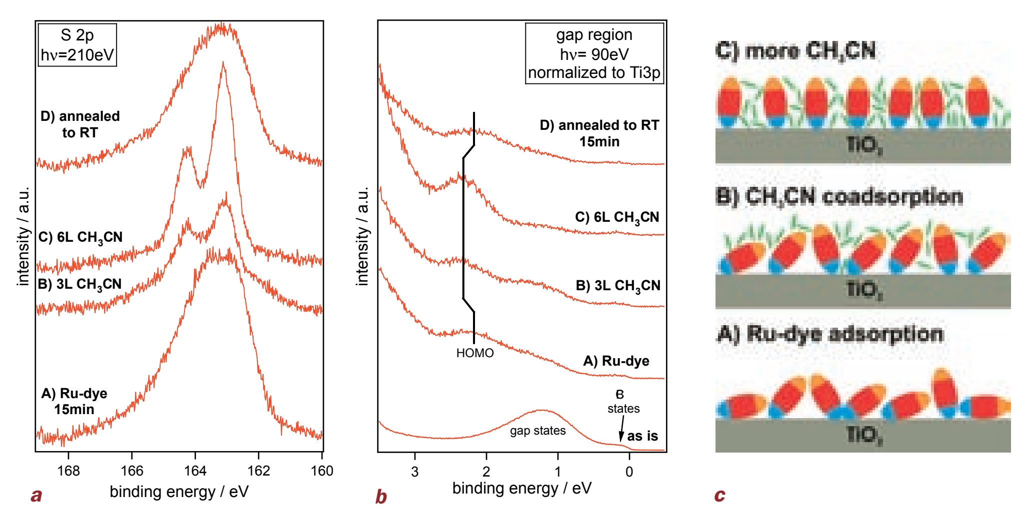

Fig. 3:
(a) Photoelectron spectra of the S2p level of the sensitizer NCS-group taken with highest surface sensitivity at 120K substrate temperature. (b) Corresponding electronic states in the bandgap of TiO_2 (E_F-E_{VB}=0-3.2eV binding energy). (c) Cartoon of the organizing effect the solvent exerts on the sensitizer molecules.

(A) Sensitizer adsorbed from ethanol solution, (B) and (C) acetonitrile co-adsorbed, (D) acetonitrile desorbed.

Contact:
Thomas Mayer
mayerth@surface.tu-darmstadt.de

Remake of ancient green

O. Hahn [1], H. Kutzke [2], M. Wilke [3]

[1] Bundesanstalt für Materialforschung und -prüfung, Berlin

[2] Fachhochschule Köln

[3] Universität Potsdam

'Abraham and Isaac', 18th century, South Tyrol (Hall); with courtesy of 'Sammlung Steiner', Munich

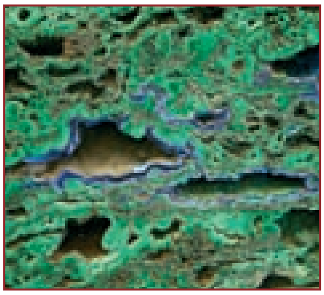

Fig. 1: Malachite with impurities of azurite, museum for natural history, Vienna.

In the late 18th century in Hall/South Tyrol reverse painting on glass with an impressive green were made. There exists a variety of these works of art containing the so called '*Haller Grün*'. The aim of this study was to find out the composition of this special green. The scientific investigation of historical pigments gives unique insight into painting techniques and their evolution through time and geographic location. In addition, the analyses of alteration mechanisms provide essential information for restoration and conservation treatments.

Copper compounds were widely used as green and blue pigments from ancient times until the 19th century. Natural minerals such as malachite (e.g. $CuCO_3$ x $Cu(OH)_2$, Fig. 1) and azurite ($2CuCO_3$ x $Cu(OH)_2$) were used as well as artificially produced compounds (verdigris, $Cu(CH_3COO)_2$ x $2Cu(OH)_2$). A lot of treatises and recipes for the preparation of copper pigments still exist, starting from the *naturalis historiae* of Pliny and medieval treatises up to the technical literature of the 19th century [1]. In the course of time numerous different copper compounds were used in art and crafts (Fig. 2). Furthermore, copper pigments can undergo chemical reactions with the binding media, with other pigments, or with the substrate (e.g. paper, parchment) – these processes may cause damages. The knowledge of the chemical composition of the pigments as well as the reaction products is essential to elucidate the damaging process.

The advantage of X-ray absorption spectroscopy is the non-destructive identification of a very special group of pigments: the characterisation of different artificial and natural green copper pigments. Pigments were usually identified by means of X-ray diffraction (XRD), X-ray fluorescence (XRF), Infrared (IR)-, and Raman spectroscopy. Due to the fact that interesting copper pigments as well as their corrosion products consist mainly of Cu and light elements (such as C, H, O), it is not possible to distinguish them by means of XRF. Some pigments and their corrosion products are not crystalline and therefore not detectable by XRD. The concentration of the copper compounds is often very low in comparison to the concentration of the binding media, and so the application of IR and Raman spectroscopy is often difficult.

Due to the fact that the shape of various XANES-NEXAFS structures reflect the influence of the chemical environment of the element copper, we started X-ray absorption measurements (XAFS) at the Cu K-edge in order to distinguish different copper pigments. Artificial samples were prepared following historical recipes [2]. The experiments were carried out at the bending magnet beamline KMC-2. A double Si/Ge gradient crystal (111) monochromator was used for monochromatization of the primary beam providing an energy resolution of $E/\Delta E = 4{,}200$.

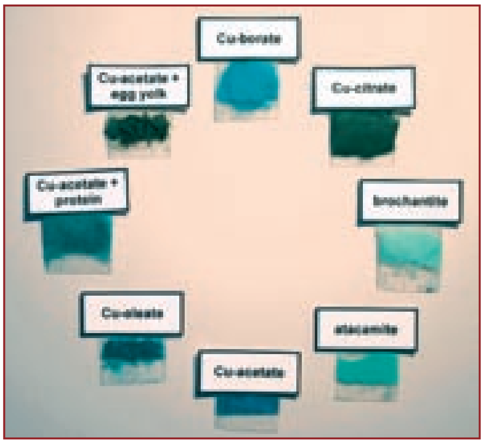

Fig. 2: The wide range of copper pigments.

References:

[1] R. D. Harley, Artists' pigments c. 1600-1835, Archetype Publications Ltd. (2001).

[2] D. Oltrogge, http://db.re.fh-koeln.de:2200

[3] A. Erko et al., Proceedings of the 11th US National Conference on Synchrotron Radiation Instrumentation, ***vol. 521****, 415-418 (2000).*

Acknowledgements:

The authors would like to thank Alexej Erko for his support, Timo Wolff for assistance during the measurements, Simone Bretz and Hans-Jörg Ranz for providing original samples, Prof. Portsteffen and his students for providing samples from various paintings.

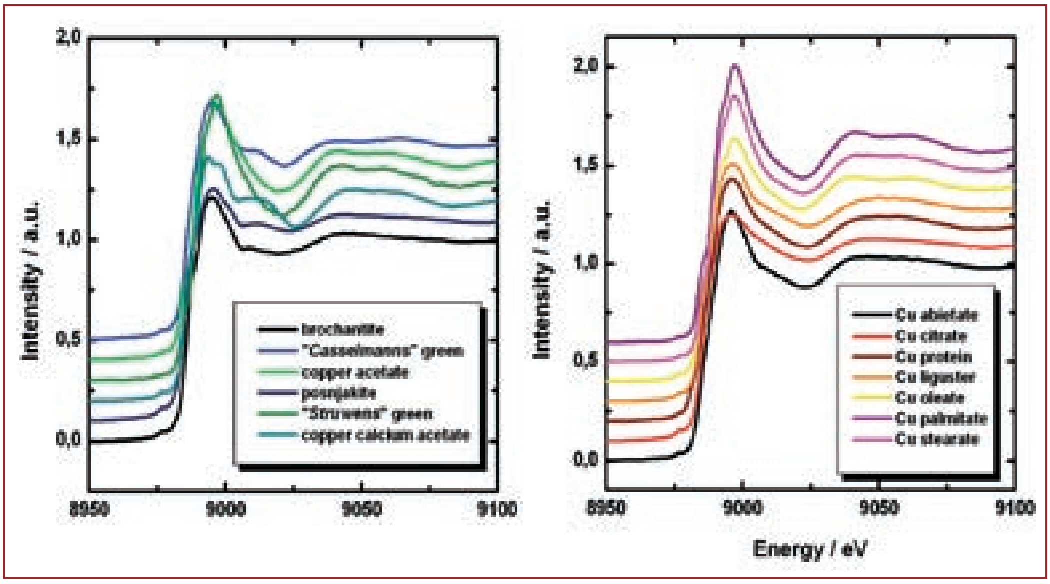

Fig. 3:
X-ray absorption spectra (Cu K-edges) of copper pigments and alteration products.

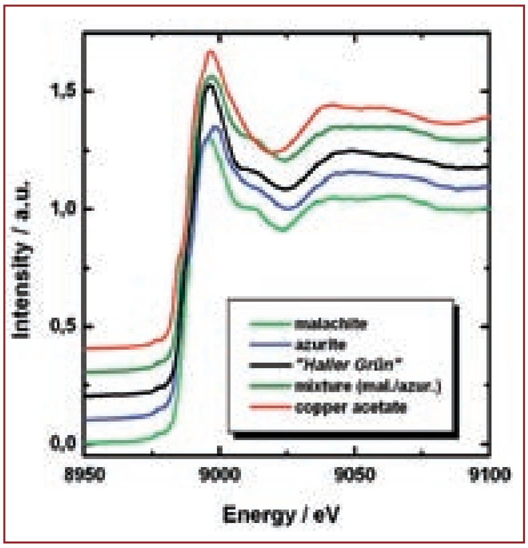

Fig. 4:
X-ray absorption spectra of 'Haller Grün', malachite and azurite.

After the monochromator the beam was focussed horizontally by a toroidal mirror resulting in a spot size of 250 x 600 µm [3]. Micro-XANES spectra at the Cu-K-edge were collected in fluorescence as well as in absorption mode using an energy step width around the absorption edge of 0.5 eV. The XANES spectra were corrected for background absorption by substracting a linear function that was fitted to the spectral region before the edge. They were then normalized for atomic absorption by fitting an arc tangent function and a Gaussian function to the spectra and setting the arc tangent function to equal step height for all spectra.

Figure 3 shows some XANES spectra of different copper green pigments - and - in addition XANES spectra of copper organic compounds. These first results demonstrate that it is possible to distinguish different pigments as well as different alteration products with respect to the fine structure of the XANES region. However, a significant energy shift of the Cu K-edge was not observed because Cu shares the same oxidation state (Cu^{2+}) in all the investigated compounds.

In order to apply these findings to original samples we investigated the green colour of the reverse painting on glass 'Abraham and Isaac'. Initial XRF measurements showed that '*Haller Grün*' is a mixture of lead white and a copper green pigment (without sulphur or chlorine), and following XAFS studies allowed to identify the green copper pigment as a mixture of malachite and azurite (Fig. 4, malachite : azurite; 3:1).

The XANES spectra of the new mixture fits the one of the original 'Haller Grün' already very well, helping the remake of the ancient paint. This is essential for the restoration of glass paintings of this period. Micro methods which allow the non-destructive analyses of cross-sections are important in the investigation of painting layers, and in future XAFS may complement well established analysing techniques such as XRD, XRF, IR- , and Raman spectroscopy.

Contact:
Oliver Hahn
oliver.hahn@bam.de

If the wrapping gets tight: How microcontainers for drug delivery are formed

K. Köhler [1], C. Déjugnat [2], M. Dubois [1], G. B. Sukhorukov [3], H. Möhwald [1], T. Zemb [4], P. Guttmann [5]

1
Max-Planck-Institut für Kolloid- und Grenzflächenforschung, Potsdam

2
Institut de Chimie Séparative de Marcoule,
Bagnols-sur-Cèze, France

3
Queen Mary University of London, London, UK

4
DRECAM/SCM, CEA/Saclay,
Gif-sur-Yvette, France

5
Georg-August-Universität Göttingen c/o BESSY

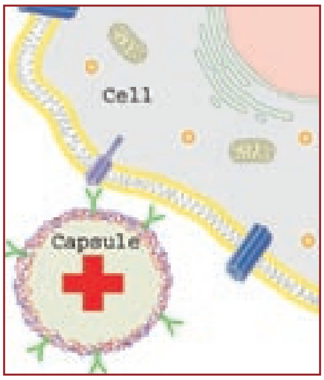

In our everyday life we encounter all-around wrapped materials like nicely packed presents, wine in bottles or bird eggs. All these packings have the function to store and protect substances from environmental influences. Nature offers also infinite examples in the microscopic world such as all different types of cells. However, also man tries to wrap substances on the microscopic scale by preparing different kinds of nano- or microcapsules. The main aims for this bold venture, besides the creation of an artificial cell, are to run reactions with only a few molecules, to generate microsensors or even to deliver drugs to targeted places within the body. Nowadays, microcapsules are already used as carriers in the pharmaceutical, cosmetic, food, textile, adhesive, and agricultural industries.

One very versatile method to prepare microcapsules is the so-called layer-by-layer (LbL) technique [1] consisting of alternating deposition of oppositely charged polyelectrolytes onto charged particles and subsequent dissolution of these templates [2]. The wall thickness can be tuned in the nm range and a vast scope of different functional materials can be incorporated into the wall.

LbL capsules consisting of four double layers of poly(diallyldimethylammonium chloride) (PDADMAC) and poly(sodiumstyrene sulfonate) (PSS) as positively and negatively charged polyelectrolytes, respectively, are temperature sensitive. They irreversibly but regularly shrink upon heating from 4.5 µm to finally 1.3 µm accompanied by an increase of wall thickness [3]. The higher the incubation temperature or the longer the incubation time the more the capsule size is reduced. Scanning electron micrographs of dried capsules show that the initially collapsing capsules become more stable after heating until they appear as solid particles at the endpoint of shrinkage (20 min 80 °C; Fig. 1). The rearrangement of the multilayer can be used for the encapsulation of materials since we found that the shrinkage reduces the permeability of the capsule wall significantly.

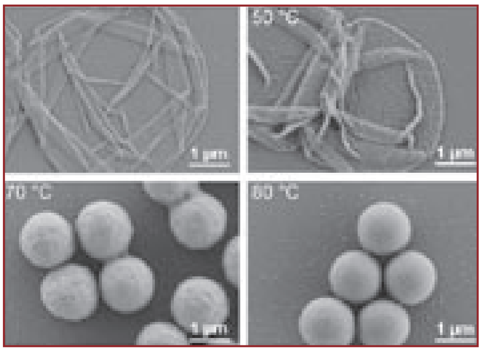

Fig. 1:
Scanning electron microscopy images of dried $(PDADMAC/PSS)_4$ microcapsules, which shrink upon heating in aqueous medium.

Conventional methods to study the multilayer capsules are confocal, electron, and atomic force microscopy. However, with none of them it is possible to get information about the thickness and composition of capsule walls in aqueous media. We used transmission X-ray microscopy (TXM) at the beamline U41/1-TXM [4], which allows the observation of soft matter in aqueous environment with a high resolution of 20 nm. In the so-called 'water window' (E = 284-543 eV), the water molecules absorb less than carbon-containing substances, giving a natural contrast. TXM images of differently shrunk $(PDADMAC/PSS)_4$ capsules are shown in Fig. 2. They clearly show the reduction of size and the concomitant increase of shell thickness upon heating. It is the first in situ proof that the capsules are no longer hollow at the endpoint of shrinkage, but they have converted into solid balls in aqueous medium. From these TXM images we determined the external radius R_e as well as the membrane thickness h and calculated the shell volume V (Fig. 3). The continuous decrease of this value with decreasing capsule size could correspond either to a densification of the polymeric network, and thus a reduction of the water content or to a loss of polyelectrolyte material. We analyzed the radial profiles of the capsules. The absorption of monochromatic X-rays by matter follows the Lambert Beer law. At fixed energy, and chemical composition, the transmittance can be expressed as $T = e^{-\mu(Z,E)\cdot\rho\cdot D}$ where ρ is the density of the absorbing material, D the thickness and $\mu(Z,E)$ a mass absorption coefficient depending on the X-ray energy (E) and the chemical composition of the sample (Z).

References:

*[1] G. Decher, Science **277**, 1232 (1997).*

*[2] E. Donath et al., Angew. Chem. Int. Ed. **37**, 2201 (1998).*

*[3] K. Köhler et al., J. Phys. Chem. B **109**, 18250 (2005).*

*[4] P. Guttmann et al., J, Phys. IV **104**, 85 (2003).*

*[5] R. Müller et al., Macromolecules **38**, 9766 (2005).*

Acknowledgements:

The authors thank Luc Belloni for useful discussions and the German-French European Network 'Complex Fluids: From 3 to 2 Dimensions' for funding.

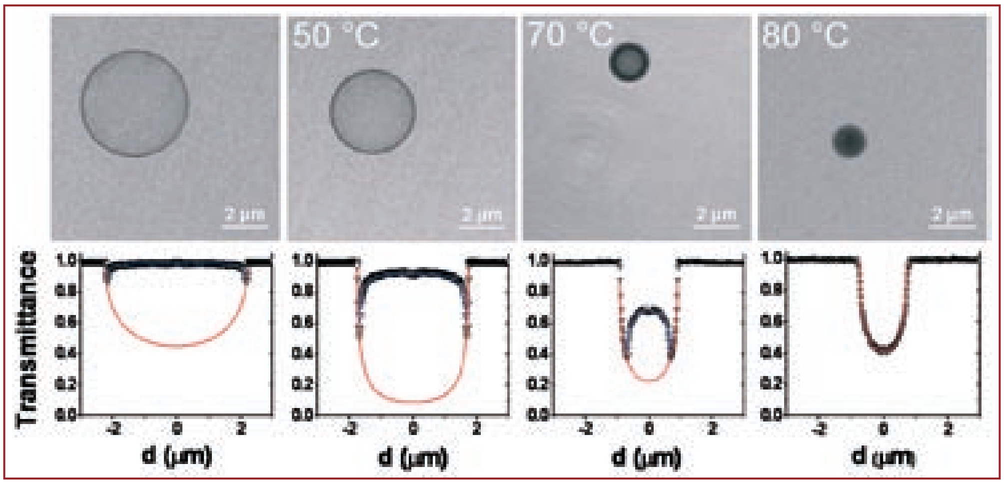

Fig. 2:
TXM micrographs of differently shrunk (PDADMAC/PSS)$_4$ capsules after heating for 20 min in water and the corresponding fitted transmittance profiles.

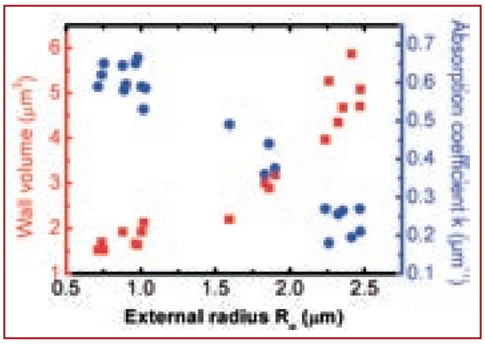

Fig. 3:
Wall volume and experimental absorption coefficient k of (PDADMAC/PSS)$_4$ capsules shrunk to different diameters as a function of the external radius.

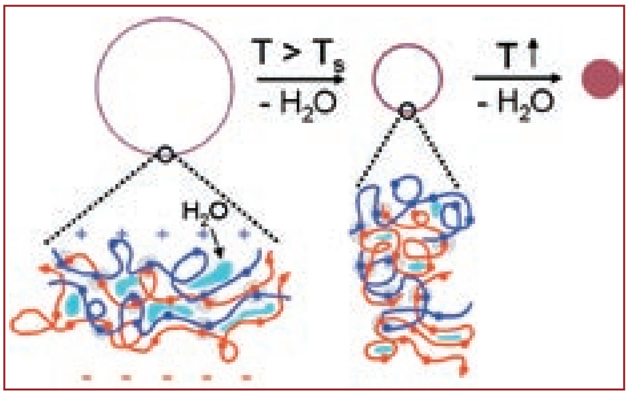

Fig. 4:
Schematic representation of the mechanism of heat-induced shrinkage of polyelectrolyte multilayer capsules in aqueous environment after exceeding the softening transition temperature of the polymer network.

We based our analysis on the simple model of a hollow capsule with constant density of the membrane. The expression of T along a radial profile becomes then:

$$T(d) = \exp[-2k(\sqrt{R_e^{\,2} - d^2} - \sqrt{R_i^{\,2} - d^2})]$$

for $d \le R_i$ and

$$T(d) = \exp[-2m(\sqrt{R_e^{\,2} - d^2})]$$

for $R_i \le d \le R_e$,

where R_e and R_i are the external and internal radii, respectively, and d the distance to the center of the capsule, assuming a perfect sphere. In all cases, this model fits the extracted radial profiles well (Fig. 2). Therein the blue line represents the fit given by the first equation and the red line that of the latter equation. From this analysis one obtains the absorption coefficient $k = \mu \cdot \rho$. It increases from $k = 0.26\ \mu m^{-1}$ for the non-heated capsules up to $k = 0.62\ \mu m^{-1}$ for the solid balls at the final stage of shrinkage (Fig. 3). Since the chemical composition as well as the used X-ray energy is constant for all samples, µ does not change with the capsule diameter, meaning that the density of the polyelectrolyte multilayers ρ increases upon heating, and that the walls undergo a partial dehydration during their rearrangement. A quantitative analysis of the amount of water within the multilayers by using $\mu = 1\ cm^2 \cdot g^{-1}$ and $\rho = 1.2\ g \cdot cm^{-3}$ for pure polyelectrolyte complex results in a decrease of water content from 78 % to 48 %. Calculations of the capsule mass before and after heat treatment show that no material is lost during shrinkage. The corresponding mechanism can be explained as following (Fig. 4): At room temperature polyelectrolyte multilayers are kinetically stabilized by multiple and thus strong bonding between the oppositely charged ionic sides. Especially, free-standing films of capsules are forced in an arrangement with an extremely high surface tension. Upon heating, more and more neighboring ionic bonds break, so that the polyelectrolytes get an increased degree of mobility and can rearrange into an energetically more favored state with a decreased interface to water. The consequently smaller surface tension favors an arrangement as solid ball. At a temperature of 35-40 °C enough ionic bonds for a rearrangement of the multilayer are broken. This was measured for (PDADMAC/PSS)$_4$ capsules by means of differential scanning calorimetry (DSC) and colloidal probe atomic force microscopy [5]. The loss of water during capsule shrinkage also decreases the polymer - water interface and is together with the thickness increase the reason for the strongly decreased permeability. This is the basis for the encapsulation by heat shrinking.

Contact:
Karen Köhler
karen.koehler@mpikg.mpg.de

1
Hahn-Meitner Institut,
Berlin

2
TU Berlin

Towards artificial bone marrow: 3D matrices to cultivate stem cells

A. Haibel [1], H. Freidank [1], A. Berthold [2], J. Banhart [1], H. Schubert [2]

Tomographic image of a human vertebra.

Aggressive chemo therapy kills not only tumour cells but also weakens the immune system at the same time. The regeneration of the immune system is only possible by the insertion of stem cells (Fig. 1). As a result, there has been an increasing interest towards to extract stem cells of a patient before a chemo therapy, to cultivate them *ex vivo* and give them back in a sufficient quantity after the therapy. But the *ex vivo* cultivation of stem cells is difficult, because successful stem cell growth relies heavily on the cultivation environment. Stem cells are located in the umbilical cord and the bone marrow. They are responsible for the regeneration of blood and the refreshment of the body's immune system. One of the main objectives of our research in external cultured stem cells is the optimization of their *ex vivo* cultivation. Successful results of this project would allow for improved treatment in cancer therapies.

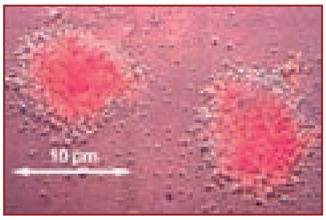

Fig. 1: Light microscopic image of bone marrow stem cells.

The basis for a successful *ex vivo* cultivation of the stem cells is to find an appropriate culture medium. Ceramic foams have a similar structure than human bones. Therefore an obvious idea is to use such foams as 3D matrix for the cultivation of stem cells. The 3D porous structure of the ceramic foams would provide for a better cultivation environment than flat cell cultivation dishes [1,2]. To guarantee an adequate supply of the cells with nutrients a good penetrable, large-pored foam structure is required. For this reason, special attention is needed on the size of the pores and their interconnection.

In this project, ceramic foams are made using ceramic powder Al_2O_3 with a purity of 99.99% and particle size between 0.1 and 0.3 µm. A chemical modified protein (bovine serum albumin) is used as foaming agent together with a dispersing agent and demineralised water [3,4,5]. From the food chemistry it is known that an acetylation or a glycation of proteins with sugar yields to enhanced foaming and emulsifying properties, i.e. to an increase of the foaming ability. All components are mixed and foamed by a ball mill. The ceramic foam precursor material is then processed in a microwave or in a drying chamber alternatively. The ceramic foams are sintered in a high-temperature furnace at T=1,600°C as the last step.

The three-dimensional investigation of the foamed ceramic samples were carried out using high-resolution synchrotron radiation tomography at the BAMline. Absorption tomography is based on the detection of radiation attenuated by the samples for many different angular positions (Fig. 2). After passing through the samples, the monochromatic X-rays (E=25 keV) were converted to visible light using a Gd_2O_2S scintillator. The optically magnified images (image voxel size 3.6 µm) were then captured by a 2,048 × 2,048 pixel CCD camera. Depending on the required spatial resolution, up to 2,400 radiographic images are needed. This results in a set of projections which are used for reconstructing a complete 3D image representing the local X-ray attenuation coefficients in the sample [6].

References:

*[1] N. Banu et al., Cytokine, **13**, 349 (2001).*

*[2] J. Bagely et al., Exp. Hematol., **27**, 496 (1999).*

*[3] I. Garrn et al., J. Eur. Ceram. Soc. **24**, 579 (2004).*

*[4] K. L. Franzen and J. E. Kinsella, J. Agric. Food Chem. **24**, 788 (1976).*

*[5] A. Banie et al., J. Agric. Food Chem. **40**, 200 (1992).*

[6] A. C. Kak and M. Slaney, Principals of Computerized Tomographic Imaging, IEEE Press, New York (1987).

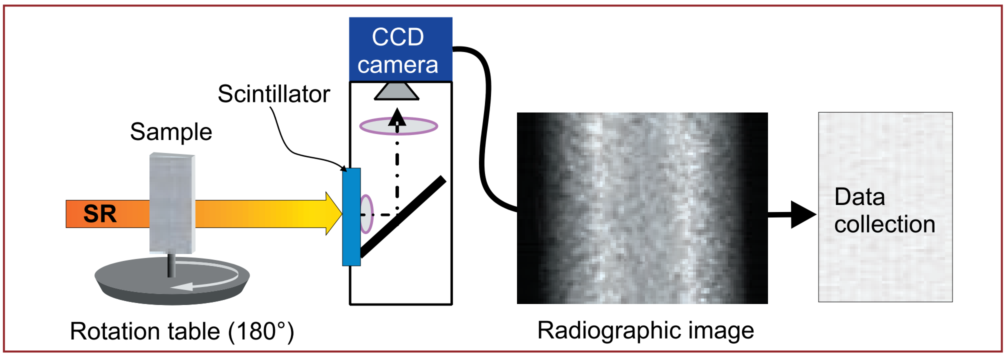

Fig. 2: Sketch of the tomographic setup.

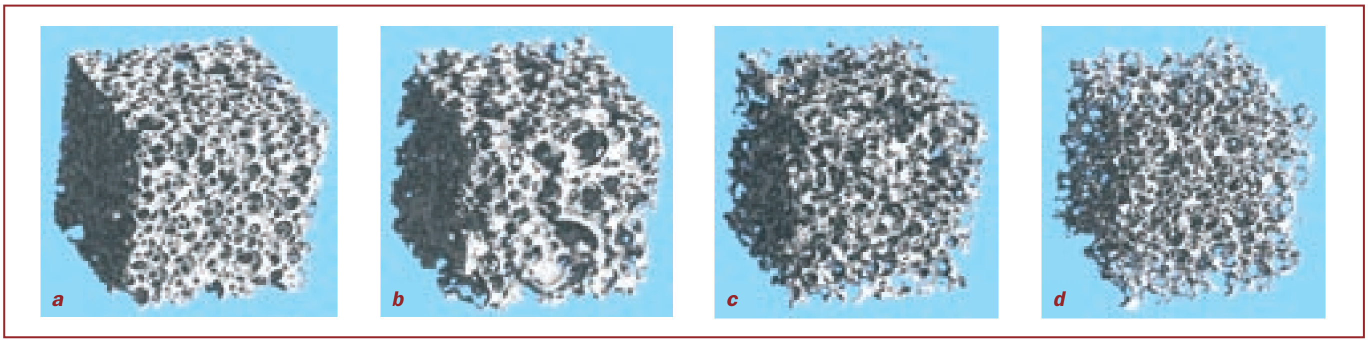

Fig. 3:
Ceramic foam structure after the sintering process for four different prepared samples. Edge lengths of the cubes are 1.44 mm. (a) Only the original components were used. (b) A dispersing agent was added to the original components. (c) Furthermore the protein was modified by glycation with sugars. (d) The foam precursor material was processed in a drying chamber.

Resulting images are displayed in Fig. 3. The foams illustrated in Fig 4 were prepared in four different ways. Only the original components were used in foam a). The precursor material was processed by micro wave radiation before sintering. Here the mean pore size and the interconnections are much smaller compared to the other foams. For the foam in Fig. 3b), a dispersing agent was added in the precursor material. The effect is a broader pore size distribution, but the interconnections are still small. By using a glycated protein for foaming (Fig. 3c), the mean pore size is larger as in the case of foam a and b and the interconnections of the pores are increased. The foam displayed in Fig. 3d was also prepared with glycated protein but additionally processed in a drying chamber instead of a micro wave. In that case, the mean pore size is increased too and the pore interconnections are very large.

For a quantitative 3D image analysis of the tomographic images the pores were identified and separated into Boolean images by using appropriate grey scale thresholds. Two transformations (Euclidean distance transformation and Watershed transformation) in an image analysis software were used to process the image. The interconnected pores were separated (Fig. 4) and the pore size distributions and pore shapes were analysed.

The quantitative pore size analysis is plotted in Fig. 5. The qualitative results of Fig. 3 are confirmed. By preparing the samples using a dispersing agent and chemical modified proteins as well as by sample processing in the drying chamber the mean pore size, the pore size distribution and the porosity increase whereas the number of pores decreases.

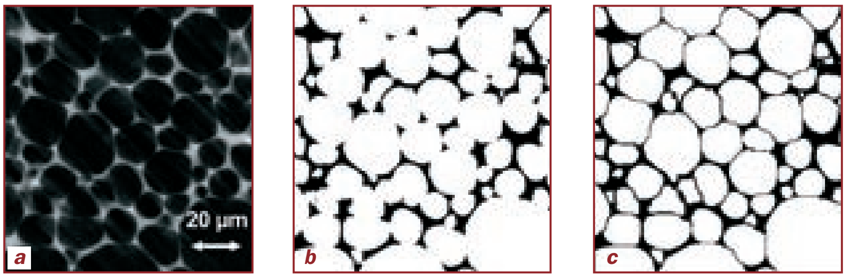

Fig. 4:
2D slice of a tomographic foam image, (a) Original grey value image, (b) Boolean image, (c) final, Watershed transformed image.

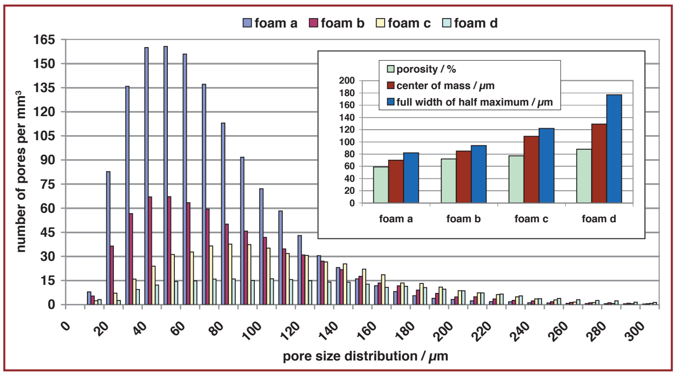

Fig. 5:
Pore size distribution of the four ceramic foams in Fig. 4. In the cut-out the porosity, the center of mass and the full width of half maximum for the four foams are plotted.

Based on these results, we will be able, to adapt the ceramic foam shape and pore size individually at the requirements of each specific stem cell line. The appropriateness of the new tailored substrate material will be proofed in cultivation experiments, now.

Contact:
Astrid Haibel
haibel@hmi.de

CIMEX Development AG,
Basel, Switzerland

Spot the difference! How to create the right medicine

M. Fischer

Pharmaceuticals are often administered as tablets. Those pills contain an active pharmaceutical ingredient (API) and some filling substances or additives (excipients). Pharmaceuticals can exist in various solid forms (polymorphs) having different chemical and physical properties including different crystalline phases as well as solvates and amorphous solids. These polymorphisms are one reason of the variability of drug performances, and industrial suppliers face the challenge of producing drugs in consistent quality. Among other issues, manufactures have to make sure that a form is not altered during the different production processes.

Beyond the quality aspect, different forms of a drug can exhibit entirely different biological activities, e.g. due to solubility in the human physiological environment (gastric juice or intestinal juice). Sometimes this leads to manifold activity increase of a form in the human body but can also cause severe side effects. Moreover, drugs sometimes change from one form to another on the shelf at the pharmacists' leading to ineffective medication.

But for a pharmaceutical company polymorphism is also an issue of intellectual property. An alternate solid state form can be regarded as a new invention and can be subject of a patent. And there are several instances where a pharmaceutical company has acquired a patent on a particular polymorphic form to extent beyond the expiry of the API's patent. Generic companies are therefore obliged to use an alternative form in order to get the product granted for marketing without taking the risk to get into patent litigation with the innovator.

Several analytical methods are commonly used to determine polymorphism in a pharmaceutical drug substance and drug product. Among these, X-ray diffraction is the preferred method for polymorphism monitoring. Since most drug substances are obtained as microcrystalline powders, X-ray powder diffraction, in particular, is the predominat tool for studying these polycrystalline materials. During the most common evaluation of drug substance, it is usually sufficient to establish only the polymorphic identity of the solid and to verify that the isolated compound is indeed of the desired structure.

However, things can get more complicated when it is necessary to investigate the polymorphism of the substance in the finished drug product, which also contains high amounts of excipients (e.g. crystalline

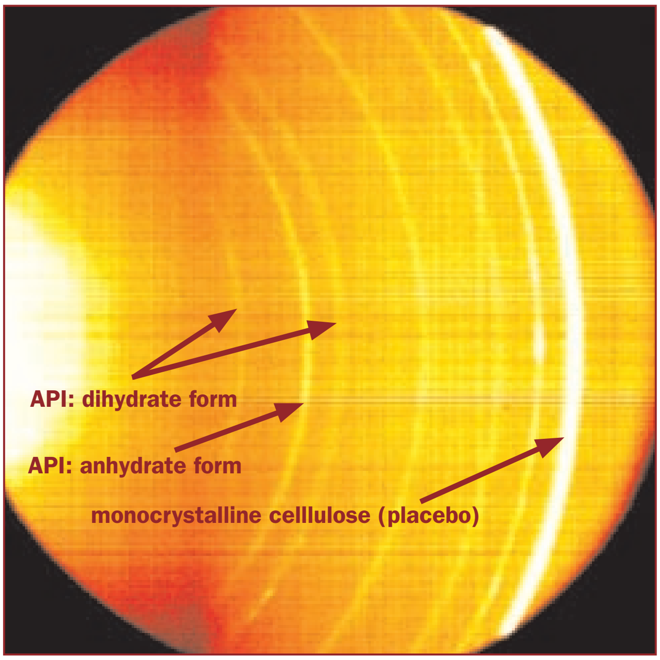

Fig. 1:
Two-dimensional XRD pattern of tablet powder containing 1.0% of dihydrate drug substance, 4.0% of anhydrate drug substance and 95% of cellulose.

References:

[1] A. Erko et. al., Nucl. Inst. Meth. ***A467-468****, 358-361 (2001)*

[2] N.V. Phadnis et al., J. Pharm. Biomed. Anal. ***15****, 929-943 (1997)*

Acknowledgements:

We thank N. Darowski and I. Zizak (HMI Berlin) for providing the BRUKER HiStar detector and for their help in the measurements

cellulose or lactose). Since the concentration of the drug compound can be much below 1%, the sensitivity of the conventional techniques is often not sufficient. For this purpose a high sensitive X-ray powder diffraction method was established using the KMC-2 beamline [1]. We aimed to evaluate the smallest amount of a polymorphic form which can be detected by the X-ray powder diffraction using synchrotron radiation.

Our model consisted of a pharmaceutical active ingredient (API) mixed with a placebo component (cellulose) in a finished tablet. The API is supposed to be in the anhydrous state but it can transform into the dihydrate form after some time under stress conditions within the tablet. Fig. 1 shows a two dimensional XRD-pattern at the beam energy of 8,048 eV. The conical diffraction maxima are indicated on a screen by bright lines. The pattern can be integrated in a digital form along the circular-shaped reflexes with an angular resolution of 0.01° in used experimental geometry. All diffraction maxima can be attributed to either the placebo component, or the API in the anhydrate and dihydrate form, respectively.

A sample containing the API in anhydrate and dihydrate form was employed to compare a conventional diffractometer with the KMC-2 station (Fig. 2). The graph shows that within a 100-fold shorter measuring time, the sensitivity of the XRD pattern at KMC-2 in combination with the Bruker “Hi Star” detector was drastically enhanced.

For the evaluation of the method sensitivity, dry mixtures of the pharmaceutical finished product were made by mixing the corresponding placebo mixture with known amount of API in anhydrate and dihydrate form. The nominal amount of API in the tablet is 5% dominated by the anhydrous form with additions of small amounts of dihydrate (0.05 - 1% total amount) in order to simulate a 1% - 20% transformation between anhydrate to dihydrate. A 2% transformation to dihydrate could easily be detected within a measuring time of 4,000 seconds. This proportion of dihydrate corresponds to 0.1% (w/w) with respect to the tablet powder, which is a 10-fold enhancement of the sensitivity compared to conventional X-ray diffraction [2]. The XRD signals of the different samples containing 20%, 10%, 5% and 2% of transformed dihydrate were extracted (Fig. 3b). From this plot we derived a calibration curve which allows quantifying the amount of dihydrate transformation stressed tablet samples.

Optimization is still ongoing in order to further enhance the sensitivity of the method.

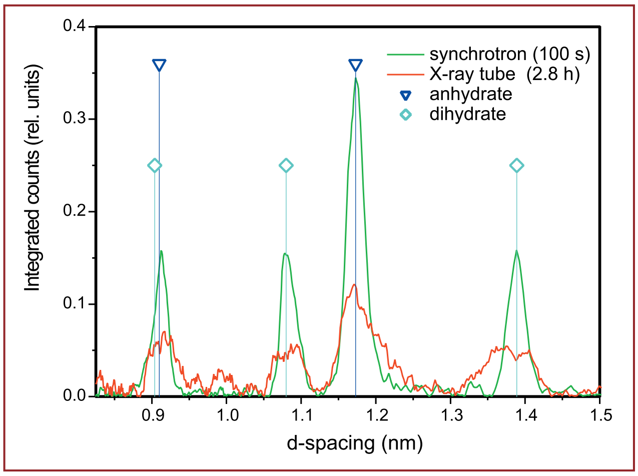

Fig. 2:
Area-integrated XRD pattern of a reference sample containing the API in anhydrate and dehydrate form using a conventional X-ray diffraction apparatus and the enhanced X-ray method using synchrotron radiation.

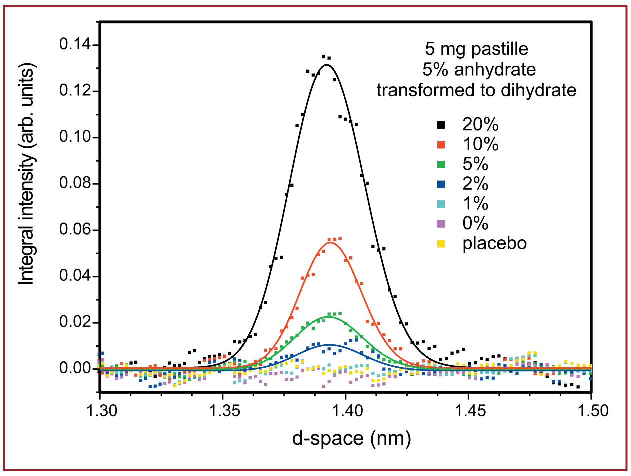

Fig. 3:
Diffraction peak of the dihydrate form in the tablet powder with various amounts of the dihydrate form in the anhydrous active substance.

Contact:
Marc Fischer
m.fischer@cimex.ch

The wolf in the sheep skin: How endosialidases unmask pathogens and tumours

K. Stummeyer[1], A. Dickmanns[2], M. Mühlenhoff[1], R. Gerardy-Schahn[1], R. Ficner[2]

[1] Medizinische Hochschule Hannover

[2] Georg-August-Universität Göttingen

Molecular mimicry is a powerful strategy used by some microorganisms to escape the immune defence reactions of the host organism. These pathogens cover their surfaces with structures that are identical to those in the host organism and thus blind the immune system. This kind of virulence strategy is used by *Escherichia coli* K1 (*E. coli* K1), a neuroinvasive bacterium that causes sepsis and meningitis in newborns.

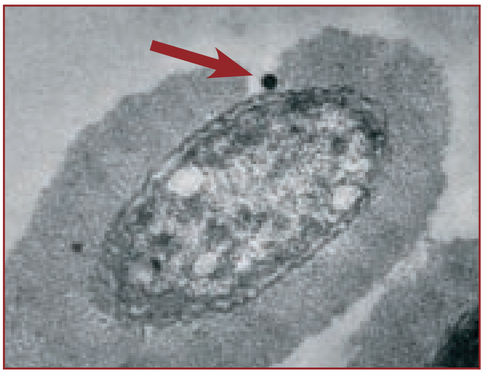

Fig. 1: Electron micrograph of a bacteriophage particle (arrow) penetrating the thick polysaccharide layer of an encapsulated bacterium.

The bacterial surface is encapsulated by poly-α2,8-sialic acid (polySia), a large carbohydrate polymer that plays an essential role during brain development of higher vertebrates [1]. Despite its protective role in the host, polySia is also the Achilles heel of the bacterium. PolySia provides the receptor for specialized bacteriophages, which infect and kill *E. coli* K1. These viruses carry spike proteins, so called endosialidases, which bind and depolymerise the polySia capsule (Fig. 1).

Phage-borne endosialidases are the only known enzymes that specifically degrade polySia and have become widely used tools to unravel the biological role of this carbohydrate polymer. PolySia has been implicated in many physiological processes like neurogenesis, cell migration, axonal outgrowth and synaptic activity including learning and memory. However, polySia also plays an important pathophysiological role. Aggressive tumours of neuroectodermal origin use polySia in a similar way as *E. coli* K1 to hide from attacks of the immune system thus supporting invasion and metastasis.

Endosialidases can unmask tumours or *E. coli* K1 bacteria to the immune system by removing the polySia skin. Initial studies have shown that the application of endosialidsases in a mouse model reduces the metastatic potential of those tumours [2], and similarly, the injection of endosialidase has been successfully used to rescue mice after infection with a lethal dose of *E. coli* K1 [3]. These examples highlight the therapeutic potential of endosialidase. We have characterized endosialidases from different *E. coli* K1 specific bacteriophages [4].

Sialidases are widespread among bacteria and eukaryotes. These enzymes usually remove single terminal sialic acid residues (hence exosialidases) from glycoproteins and glycolipids. Endosialidases specifically bind to polySia and cleave intersialyl linkages within the polymer chain, thereby releasing short sialic acid oligomers. Both sialidase families share some amino acid sequence homologies. The numerous known crystal structures of exosialidases reveal a common fold of these enzymes, a β-propeller, and when we solved the first crystal structure of an endosialidase (endoNF) at 1.9 Å resolution [5], we were not surprised to find a β-propeller as a structural unit. The functional enzyme is build-up by three identical subunits which are assembled into a mushroom-shaped structure with a prominent ‘cap’ and ‘stalk’ region (Fig. 2a). Each monomer comprises three distinct domains: a β-propeller, a β-barrel domain and an intertwined β-helix domain (Fig. 2b). This unique domain architecture combines structural elements characteristic for exosialidases (β-propeller) and bacteriophage tailspike proteins (β-helix domain). The two N-terminal domains form the compact cap of the mushroom which is dominated by the six-bladed β-propeller harbouring the active site. Within the third blade of the propeller, a nine stranded β-barrel is inserted. The C-terminal stalk region of the trimer is formed by the intertwining tailspike domains of endoNF which assemble into a triple β-helix interrupted by a small triple β-prism domain (Fig. 2a). The elongated 60 Å stalk region has presumably major impact on the unusually high stability of the enzyme. At room temperature, even the addition of

References:

*[1] Weinhold et al., J. Biol. Chem. **280**, 42971-42977 (2005).*

*[2] Daniel et al., Oncogene **20**, 997-1004 (2001).*

*[3] Mushtaq et al., Antimicrob. Agents Chemother. **5**, 1503-1508 (2004).*

*[4] Mühlenhoff et al., J. Biol. Chem. **278**, 12634-12644 (2003).*

*[5] Stummeyer et al., Nat Struct Mol Biol. **1**, 90-96 (2005).*

Acknowledgements:

The electron micrograph in Fig. 1 is courtesy of Prof. M. Bayer (taken from I.W. Sutherland, ed. (1977). Surface Carbohydrates of the Prokaryotic Cell. Academic Press).

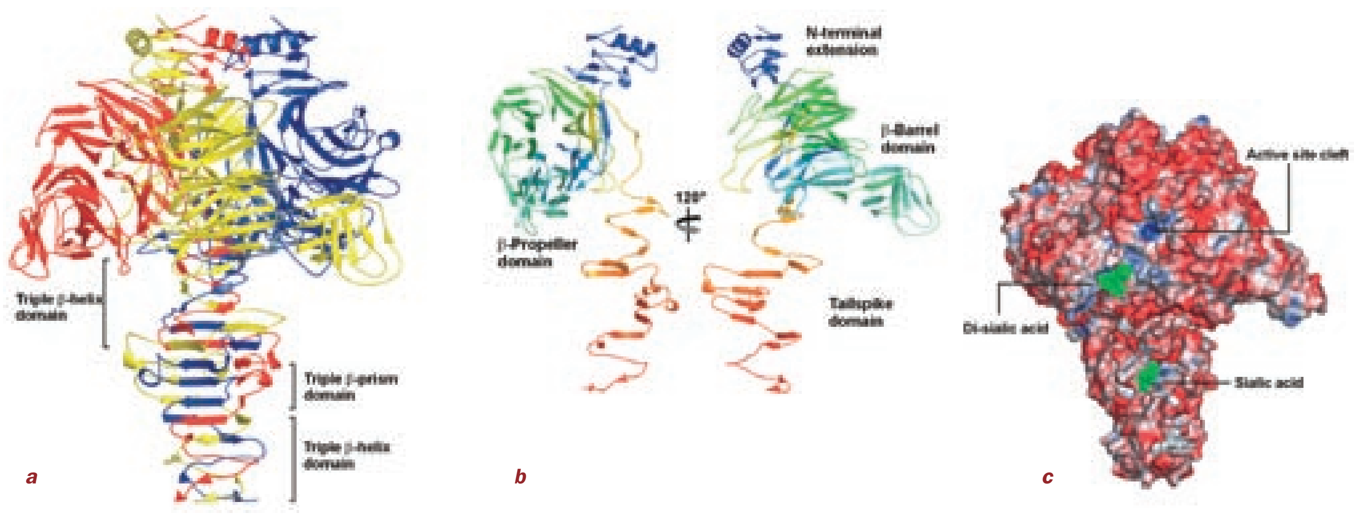

Fig. 2:
Structure of endoNF and carbohydrate binding. (a) Ribbon diagram of the homotrimer with monomers coloured in red, blue and yellow. (b) Structure of the endoNF monomer with its three domains. The chain is coloured from blue at the N-terminus to red at the C-terminus. (c) Surface representation of the endoNF homotrimer in complex with sialic acid. The molecular surface is coloured by electrostatic potential. Sialic acid residues are depicted as green spheres.

sodium dodecyl sulphate does not dissociate the trimer [4]. Inwardly pointing residues build extensive hydrophobic stacks while a substantial network of interchain hydrogen bonds additionally stabilizes intersubunit interactions.

The active site of exosialidases in the centre of the β-propeller has an equivalent site in endoNF, however, not all amino acids highly conserved in exosialidases are preserved in endoNF (Fig. 3). Interestingly, this includes an aspartic acid and a tyrosine residue, which are believed to be key residues of the exosialidase activity. For endoNF we expect therefore a reaction mechanism distinct from what is known for exosialidases which would reflect the different substrates of both enzyme families.

Another intriguing question concerns the specific binding of polySia to endosialidases and whether this knowledge would tell us also something about the active site? We performed soaking experiments with carbohydrate oligomers containing five α2,8-linked sialic acid residues and solved the structure of the enzyme-substrate complex at 2.6 Å resolution (Fig. 2c). Bound to the β-barrel domain, we identified a di-sialic acid moiety. Interestingly, the β-propeller domain of the adjacent enzyme subunit is also involved in binding and its proposed active site is most favourably positioned to cleave bound polymeric substrate. This indicates that trimerization of the endosialidase is a prerequisite for the formation of an active enzyme. Remarkably, sialic acid was also identified bound to the intertwined stalk domain of endoNF, indicating that this domain does not only function in stabilizing the catalytic trimer but is also directly involved in substrate binding. This makes sense, since bacteriophages 'land' on the bacterium with the stalk region ahead and need an early recognition of the correct 'airfield'.

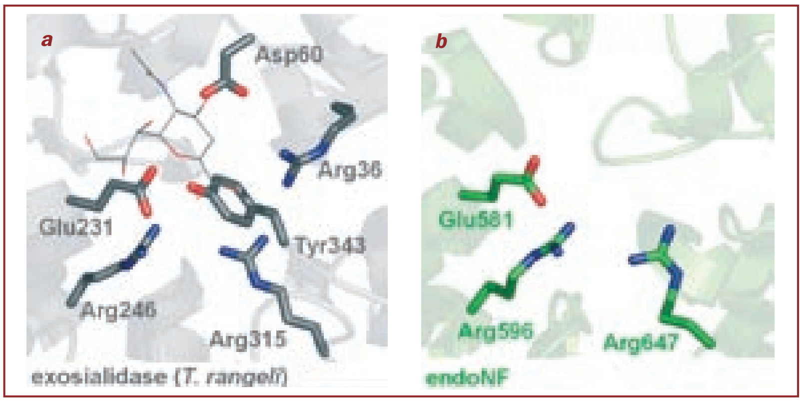

Fig. 3:
Active sites of** Trypanosoma rangeli **exosialidase with bound inhibitor DANA (a) and endo NF (b) in comparison showing three conserved residues in exo- and endosialidases.

Our studies provide insight into the molecular basis of the high substrate specificity of endosialidases and thus may help to develop strategies for the use of endosialidases as therapeutic drugs. However, the mechanism of polySia cleavage is still to be revealed and will keep us puzzling for a while.

Contact:
Rita Gerardy-Schahn
gerardy-schahn.rita@mh-hannover.de
Ralf Ficner
rficner@gwdg.de

Revealing the deadly secrets of bacteria

R. Jørgensen [1,2], A. R.Merrill [2], S. P. Yates [2], V. E. Marquez [3], A. L. Schwan [2], T. Boesen [1], G. R. Andersen [1]

[1] University of Aarhus, Denmark

[2] University of Guelph, Canada

[3] National Cancer Institute at Frederick, USA

Fig. 1: Electron micrograph of pseudomonas bacteria.

A number of pathogenic bacteria are secrete members of a family of deadly toxins, which includes the most toxic protein known to man – a single toxin molecule can kill a cell! These bacteria include pertussis, diphtheria, cholera, coli and pseudomonas (Fig. 1). Disease caused by the first three species is not observed very frequently in developed countries because of improved hygiene, but in developing countries these bacteria frequently cause epidemic outbreaks of deadly diseases. Likewise, the risk of cholera outbreaks, for example, is highly elevated following natural disasters such as the Tsunami disaster in Indonesia last year and more recently the earthquake in Pakistan. The *E. coli* and pseudomonas bacteria are observed more often in developed countries too. Pseudomonas is recognized as a serious cause of hospital infections, an emerging problem due to increasing bacterial resistance towards available antibiotics. These infections especially affect patients with cystic fibrosis, cancer or AIDS, and can cause death in up to fifty percent of the cases.

The toxins in this family are called mono-ADP-ribosylating toxins because they transfer a chemical group (an adenine diphosphate-ribosyl group) to a protein target in the human cell. Each toxin has its specific target. This modified protein is then caught in a highly active or completely inactive state giving rise to the disease symptoms. Whereas the cholera, coli and pertussis toxins targets are involved in cell signalling (e.g. leading to massive water efflux in the gut), the diphtheria and pseudomonas toxins both target an important protein involved in a fundamental cellular process – the protein synthesis.

Protein synthesis takes place on nano-machines called ribosomes in our cells. During this process the information stored in our hereditary material (encoded by DNA) is translated into functional enzymes (proteins) via an intermediate messenger molecule (messenger RNA). The messenger RNA is decoded by the ribosome and protein is synthesised during this decoding. The proteins produced on the ribosomes are involved countless different functions of the cell and each ribosome (more than a million in a cell) produces a new protein approximately every 5 minutes. The old and redundant proteins are broken down to their basic building blocks, amino acids, which serve as raw material for the synthesis of fresh proteins by the ribosomes. The entire process is crucial for the survival of the cell.

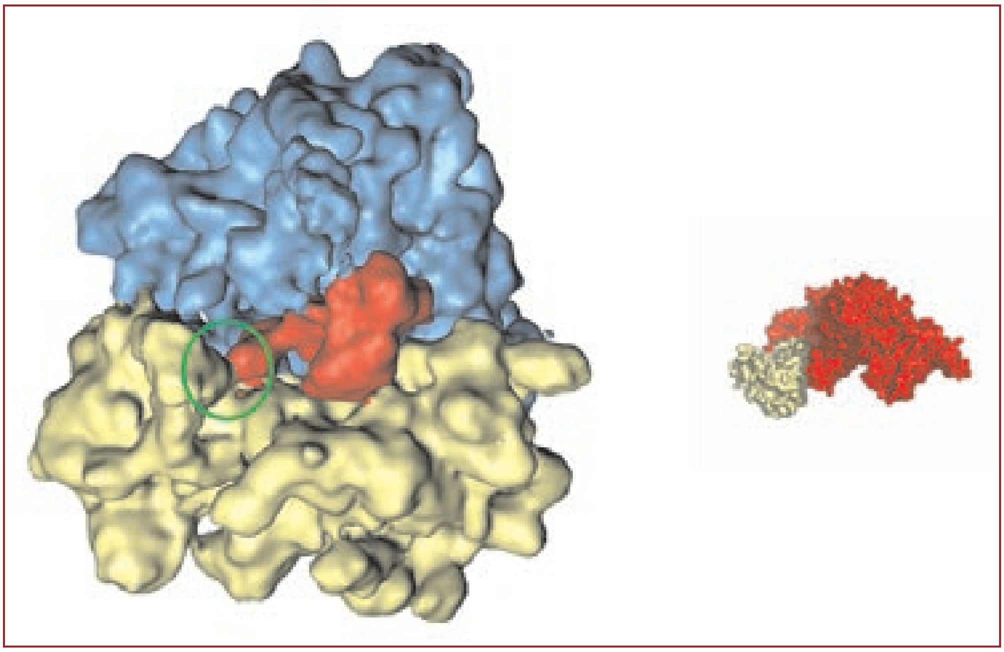

Fig. 2: Comparison of structures of (left) the ribosome (yellow and blue colouring for small and large ribosomal subunit, respectively) with bound eEF2 (red) [4]. Green circle shows the part of the ribosome which is mimicked by the toxin. (Right) toxin (yellow) bound to eEF2 (red).

References:

[1] R. Jørgensen et al., Nature Struct. Biol. ***10,*** *379-285 (2003).*

[2] R. Jørgensen et al., J. Biol. Chem. ***279,*** *45919-45925 (2004).*

[3] R. Jørgensen et al., Nature ***436,*** *979-984 (2005).*

[4] C.M. Spahn et al., EMBO J ***23(5),*** *1008-1019 (2004).*

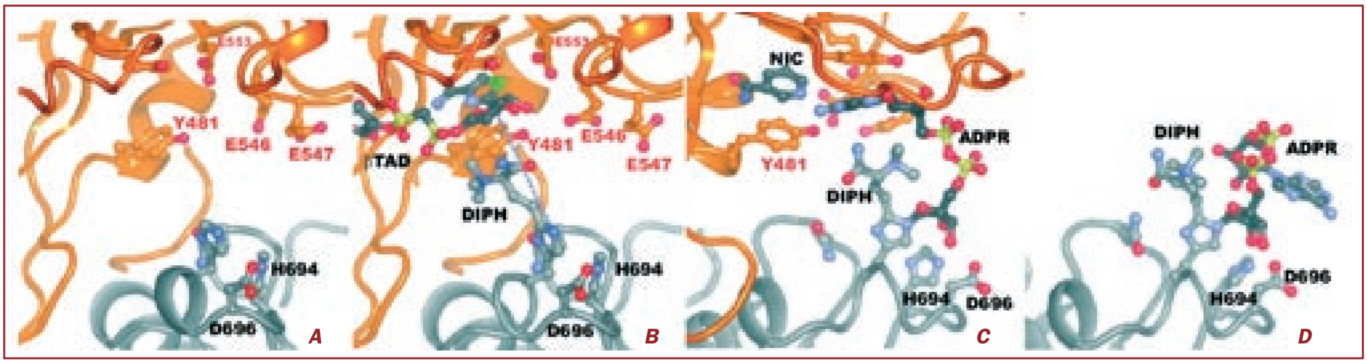

Fig. 3:
A) Close up of the modified region of eEF2 before and after the reaction catalysed by the toxin. The structure of the toxin (orange) without NAD$^+$ analogue bound to eEF2 (grey) showing the important amino acid residues marked in red and black for toxin and eEF2, respectively. B) Structure of the toxin with the NAD$^+$ analogue βTAD (shown with dark grey carbon atoms) bound to eEF2. This structure captures the molecules just before the reaction takes place. The amino acid on eEF2 which is modified by the toxin carries a unique modification called diphthamide (DIPH). The dotted blue line is drawn between the two atoms that will form a covalent bond during the reaction. C) Structure of the toxin bound to eEF2 after the reaction has taken place and the ADP-ribosyl group (ADPR) has been transferred to eEF2 from the NAD$^+$ leaving a nicotinamide (NIC) bound to the toxin. D) Structure of ADP-ribosylated eEF2 after dissociation of the toxin.

A number of protein factors aid the ribosome in the decoding/synthesis process. One of these factors is the eukaryotic elongation factor 2 (eEF2). This factor binds to the ribosome and facilitates movement of the messenger RNA on the ribosome by one coding unit in order for the ribosome to decode the next coding unit (Fig. 2). The pseudomonas exotoxin A (ETA) and diphtheria toxin both inactivate eEF2 by transferring the ADP-ribosyl group from NAD$^+$ (nicotinamide adenine dinucleotide) to a specific part of eEF2. By inactivating the eEF2 in the cell, protein synthesis is eventually stopped because a crucial step in the process is blocked and this results in cell death.

We used the method of X-ray crystallography to study how ETA binds and modifies eEF2. This method uses the high-brilliance X-rays produced by the BL1 beam line of BESSY to reveal the 3-dimensional structure of the molecules in atomic detail. This level of detail is necessary in order to understand the specific molecular interactions and chemical mechanism underlying the 'death touch' of the toxin. Previously, we obtained the structure of eEF2 with and without the toxic modification [1,2]. In the new study we obtained 4 different structures [3]. Firstly, the structure of the toxin without its co-substrate NAD$^+$ bound to eEF2. Secondly and thirdly, the toxin with a NAD$^+$-analogue bound to eEF2 in two states before and after transfer of the ADP-ribosyl group from NAD$^+$ to eEF2 and finally, a structure of the toxin bound to eEF2 together with a new potential drug against the toxin (Fig. 3).

The new structures reveal how the toxin recognizes and binds its target (eEF2) in the cell. Surprisingly, it was shown that the toxin disguises itself as the ribosome. It does this by mimicking a very important part of the ribosome, which is preserved in all organisms (Fig. 2). This ribosomal part is involved in 'proofreading' during protein synthesis which ensures that the protein produced does not contain errors. Through this mimicry, it ensures that the target cell will not be able to avoid binding of the toxin. Preventing toxin binding would require changes in a part of the ribosome or in eEF2 which has not changed during millions of years of evolution. This makes the disguise of the toxins perfect and the cell defenceless.

An understanding of the molecular details of toxin binding and the mechanism underlying the chemical reaction catalysed by the toxin is important as this mechanism is expected to be similar for the rest of the toxins in the family. This knowledge can be important for the development of new antibiotics against bacteria carrying these toxins including multi-resistant bacteria such as the pseudomonas bacteria involved in e.g. pneumonia and urinary tract infections. The work presented here included a structure of a new potential drug bound to the toxin giving hope for the future treatment of diseases caused by this class of bacteria.

Contacts:
Gregers R. Andersen
gra@mb.au.dk
A. Rod Merrill
rmerrill@uoguelph.ca

Physikalisch-Technische Bundesanstalt, Berlin

Watching the sun – radiometric calibration of space instruments

A. Gottwald, U. Kroth, W. Paustian, R. Thornagel, M. Richter

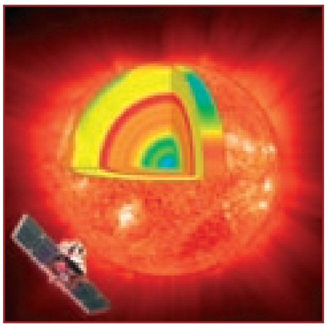

(Source: ESA/NASA)

The sun is the most important source of energy for life on earth. Each day, the sun's radiation gives light and warmth. However, the solar irradiation to earth is not constant, and any change can affect the life conditions on our planet. Explosive eruptions and solar storms cause intense auroral activity, disruptions in radio transmissions, or even damage satellites, telephone and power lines. Monitoring the sun's intensity collects important data for modelling physical processes in the sun's atmosphere, but also for earth climate models. To obtain data without atmospheric disturbances, space-based instruments are used, in particular for the vacuum-ultraviolet (VUV) spectral range which can not be accessed from ground. Over the last decades, the Physikalisch-Technische Bundesanstalt (PTB) has developed possibilities to offer absolute radiometric calibrations of spectrometers and detector systems in the VUV using the broad spectral characteristics of synchrotron radiation. This resulted in numerous co-operations with different partners, and contributions to several extraterrestrial, astronomical, and particularly solar missions (Table), which represent the most reliable radiometric standards in space to date [1].

Absolute measurements are based on the tracability to primary standards. In the context here, absolute calibrations are realized using two different primary standards: electron storage rings as primary radiation source standards [2] and cryogenic electrical substitution radiometers as primary detector standards [3]. The use of an electron-storage ring as a primary standard is based on Schwinger's equation, which is derived from classical electrodynamics and expresses the spectral radiant intensity of synchrotron radiation emitted from a charged particle in a dipole magnetic field. Hence, the radiant power of synchrotron radiation through an aperture can be calculated when measuring the corresponding storage ring parameters and geometric quantities. The technique allows to directly calibrate energy-dispersive detection systems, e. g. spectrometers. However, VUV spectrometers for spacecraft use often require dedicated cleanroom condi-

Instruments calibrated at the PTB laboratories at BESSY I and BESSY II for solar astronomy related space missions

Year of calibration	Wavelength range	Instrument	Mission
1994	50 to 160 nm	**SUMER** **S**olar **U**ltraviolet **M**easurements of **E**mitted **R**adiation	**SOHO** **S**olar and **H**eliospheric **O**bservatory (launched Dec 2, 1995)
1994	15 to 80 nm	**CDS** **C**oronal **D**iagnostic **S**pectrograph	
1996	15 to 80 nm	**SERTS** **S**olar **EUV** **R**ocket **T**elescope and **S**pectrograph (launched Nov 18, 1997 and June 24, 1999)	
1998	1 to 20 nm	**SORCE** **S**olar **R**adiation and **C**limate **E**xperiment	**TIMED** **T**hermospere **I**onosphere **M**esosphere **E**nergetics and **D**ynamics (launched Dec 7, 2001)
		SEE **S**olar **E**UV **E**xperiment	
2002	160 to 330 nm	**SOL-SPEC** **Sol**ar **Spec**tral Irradiance Measurement	**SOLAR** Solar Monitoring Observatory / ISS (in preparation)
2004	10 to 240 nm	**SOL-ACES** **Sol**ar **A**uto-**C**alibrating **E**UV/UV **S**pectrophotometers	
2004	115 to 135 nm	**TWINS** **T**wo **W**ide-Angle **I**maging **N**eutral-Atom **S**pectrometers (in preparation)	
2004	15 to 80 nm	**EIS** **E**UV **I**maging **S**pectrometer	**SOLAR-B** (in preparation)
2005	15 to 80 nm	**MOSES** **M**ulti-**O**rder **S**olar **E**UV **S**pectograph	(launched Feb. 8, 2006)
2005	1 to 240 nm	**LYRA** **Ly**man-alpha **Ra**diometer	**PROBA II** **Pro**ject for **O**n **B**oard **A**stronomy (in preparation)
		SWAP **S**un **W**atching using **AP**S detectors and image **p**rocessing	

References

[1] M. Richter et al., Advances in Space Research ***37****, 265 (2006)*

[2] R. Thornagel et al., Metrologia ***38****, 385 (2001)*

[3] A. Gottwald et al., Metrologia 43, S125 (2006)

[4] M. Richter et al., Metrologia ***40****, S107 (2003)*

[5] U. Schühle et al., Proc. SPIE ***5171****, 231 (2004)*

[6] A. Gottwald et al., Rev. Sci. Instr. ***76****, 023101 (2005)*

[7] R. Klein et al., Proc. of EPAC 2004, 2290 (2004)

Acknowledgements:

We thank all our co-workers and cooperation partners in this field, particulary from the Max-Planck-Institute for Solar System Research (MPS) and the Rutherford Appleton Lab (RAL).

tions or large vacuum tanks. In this case, measurements are performed at the respective laboratories of the cooperation partners using a secondary (transfer) source standard calibrated in the PTB laboratory.
To absolutely calibrate a source standard, it is directly compared to the storage ring with the help of a movable spectrometer that is alternately exposed to the radiation from both sources under analogous conditions. At BESSY II, this is a Normal-Incidence-Monochromator for the wavelength range from 40 nm to 400 nm. PTB's radiant intensity scales in the UV and VUV displayed in Fig. 1 are realized by deuterium lamps and hollow-cathode (HC) sources [1,4]. HC sources, in particular, have been used in the past for calibration of various instruments, most recently for the *Multi-Order Solar EUV Spectrograph* (MOSES) (Fig. 2). This instrument was successfully launched on February 8, 2006. The success of this mission is an important milestone towards use of this spectrometer type for the future Solar Orbiter mission, which is planned to be the successor to SOHO.

In some cases, it is more applicable to calibrate the spectral responsivity of a detector used within a spectrometer system. For the calibration of a detector, direct comparison with a cryogenic electrical substitution radiometer as primary detector standard is realized by turning both detectors alternately into a beam of monochromatized synchrotron radiation. Cryogenic radiometers are thermal detectors operated at liquid helium temperature which are based on the equivalence of radiant and electrical heating. In this way, PTB has established absolute spectral responsivity scales of semiconductor photodiodes using synchrotron radiation that cover the photon energy range from 3 eV to 60 keV [3]. Besides calibrations of standard semiconductor photodiodes for different missions, recently new types of solar-blind photodetectors based on wide band gap materials like diamond have been investigated within the framework of a scientific cooperation with the *Max Planck Institute for Solar System Resarch* [5]. These measurements were highly demanding, and profited from the outstanding capability of detector calibrations over the whole VUV spectral range. Moreover, to calibrate highly sensitive photon counting devices, a procedure to transfer the absolute spectral responsivity scale from the radiant power range around 1 μW to the sub-pW regime has been established [4]. The method, again, benefits from PTB's unique capability of operating the electron storage ring BESSY II as a primary source standard which requires the stored electron current being accurately adjusted and determined over a wide dynamic range of 12 orders of magnitude (from hundred milliamperes down to the current of a single electron stored) without affecting the spectral distribution.
As an example, Fig. 3 shows the measured quantum efficiency of two Lyman-α detectors, averaged over the detector area, which were developed at *Bonn University* for the NASA satellites TWINS.

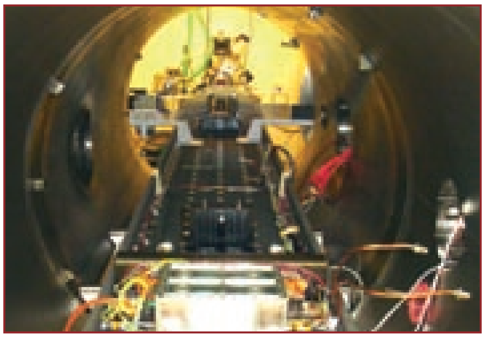
Fig. 2: The MOSES instrument during calibration at the RAL [1].

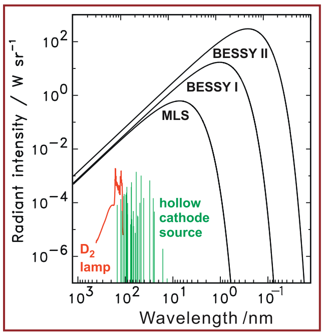

Fig. 1: Radiant intensity of electron storage rings BESSY I, BESSY II, and MLS in the storage ring plane into a bandpass of 1 % of the wavelength at an electron current I = 1 mA, and electron energies of MLS: W = 400 MeV, BESSY I: W = 800 MeV, BESSY II: W = 1.7 GeV; deuterium lamp into a bandpass of 1 % of the wavelength; hollow-cathode spectral line source operated with different rare gases [1, 4].

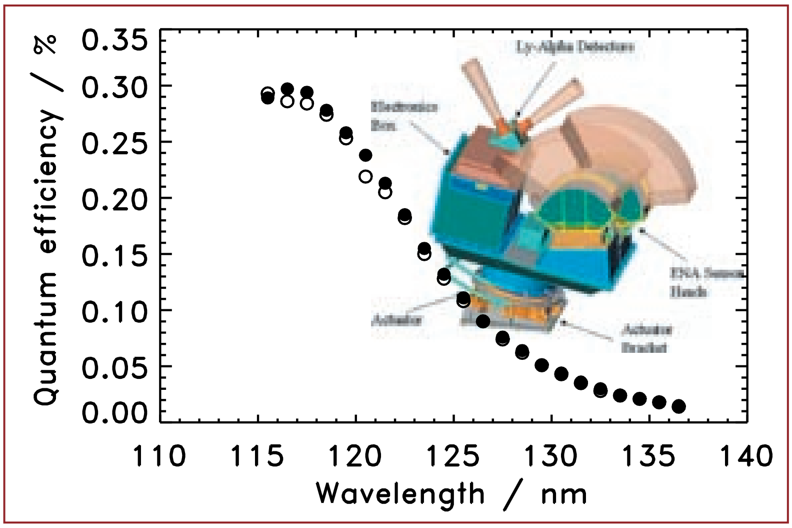

Fig. 3: Quantum efficiency, averaged over the detector area, of two Lyman-α detectors for the NASA satellites TWINS (Source: UC/LANL) [1,4].

In the near future, PTB's new Metrology Light Source (MLS) will offer extended capabilities for space-research related activities [7]. Source calibrations down to a wavelength of 4 nm will be possible at a newly designed monochromator. Furthermore, an electron-cyclotron resonance plasma source has been proven recently to be a versatile transfer radiation source standard [6], offering enhanced spectral capabilities compared to the hollow cathode. At the MLS, the availability of VUV undulator radiation enlarges the dynamic range for the available radiant power, and, moreover, opens new possibilities for polarization-dependent measurements.
At BESSY II, numerous space-related activities in the X-ray range will remain and be continued.

Contact:
Alexander Gottwald
alexander.gottwald@ptb.de

News & Events

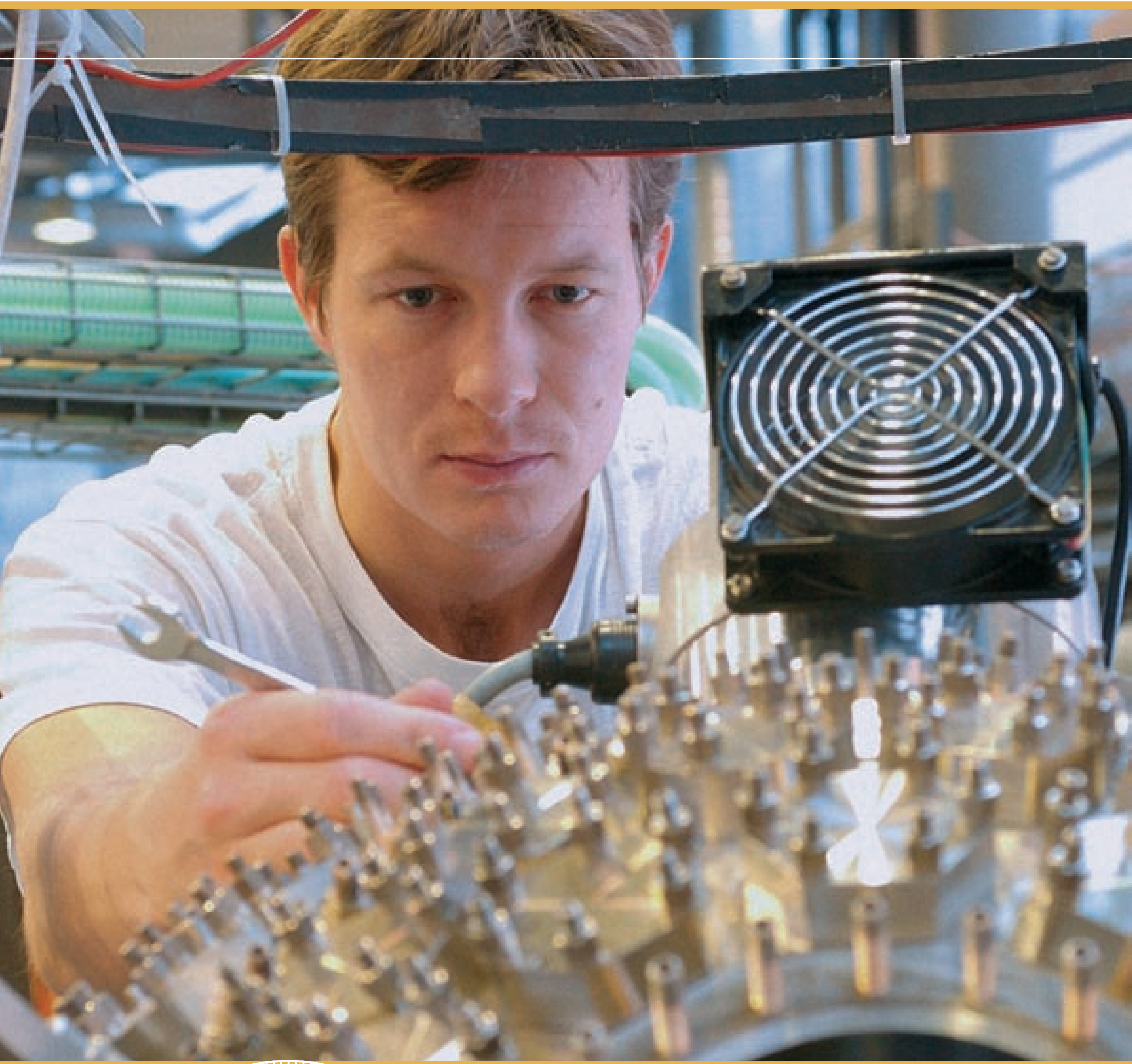

News

Nobel Prize laureates of different disciplines gave BESSY the honour of a visit during the Einstein year. After a tour through the facility there was ample time for discussions during the 'Academic lunch' together with colleagues from the campus Adlershof.

Nobel Prize laureates visit BESSY on the occasion of the Einstein year.

Among the numerous visitors were Czech vice-minister of Science and Education, Petr Kolár and the Indian secretary of Science and Technology, Prof. Ramamurthy.

Among the more than 3,200 visitors BESSY welcomed in 2005 were the Czech vice-minister of Science and Education, Petr Kolár, and the Indian secretary of Science and Technology, Prof. Ramamurthy. We are pleased that BESSY is such an interesting place to attract so many visitors every year.

In July, an international group of scientists evaluated the technical design of the planned Free Electron Laser for the German Science Council (Wissenschaftsrat). The test facility for the accelerating units of the FEL, the cavities, was visited. This test stand, called HoBiCat, is financed by an EU project and is part of the FEL collaboration with DESY. BESSY is awaiting the decision of the Science Council by the mid of 2006.

Well-known scientists evaluated the technical design of the BESSY FEL.

BESSY had the great opportunity to present the FEL project to Berlin politicians and interested public during an exhibition in the house of the Berlin Parliament. Organized by a local optics and photonics network, OpTecBB, the day was under the auspices of Walter Momper, the president of the Berlin parliament and former mayor of the city.

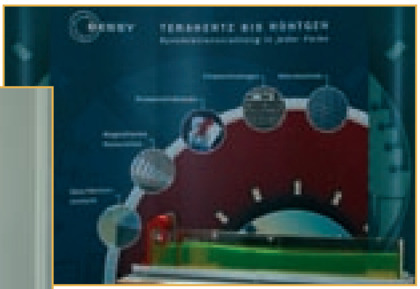

Presenting the BESSY FEL at the Berlin Parliament under the auspices of W. Momper, former mayor of the city.

In September, BESSY said farewell to William Peatman, vice head of the experimental division. He was nearly a man of the first hour at BESSY I and accompanied the building and setting-up of BESSY II. We are very grateful to his passionate and very successful work and wishes him all the best for the time of his retirement. Thankfully, he still helps out even so his 'new' life is already very busy. BESSY will also not forget the other long-term staff members who retired in 2005: Michael von Hartrott and Peter Rotter.

Farewell to William Peatman and remembering Leo and Clara Fichtman.

With the new-built campus all around BESSY one sometimes forgets the history of this site. We were therefore thankful that two 'Stolpersteine' were integrated in the pavement and inaugurated with a little ceremony reminding of two Jewish people, *Leo* and *Clara Fichtman,* who lived with their children in an allotment close to the banks of the canal. They were both deported and died in May 28, 1942 in concentration camp Sachsenhausen. May this help to remember that a Holocaust should never happen again.

Children and adults discovering the fun of science during 'Lange Nacht der Wissenschaften'.

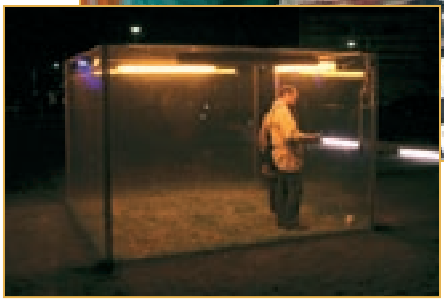

Events

2005 was announced the Einstein year: 100 years after his 'wonder year' the focus was on physics after Einstein's genius ideas. Many events took place within the framework of this year. BESSY was co-organizer of the 'Highlights of Physics' – an interactive exhibition in the Urania, including a contest for students and a big science show. The theme of this exhibition was 'Time – Space – Chance' and BESSY displayed the plans for the free electron laser, which will achieve a time resolution as short as femtoseconds.

Onboard the exhibition boat MS Einstein, BESSY was present with an exhibit on the photoelectric effect – the work winning Einstein the Nobel Prize for. The boat started in Bremen, calling in 37 stations along the Weser, Havel, Spree, Main, Neckar, Rhine and ended in Karlsruhe.

The Lange Nacht der Wissenschaften is already an institution at BESSY. The focus on Einstein was celebrated together with the Albert-Einstein-Oberschule. The pupils of this school enriched the programme with their Big Band and later on with school bands. They performed a self-written play called 'Dream on, Einstein' in which they expressed their thoughts on the relativity of time. Challenging for the audience was a science quiz with problems and astonishing experiments – nobody left the show as looser.

Projects with and for pupils played an enormous role in 2005. Accompanying the Lange Nacht a TV programme called 'nano' organized a 'nano camp' with pupils from all over Germany. They stayed for one week in Adlershof, visiting another institute each day. At BESSY they injected the electrons into the storage ring, grew protein crystals and analyzed them.

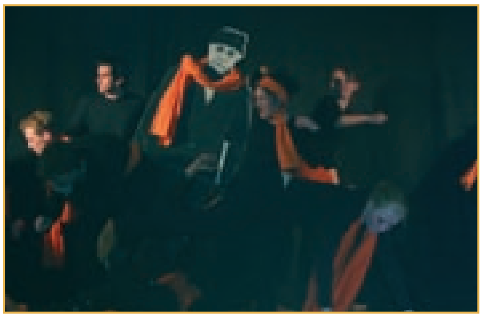

'Dream on EInstein' – a play on the relativity of time.

'Nano Campers' take over the control of the storage ring.

They gave their colleagues some puzzles to find out which metal they choose to draw. The young people were fascinated to get an insight of the 'real' life of scientists. Hopefully this camp will trigger the decision to become a scientist themselves. At the occasion of the 'Adlershofer Tage der Forschung' two school courses performed lithography experiments in the lab. Instead from BESSY the light came from an UV lamp, but the pupils could do every step of the process by themselves. In the end they held their own structured chip in hand.

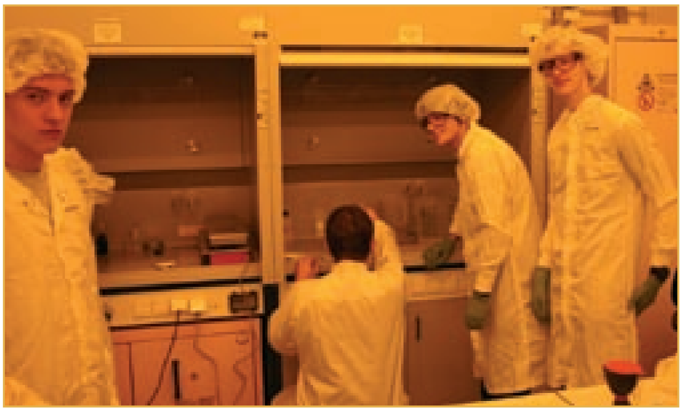

Pupils creating their own chips in lithography lab.

'Physik zum Frühstück', our interactive lecture around the subject light, gained so much attention this year that two of the three events were sold out. Next year one of the lectures will be part of the 'Land der Ideen' – a campaign accompanying the soccer world championship. We appreciated that more families with smaller children used the occasion to visit BESSY.

BESSY became a wanted location for TV and film productions, having the image of a kind of mysterious lab. Thanks to the understanding of our users the shooting was possible. It was an experience to see the light source BESSY in the light of cameras and spot lights.

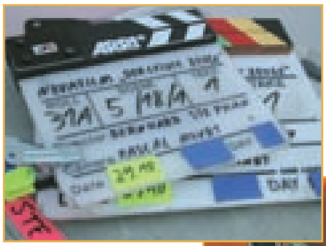

Apropos light: Light was also the subject of an art project which took place during the winter months. In the evening the foyer was immersed in projections of pattern giving an entirely new and fascinating atmosphere to the room.

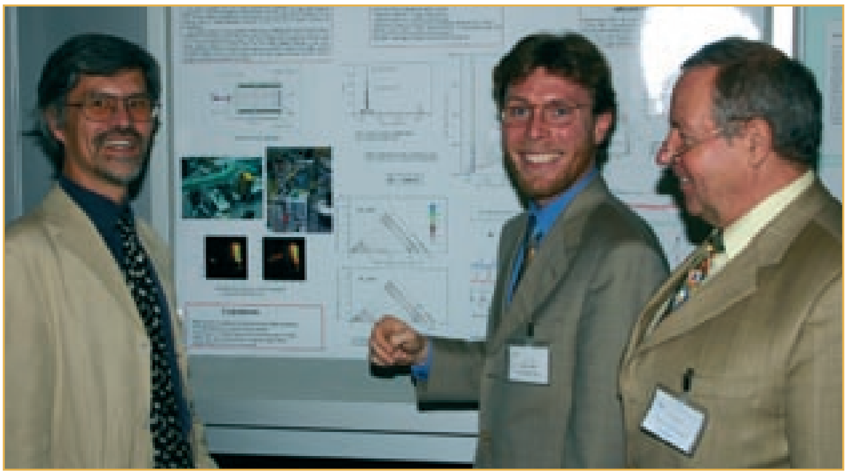

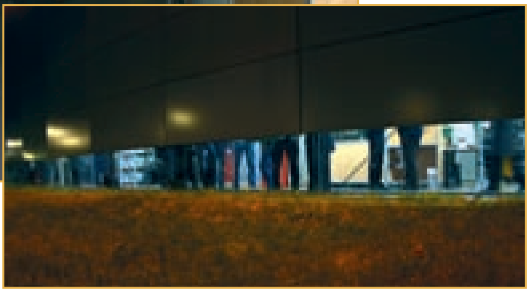

Users' Meeting 2005

This years' key note lecture by Philippe Sainctavit (CNRS/UPMC, France) is an exquisite example of the growing importance of EU science co-operations. In preparation for the new French synchrotron radiation source Soleil, Sainctavit and co-workers continued their work on molecular magnetism at BESSY, setting up a 4 Tesla cryostat which allows cooling down to 4K. At BESSY the bottom-top approach in nanotechnologies meets with the other way around. The goal of decreasing dimension sizes is approached either using molecules as the ultimate smallest building blocks as Sainctavit does or from lithography, trying to reduce the fabricated structures to the limits.

More than 300 participants joined in the discussions on the various talks covering highlight experiments carried out at BESSY. More than 170 posters, presented during the poster session in the experimental hall, gave an overview about the large field of research carried out at BESSY. Discussions were lively as always and followed by the 'Berliner Buffet', kindly sponsored by the vendors participating at the exhibition. More than 40 vendors displayed their products. As interest from exhibitors as well as visitors is still very high the exhibition is rather at its limits, initiating the search for maybe a new site.

For the first time Christian Jung, well-known to the user community, but newly appointed as vice head of the experimental division, gave the overview on new beamlines and instruments at BESSY. Peter Kuske followed with reporting on machine improvements. Uwe Hergenhahn gave a summary of the activities of the users' committee. Thanks to Wolfgang Kuch, Christian Herbert-Fischer and Uwe Hergenhahn; they finished their term in the committee. Birgit Kannengießer, Peter Baumgärtel and Ralph Püttner were elected for the next term. The valuable work they are doing is greatly acknowledged by users and management likewise. Details can be found on the Users' Page of this issue.

Workshops:

Workshop on ultrafast time-resolved instrumentation and experiments at synchrotron radiation facilities and free electron lasers	Zeuthen, April, 27 -29
International Workshop on Infrared Microscopy and Spectroscopy with Accelerator Based Sources	Rathen, June, 26 - 30
PRORA Satellite Workshop Aktuelle Fragen der Röntgenanalytik - Quo vadis XRF ?	November, 26 - 27
BESSY Users' Meeting	December, 1 - 2
Workshop on Scientific Possibilities with Ultrashort Soft X-ray Pulses	December, 2 - 3

Innovation Award on Synchrotron Radiation

Even so synchrotron radiation sources generate extremely bright X-rays, the focussing into very tiny spots remained a problem. ESRF scientists Peter Cloetens, Olivier Hignette and Christian Morawe brought a special focussing system to perfection which allows the generation of extremely small X-ray spots. For their work, the three physicists have been awarded the Innovations Award on Synchrotron Radiation by the Society of BESSY Friends and Sponsors.

P. Kirkpatrick und A.V. Baez already in 1948 had the idea to design a combination of two perpendicular oriented elliptical mirrors which focuses X-rays ideally on a spot. A big advantage of their design is that intensity losses are marginal. Their design is also predestined for spectroscopic applications, since all X-ray frequencies are focussed on the same spot. The awarded scientists optimised mirrors and adjustments. As a special trick they coated mirrors with numerous extremely thin metal layers in order to boost the reflectivity and they bended the resulting mirrors exactly as required. With this ingenious design they recently achieved a world record beam width of 40 nm (which is roughly the size of a single Influenza virus).

The Innovation Award on Synchrotron Radiation, announced Europe-wide, is awarded annually by the Society of BESSY Friends and Sponsors for an outstanding technical achievement or experimental method that promises to extend the frontiers of research with synchrotron radiation.

Peter Cloetens, Olivier Hignette and Christian Morawe won the Innovation Award for their X-ray focussing system.

Ernst-Eckhard-Koch-Prize

In 1927 Niels Bohr worded the complementary principle: Every part of nature has wave or particle character, but only one appears at the same time. It depends on the experiment, which character is measured. In the last years the validity of the principle was doubted for photons as well as atoms or other compound systems. Daniel Rolles showed in his PhD thesis also the ambivalence in the nature of electrons. He was given this years' Ernst-Eckhard-Koch-Prize for his dissertation. His work is based on the classical double-slit experiment by Young. Electrons passing a double slit form an interference pattern, clearly indicating their wave character. The double slit in Rolles work is a nitrogen molecule emitting the electrons from an inner shell after X-Ray absorption. This experiment resulted in the interference pattern typical for waves. The coherence is partly destroyed when one of the nitrogen atoms is replaced by a different isotope. In the picture of the double slit this means that one path is partly marked. The measured angular distribution of the emitted electrons indicates the cross-over to an incoherent particle-like system, i.e. the electrons behave like particles and waves at the same time.

The Ernst-Eckhard-Koch-Prize is awarded annually by the Society of BESSY Friends and Sponsors for an outstanding dissertation in the field of synchrotron radiation. The PhD thesis should be carried out at BESSY or HASYLAB (Hamburg) as the main work-places of E.-E. Koch.

Daniel Rolles, winner of the Ernst-Eckhard-Koch-Prize 2005, showed the ambivalence of electrons in a double-slit experiment.

Tailoring radiation with wiggles, gaps, and shifts: The art of undulators

In the first synchrotron radiation sources the radiation was generated exclusively in bending magnets – simple dipole magnets which change the direction of the electron beam. Changing any of the properties of the emitted radiation was very difficult. The more researchers used synchrotron radiation the more they demanded special radiation properties such as higher energy to cover hard X-rays, higher brilliance to get more photons or qualities like coherence and polarization. During the years machine physicists started to insert magnetic devices (insertion devices, IDs) into the straight sections of storage rings to tailor the light emission according to the scientific needs. Today, third generation synchrotron radiation sources like BESSY are optimized for operating in particular with insertion devices.

Insertion devices are periodic magnetic structures with magnet period between a few centimeters and one meter – wigglers, wavelength shifters and undulators. Wigglers are high field devices that enhance the photon flux by ‘lots of magnetic field’. Wavelength shifters use a single high magnetic field pole, usually realized by superconducting coils, to generate hard radiation of tens of keV photon energy from ‘low energy’ storage rings.

Undulators have a large number of periods (up to 100) and the radiation characteristics are dominated by interference effects. The brilliance, the number of photons emitted per time from an effective source area into a solid angle within a given bandwidth, is enhanced by several orders of magnitudes as compared to the emission from storage ring bending magnet. Simultaneously the heat load on the optical components is minimized.

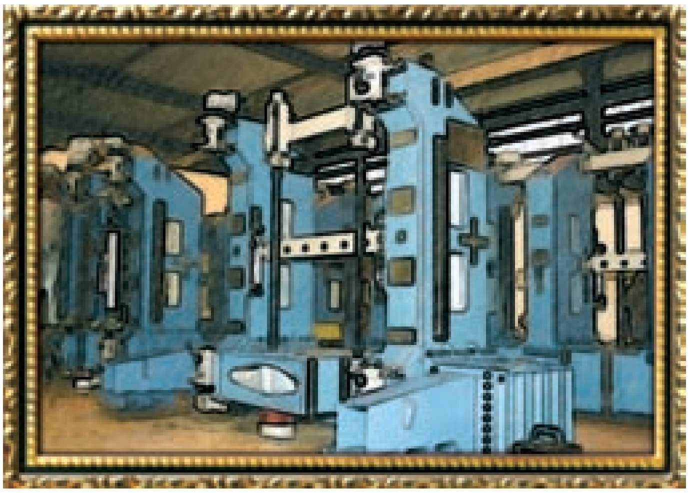

Undulators are special, since they must be operated 'on-resonance' (see Box 1). Therefore the magnetic field configuration of undulators must essentially be perfect for trouble free simultaneous operation of several devices. For example, the integrated field within the physical aperture of a BESSY undulator should remain below 0.01 Tesla · mm. To put these number into perspective we note that the integral over half a period reaches values of the order of 10 Tesla · mm and the (constant) contribution from the earth magnetic field is 0.1 Tesla · mm. A different but as important specification is the requirement for an essentially perfectly periodic field to ensure constructive interference between all poles (see Box 2). In this contribution we describe how we achieve the required accuracies with our undulators.

Box 1: Resonance condition

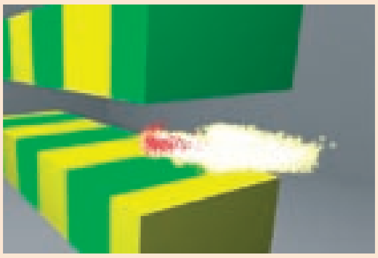

The relativistic electrons travel through the undulator field along a sinusoidal line with an amplitude of a few microns. The longitudinal velocity is below the speed of light both because of the finite mass of the particle and because of the transverse excursions due to the magnetic field. On resonance when the maximum emission occurs the light traveling along the undulator axis overtakes the particles by one optical period (a few nm) while the particle and the light travel through one period of the undulator (a few tens of mm). Thus the phase of the optical field at the position of the particle increases by 2π per undulator period. For relativistic velocities this leads to the relation

$$\lambda_1 = \lambda_0 /(2\gamma^2) (1+1/2 K^2).$$

Here, λ_1 is the wavelength of the first harmonic of the undulator spectrum, λ_0 is the period of the magnetic field, γ is the particles’ kinetic energy in units of the rest mass, and K is a dimensionless constant of the order of 1 which is proportional to the magnetic field amplitude.

Fig. 1:
High precision test stand for single magnet block characterization. By moving a magnetic block with respect to a stretched out wire (mimicking the electron beam) the induced voltage is representative for the integrated magnetic field.

Magnets

All BESSY undulators use permanent magnets based on the rare earth alloys $Nd_2Fe_{14}B$. This magnetic materials exhibit a magnetization of typically 1.2 Tesla corresponding to a surface current density of 1,300 A/mm. The high coercive force of these permanent magnet materials and a permeability close to 1 allow for magnetic arrangements such as the APPLE design (see Box 3) to generate any desired polarization (see Box 4).

There is presently no alternative to the use of permanent magnets: Normal conducting electromagnets not even get close to the current density of permanent magnets due to cooling limitations, while superconducting technology reaches even higher magnetic performance. However, so far there is no mature technology to reproducibly tune the magnetic field.

Permanent magnet undulators exist in two different designs: In pure permanent magnet undulators (PPM) the field is only generated from blocks of permanent magnet. The principle of linear superposition of fields allows for accurate prediction of the field. All elliptically polarized undulators of the UE type at BESSY employ this design. In so-called hybrid undulators high permeability pole pieces made from permendur (an alloy of composition $Fe_{49}Co_{49}V_2$) channel the magnetic flux towards the midplane. The high homogeneity of the permendur material suppresses field errors. The magnetic performance is increased by shaping the poles and the magnets as wedges as is done in the linearly polarized U49 and U41 undulators.

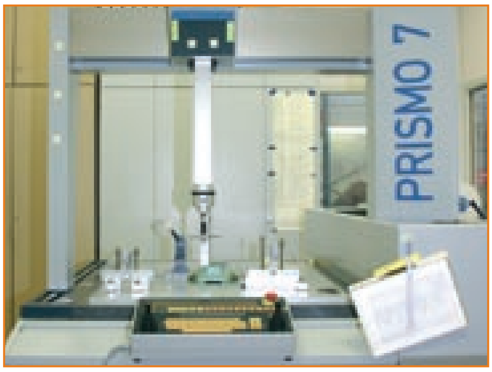

Fig. 2:
Using a 3D coordinate measuring machine (PRISMO 7, Zeiss) mechanical tolerances in the range of a few microns are determined. The BESSY system additionally allows for a geometric correlation of part size and magnetic field.

Permanent magnet blocks typically have a scatter of the magnetization of the order of 1% and a scatter of the direction of the magnetization of 1°. To cope with these large values, we characterize each of the ca. 1,000 magnetic blocks of an undulator upon delivery.

This geometrical and magnetical characterization is achieved in our high precision test stands (Figs. 1 and 2). The obtained data are used to assign each block to a unique position within the magnetic arrays of an undulator using a technique known as simulated annealing.

Construction and assembly

To assure the constructive interference the gap must be the same within 20 µm all along the undulator. In order to allow the use of the 5th harmonic the reproducibility of gap and shift setting must be in the order of 3 µm. The gap and shift motion have to be realized in the presence of strong and variable magnetic forces reaching tons per meter undulator length.

We achieve these specifications using an as stiff as possible support built around a cast iron structure designed by a bionic optimization procedure (Fig. 3). The magnets are held in precision mounts bolted to the aluminum beams. The actual gaps and shifts are measured using optical encoders. High dynamical servo motors provide the motive force.
All parts are designed in-house and BESSY fabrication drawings are used to contract the production to industry.

All undulators are assembled and commissioned at BESSY (Fig. 4). After assembly of an APPLE type undulator the typical remaining phase jitter is less than 3.5° i.e. the resonance condition is met from pole to pole within less than 1%. Furthermore, there is close agreement between the trajectories and multipoles from magnetic measurements of the assembled undulator and those from previous magnetic measurements of the individual blocks Fig. 5. This unique result is caused by the high precision techniques developed at BESSY which are applied throughout in manufacturing process

At such a small phase jitter the brilliance is limited either by diffraction effects leading to transversely coherent beams, or by the finite emittance and energy spread of the electron beam. Thus there is no need to further improve the magnetic field quality of BESSY undulators in this respect.

Shimming

There remain magnetic errors that cause trajectory wandering beyond a few micrometer and extra focusing effects. They are compensated using shims. Shims are small pieces of permanent magnets or ferromagnetic material strategically placed within the undulator (Fig. 6). The effect of permanent magnet shims depends on the size and positions, while the effect of ferromagnetic shims also depends on the magnetic field at the shim position. The latter effect is used in BESSY APPLE undulators to compensate shift dependent effects. Shims are also used to compensate dynamic multipoles due to the naturally occurring and omnipresent edge focusing.

In fact, undulators consist of 'nothing but edges'. On top of the natural focusing there is beam distortion due to magnetic field imperfections. The focusing varies according to the operational status of the undulator. It is localized in the storage ring at the position of the undulator. This modifies the electron beam cross section all around the storage ring unless compensated by slightly different powering of adjacent magnetic focusing elements of the storage ring as done at BESSY.

The dynamic apertures as measured by kicking the electron beam with different amplitudes show the expected increase of the dynamic aperture due to shimming (see Facility Report of this issue). A further increase of the dynamic aperture for all undulators will improve the lifetime of the stored beam. It also will increase the injection efficiency with operating undulators as needed for topping-up operation of the BESSY storage ring.

A coming challenge will be the installation of the elliptically polarized undulator UE112 in spring 2006. Due to the long period of 112 mm the interaction with the stored beam will be much bigger than at any other undulator. To predict the required shims for sufficient dynamic aperture we use fast analytic and simplectic (i.e. phase space conserving) particle tracking tools which have been developed at BESSY based on generating functions (see Box 5).

Box 2: Undulator Spectra

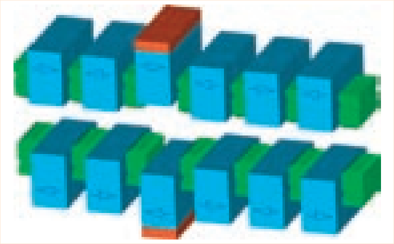

The spectrum of a planar undulator, i.e. when the electrons execute an oscillation within one plane consists of several odd harmonics. Even harmonics are emitted off-axis. Due to finite electron beam divergence and finite beamline acceptance even harmonics also appear in the spectra.

The experimental spectra are complicated by higher order contribution of the grating monochromator. In the quasi-periodic undulator U125-2 (see sketch) some poles are weakened which shifts the higher harmonic emission to those parts in the spectrum where the grating monochromator has low transmission.

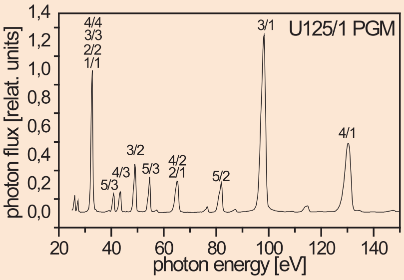

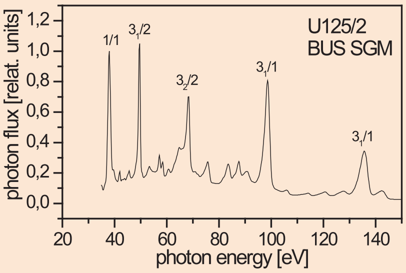

The top spectrum has been measured at U125-2 PGM for g = 61.181 mm directly behind the exit slit of the monochromator. Some spectral features are identified by two numbers, the first one referring to the undulator harmonic, the second one to the monochromator order. The transmission function of a grating monochromator tuned to the first harmonic is sketched by shadowing. Note the 1st harmonic in 1st order is contaminated by 2nd harmonic in 2nd order, 3rd harmonic in 3rd order etc. in a manner which is difficult to control. The bottom spectrum of U125-2 SGM was measured at the BUS beamline. Note the minimum intensity at position of the higher orders of the monochromator transmission.

The spectrum of a circular undulator, i.e when the electrons move along a screw type trajectory with the pitch of the undulator period, consists on-axis only of the first harmonic. Higher harmonics appear for elliptical polarization and/or off-axis.

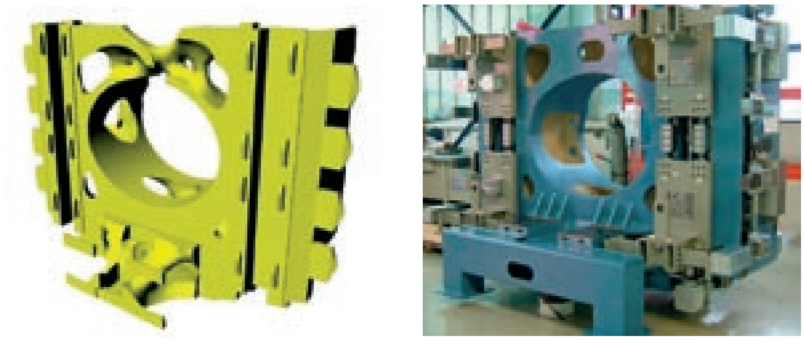

Fig. 3:
Support frame for UE112. The shape of the cast iron part is designed using a bionic optimization procedure.

Fig. 4:
Assembling an APPLE Undulator

Undulator control

All components of installed undulators are under control of a generic computer code that is matched to the control system of the BESSY storage ring. This guarantees that at each of the eleven undulators, users have complete control over photon energy (gap) and polarization (shift) independent of users at other beamlines. This is made possible by the precision design and construction leading to a high quality magnetic field, by feed-forward corrections of the remaining and of the naturally occurring gap and shift dependent kicks and focusing, and a slow (6 sec) feed-back correction of the electron beam position. The focusing feed-forward mechanism reduces any variation of the electron beam cross section due to beta beat to an acceptable level.

Free Electron Laser

To meet the requirements of undulators for the BESSY soft X-ray Free Electron Laser, we modified the mechanical design so that it allowed for simplification of the assembly groups and reduction of the height from presently almost 3 m to 2.45 m. The first undulator in the new design is UE112 (Fig. 3). The control system will allow for simultaneous and synchronized operation of several undulators.

We also provide undulators for the high gain harmonic generation (HGHG) FEL test facility at MAX Lab, Sweden. In parallel, we improve magnet quality in a joint project with Vakuum Schmelze (a leading manufacturer of rare earth permanent magnets) and DESY.

Box 3: APPLE undulator

The APPLE (= Advanced Planar Polarised Light Emitter) type undulator consists of four identical rows of permanent magnet, two of them above and two of them below the storage ring plane [1]. The field of each row at the electron beam axis is periodic with identical periods and is oriented near 45° with respect to the storage ring plane. Amplitude and direction ot the total field depend on the gap. By longitudinally shifting the rows with respect to each other field configurations can be generated that make the particles travelling along a screw like trajectory emitting circularly polarised radiation or oscillating in an inclined plane emitting light linearly polarised at any direction. In the APPLE III design, the orientation of the block magnetization at 45° enhances the magnetic performance by a factor of 1.4 [2].

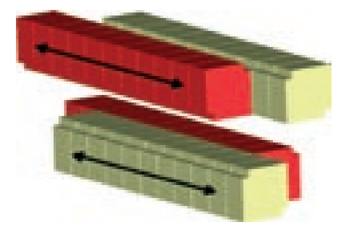

Principle of an APPLE undulator

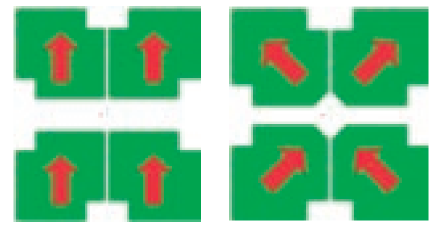

Magnetization orientation.
Left: APPLE II, right: APPLE III

In the BESSY double undulator the rate of switching the polarization is dramatically enhanced: Two undulators one after the others are set to different helicities/polarizations. A magnetic chicane makes the electron beam going at different angles (± 200 µrad) through the undulators and thus the two light beams (of different polarization) separate further downstream in the beamline. A fast mechanical chopper cuts off one of the light beams and transmits one polarization at a time to the experiment. This switching rate can exceed 100 Hz.

References:
[1] S. Sasaki, Nucl. Instr. Meth. ***A347****, 83-86 (1994).*
[2] J. Bahrdt et al., AIP-Proceedings ***Vol. 705*** *of the SRI 2003.*

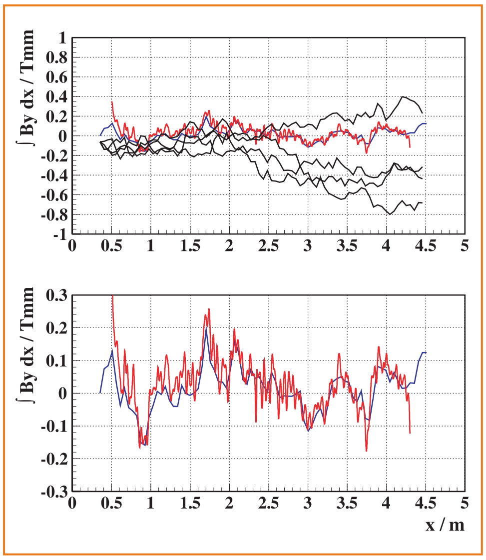

Fig. 5:
First magnetic integral (proportional to trajectories) predicted due to magnetic and geometric single block measurements and due to magnetic measurements of the completely assembled structure. Some simulated trajectories due to a random assembly are also shown. The improvement due to the simulated annealing sorting procedure is a factor 10 with respect to the residual kick.

Resume

The in-house fabrication of insertion devices has allowed BESSY to be on the cutting edge of APPLE undulator development.

This includes

- the consistent prediction of undulator fields based on single block characterization and the high precision assembly,
- the 180 degree rotation of the plane of linearly polarised light in APPLE undulators,
- the reduction of the contamination by higher order radiation using quasi periodic undulators,
- the enhancement of magnetic performance of planar undulators using the wedge pole concept,
- the development of particle tracking techniques to assist the design and operation of insertion devices,
- and the successful operation of several independently functioning insertion devices in a low energy storage ring.

We work hard to keep BESSY's leading position in undulator development also in the future.

Box 5: Software tools

We have developed a simplectic tracking code which allows for the analytic description of the ID/ring interaction based on generating functions.

More information:
godehard.wuestefeld@bessy.de

WAVE is large package of routines to calculate the emission of electrons moving in a general magnetic field configuration. It has been used for radiometry work at the BESSY PTB wavelength shifter, for instance.

More information: michael.scheer@bessy.de

PHASE propagates an optical field through a system of components including diffraction effects. The programme is used to design and to verify designs of beamlines and monochromators, including those proposed for the BESSY soft X-ray Free Electron Laser Facility.

More information: johannes.bahrdt@bessy.de

Box 4: Polarisation measurements

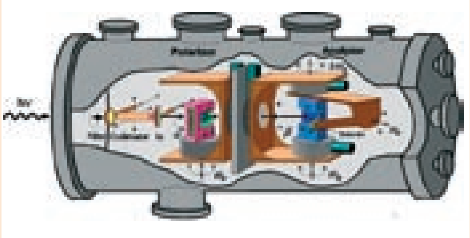

The polarization of our undulators has been characterized using the BESSY polarimeter. This instrument is equipped with different transmission multilayers as phase shifters and corresponding reflection multilayers operating near the Brewster angle as analyzer. It is found that the BESSY undulator radiation is completely polarized. The polarization is distributed among linear and circular polarization depending on the shift value as predicted by magnetic field calculations. The on-axis intensity of the third harmonic varies with polarization and vanishes for complete circular polarization in accordance with prediction.

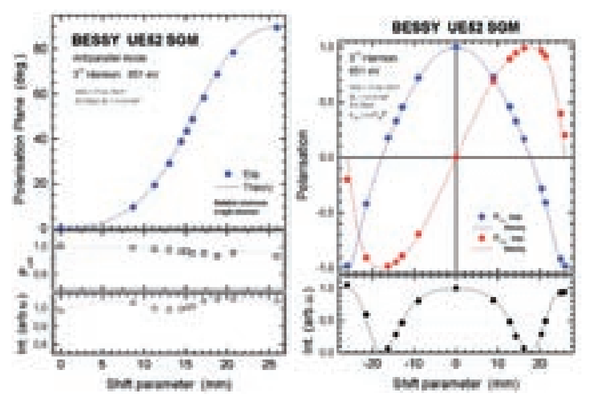

Polarization measurement of UE52 undulator using the BESSY polarimeter equipped with transmission and reflection multilayers of different composition. Note the intensity variation with shift in case of the 3rd harmonic

Fig. 6:
Precision bench for local field measurements and shimming

Contact:
Johannes Bahrdt
johannes.bahrdt@bessy.de

Facility Report

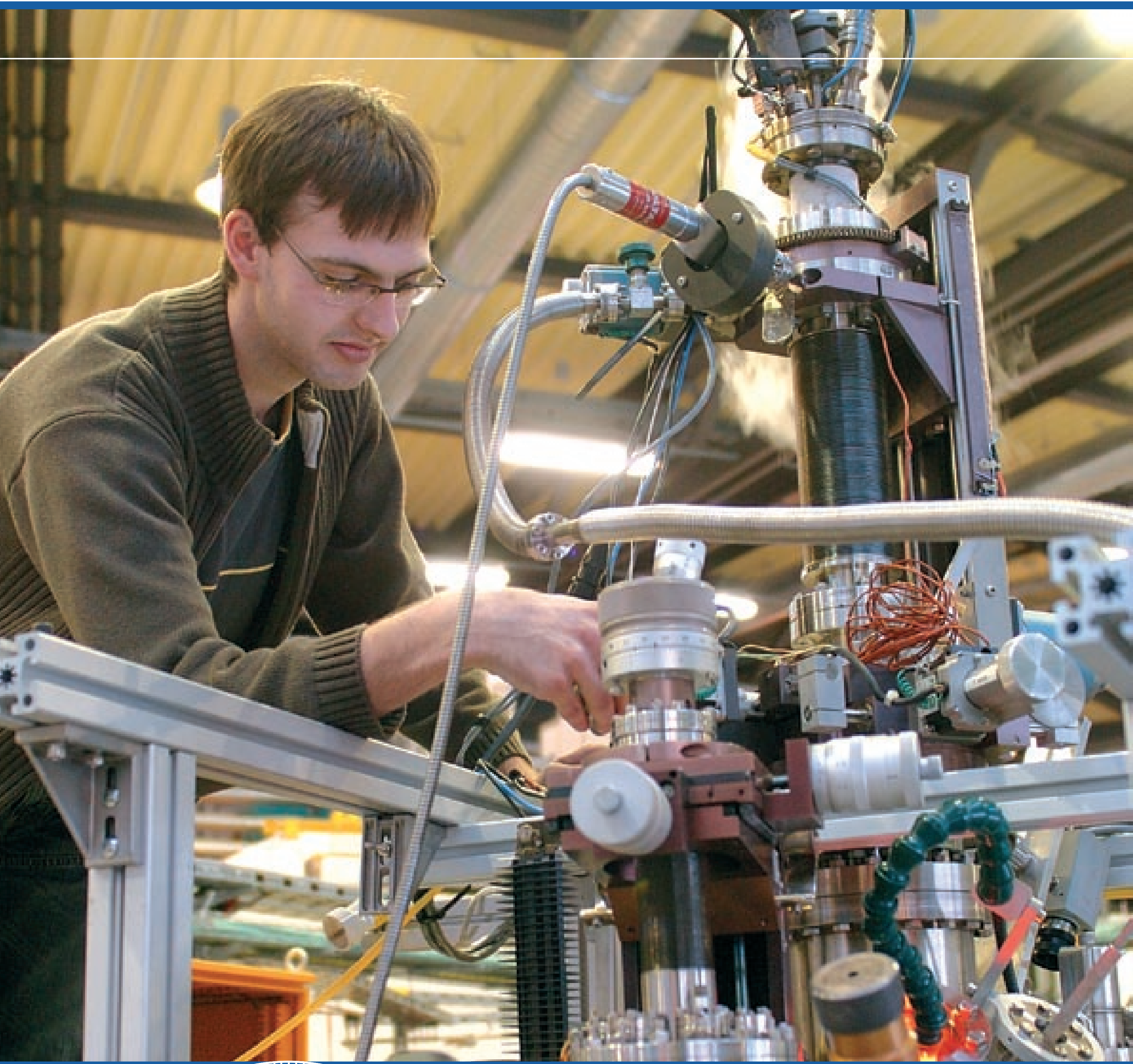

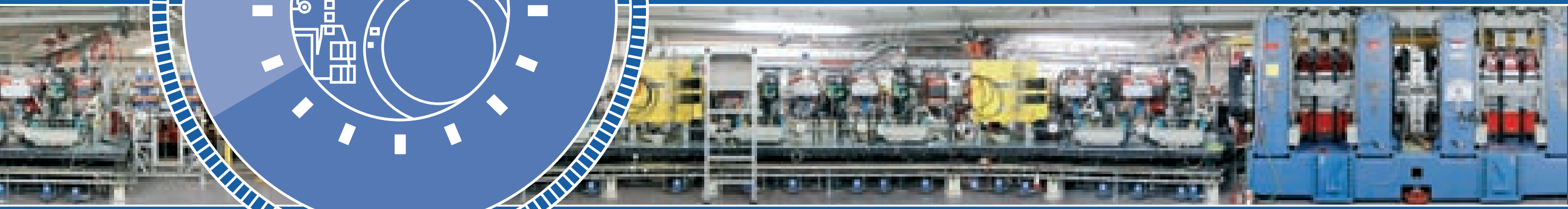

Machine Status

In 2005 the BESSY source delivered light to users during 5,252 h spread over 38 weeks. Among these were 4 weeks of operation in single bunch and 1 week operation in the low-alpha mode with bunches as short as 2 ps FWHM. In addition, 7 weeks were dedicated to machine development and beamline commissioning in order to improve the overall performance of the light source.

Some of the characteristics of the light source are compiled in the table. Noteworthy is the improved lifetime of the stored beam. At the beginning of last year the lifetime still suffered from the operation of the 7T wiggler. Warming up of its cold vacuum chamber and pumping off the frozen gas released from the surfaces, eventually restored and improved the lifetime. We now inject regularly three times a day in 8 h intervals. The number of daily injections increases to five in case of single bunch mode operation.

The standard operation is hybrid mode, with 250 mA stored in 350 buckets and 5 to 10 mA injected into a single bucket in the remaining empty gap of 100 ns. This single bunch is used primarily for producing short pulses of radiation by slicing the beam with an fs-laser during normal user operation. The high reliability of >96% achieved last year reflects the success of the continuous efforts of the staff to improve and keep up all parts of the facility.

Undulator re-shimming

Some insertion devices can severely reduce the horizontal acceptance of the ring resulting in a strong impact on the capture efficiency for injected particles. The non-linear beam dynamics introduced by these IDs was studied with experimental frequency map analysis. We found that in some cases insufficient shimming of the undulator field is responsible for the poor performance, for example in the early APPLE-type UE56-2 and the strong undulator U125-2. Re-shimming of those undulators was performed either on the fly or in the lab during shut-down periods. The promising results can be seen in Fig. 1.

Improvements were also obtained in cases in which field imperfections led to aperture limitations. During the shut-down we brought both parts of the UE56-2 to the measuring bench and re-shimmed it carefully in a two week period. The results in terms of the integrated normal and skew fields and the improvements of the horizontal dynamic aperture are shown in Fig. 2. Today, UE56-2 reduces the lifetime by only 5 % whereas before the impact was 6 times larger. The injection efficiency improved similarly.

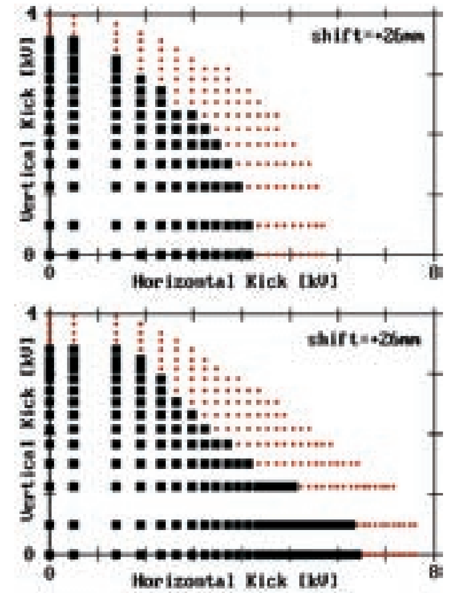

Fig. 1:
'Survival plots' of the beam being kicked in both spatial directions with increasing strength. Measurements without noticeable beam loss are represented as black dots and small red dots represent cases with more than 2 % particle losses. These two pictures clearly show the impact of the UE52 on the horizontal acceptance: top – before and bottom – after the in situ re-shimming. The horizontal dynamic aperture is increased almost without reducing the vertical aperture. In the above case the ID was set for vertical polarization at the smallest gap.

BESSY, the Light Source

horzontal emittance	6 · 10^{-9} m·rad
beam energy	1.72 GeV
beam current	> 250 mA, multi bunch mode
	> 20 mA, single bunch mode
beam lifetime	> 8 h at 250 mA, multibunch mode
	~ 2.5 h at 20 mA, single bunch mode
16 straight sections	12 undulators (5 elliptical)
	4 superconducting insertion devices
pulse duration (FWHM)	30 ps (natural), ≥2 ps (low alpha mode)

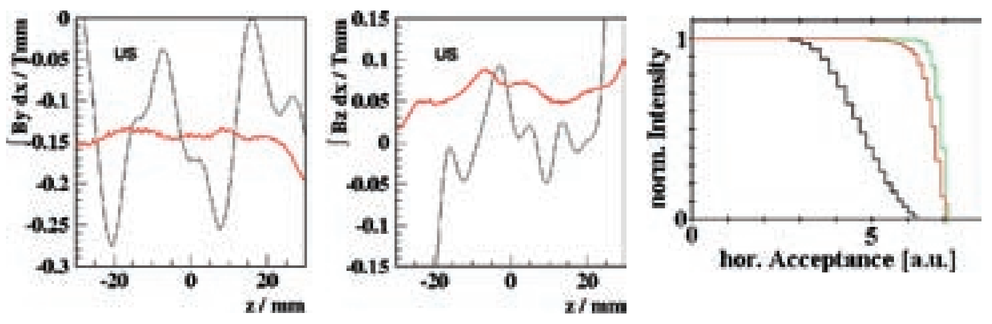

Fig. 2:
Measured integrated field integrals before (black) and after (red) re-shimming of the upstream part of the UE56-2 as a function of the horizontal coordinate. The third plot shows in the same colors the remaining beam intensity after single horizontal kicks with increasing strength were applied. Without losses, the beam can be kicked to much larger amplitudes after re-shimming. For comparison the situation without ID is shown in green.

Topping-up

Research and development concentrated on the planned topping-up mode in which lost electrons are replaced by injecting beam as soon as the current has dropped below a certain level. This mode would improve the brilliance by keeping the current constantly high and could reduce optics distortions in the beamline related to time-varying heat loads on the optical components. However, electrons would have to be injected with the beam shutters open. Therefore, the injection efficiency should be close to 100 % in order to keep radiation levels at the experimental stations sufficiently low, under all possible operating conditions.

In order to achieve this high injection efficiency with the required reliability, we adjusted the injection kicker magnets to make the individual pulse shapes as equal as possible.

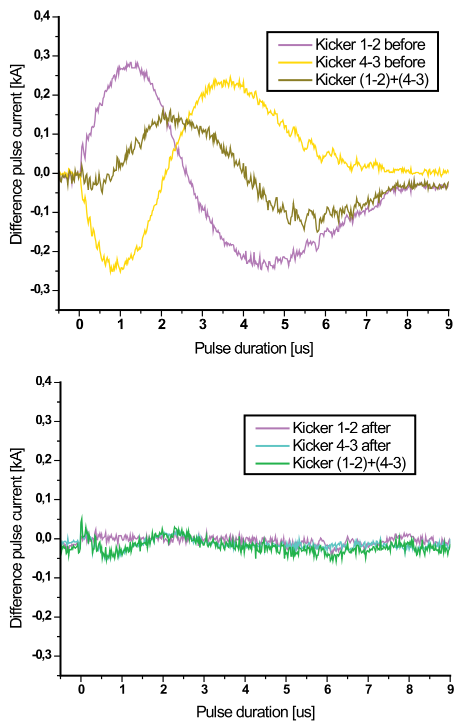

Fig. 3:
Pulse mismatch between the two pairs of injection kicker pulses with opposite polarity, top: before and bottom: after adjustment of the pulse shapes. The larger the mismatch the more beam motion is induced during the injection process and the stronger is the impact of IDs.

The timing of these four pulses could be improved considerably. With carefully adjusted kicker magnets (Fig. 3) the typically 50 ms lasting injection transients on the horizontal beam position can be made as small as a fraction of a mm. However, the beam moves vertically with a damped amplitude of initially 1 mm. With the adjusted kicker magnet pulses the injection efficiency is less dependent on the gaps of insertion devices and the injection efficiency is improved for the injection of single bunches. The efficiency for longer bunch trains remains around the 80 % level indicating that other effects still have to be investigated.

Finally, we installed sets of collimators in the transfer line between synchrotron and storage ring in order not to spread losses from injected particles all around the storage ring. These collimators will prevent particles in the tail or halo of the injected beam from entering the radiation sensitive ring area. We expect that all these measures will eventually lead to the required injection efficiency.

Regular operation in topping-up mode is envisaged to start by the end of 2007. Users will only be able to take full advantage of this mode if their data taking process or their detectors can be blanked out during the injection process. Otherwise the quality of the experimental data might be deteriorated due to the unavoidable beam motion in connection with the topping-up injections.

Beamline Developments

After seven years of successful operation and an ambitious development program to increase both the number and the performance of available beamlines, maintenance and improvement of the existing equipment becomes more and more important.

With the optimization of the electron beam performance concerning size and stability, the influence of residual field inhomogeneities of the insertion devices became more and more noticeable. By re-shimming of several undulators the field variation in the plane perpendicular to the electron beam could be reduced by about a factor of ten, resulting in a significantly reduced impact on electron beam life time as already mentioned.

To some extent the beamline control system seemed to develop to a never ending story, since the number of interrupts caused by crashes of computer hard- or software or erroneous operation of the data acquisition programme increased during the year. A dedicated task force was established to concentrate on that special problem, and within a short time some soft- and hardware bugs could be fixed. The first action taken was the modification of the existing beamline control system to run much more stable. Parallel to this, it is our aim to develop a new control system, which then will act as an interface between the user and the hardware required to generate monochromatic light with a certain polarization on the user's sample.

At the beginning of 2005, BESSY has taken on responsibility for beamline 14.1, being one of three beamlines of the former Protein Structure Factory (PSF).

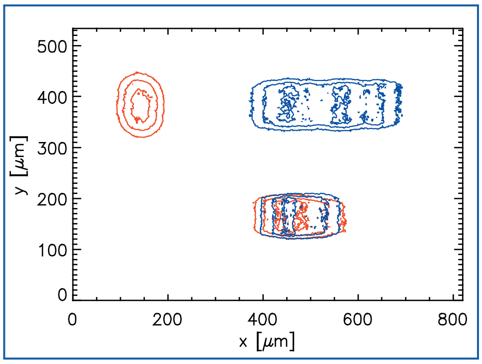

Fig. 4:
Focus of the UE56-2 PGM-1

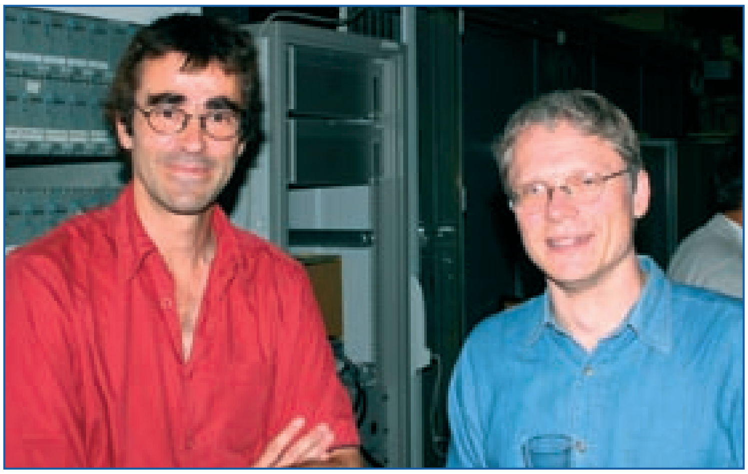

Fig. 5:
Official inauguration of the μ-Spot beamline

To improve the working conditions at the beamlines and to make them competitive to other synchrotron radiation facilities an upgrade programme was initiated including a new SPINE-pin compatible sample cooling system, a large CCD array detector and the implementation of a highly standardized automated sample handling.

New beamlines

During the fall shut down the UE56-2 PGM-1, operated by the MPG, got a new design. Three optical elements were replaced to deliver a spot size for the double-beam-operation of 62 μm by 13 μm (Fig. 4). As a side effect, the carbon contamination of the optics could be completely removed.

The new microfocus beamline (μSpot) at the BAM-WLS was commissioned in summer last year. A spot size of 20 μm x 25 μm (horizontal x vertical) was obtained with a photon flux of $7 \times 10^8\ \mathrm{s}^{-1}\ 100\ \mathrm{mA}^{-1}$ at an energy of 9 keV. While the horizontal spot size already meets the specification, the vertical spot size is out of specs by a factor of about two, indicating that the bimorph mirror requires further tuning (Fig. 5).

Since the end of 2005, a new high-transmission Bragg-Fresnel monochromator is available for the fs-slicing activities. The only optical element of this beamline is a Bragg-Fresnel lens operated in reflection geometry, delivering a transmission of up to 6.5% at an energy resolution of about 1,000. Three lenses are available designed to investigate the 2p-edges of Fe, Co and Ni.

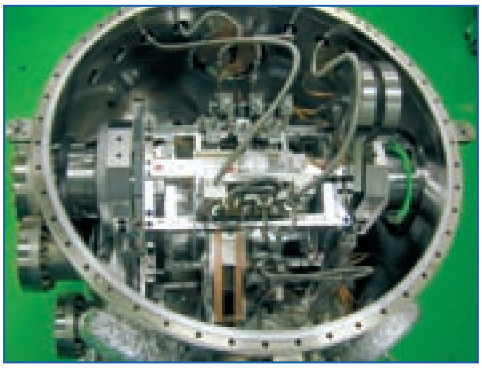

Fig. 6:
UE112 PGM vacuum chamber – open secret. (Source: FMB GmbH, Berlin)

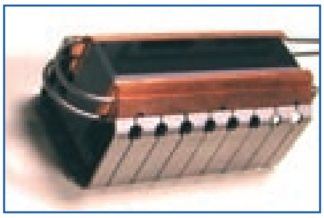

Fig. 7:
Optical element in its holder with additional cooling plates attached

As a spin-off product of the fs-slicing activities, a new beamline dedicated for the Far Infrared (THz) region was successfully commissioned, operating in the spectral range between 50 GHz and 4.5 THz. The beamline accepts synchrotron radiation from a bending magnet source close to the interaction region of a femtosecond laser of 30-50 fs pulse length with the electron bunch. Edge radiation as well as the regular bending magnet fan can be accepted. The beamline was tailored for diagnostics and experiments employing coherent synchrotron radiation (CSR) from regular and compressed bunches as well as from a laser-induced femtosecond density modulation. Users who will work with a naturally synchronized fs-laser and polarized coherent fs-THz pulses up to 3 THz may benefit from commercial FTIR equipment (VERTEX 70, Bruker), a Martin-Puplett spectrometer, two fast InSb bolometers, a 4.2 K Si-bolometer and other detectors.

One year after the installation of the UE49, an elliptical undulator filling the last available straight section L08 of the storage ring, the corresponding plane grating monochromator could be commissioned. The monochromator offers two branch lines. Branch line A is designated for experiments using the new spin polarized photoemission microscope (SPEEM), offering a final lateral resolution of about 200 nm (20 nm without spin polarization). Branch line B will provide synchrotron light for the SMART, offering a final lateral resolution of 2 nm. Photon flux and energy resolution are as specified. The final installation of the refocusing optics (elliptical mirrors in both cases) is under way and will be finished early in 2006.

With the UE112-PGM another new beamline is under construction. Since this instrument covers the energy range from 5 – 300 eV, the incidence angles at the optics have to be varied between normal (nearly visible light) and gracing (XUV-range), requiring a large turning range of the grating. To fulfil these mechanical requirements, mirror and grating drives had to be implemented inside the chamber, so that both actuation and position encoding are performed under UHV conditions (Fig. 6).

Metrology

To further improve the performance of optical elements, metrology and precision engineering were merged. The aim is to study the behaviour of the performance of an optical element if its holder with or without additional cooling plates is attached (Fig. 7). It could be demonstrated that the surface performance is significantly reduced when mounting an optical element in its holder, but that the effect can be retracted by proper modifications of the holder (Fig. 8). In addition, first experiments were performed to determine the behaviour of a grating being cooled with liquid nitrogen. Not surprisingly, it showed up that oxygen is deposited on the grating surface if its temperature is below the condensation temperature.

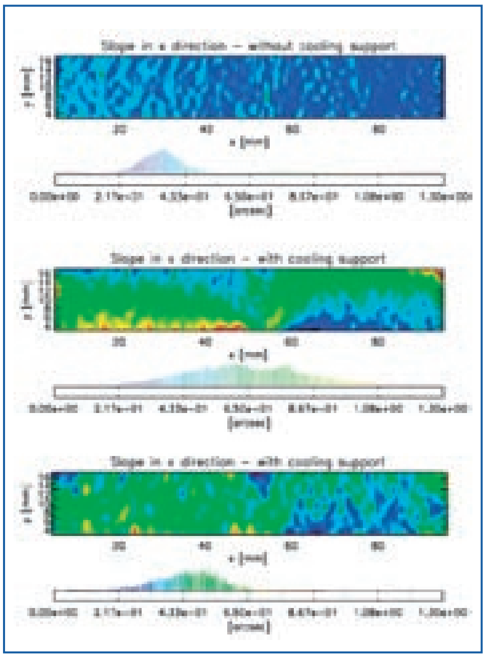

Fig. 8:
Mirror distortion upon mounting in its holder (a, b) and retraction of distortion by careful modifications of the holder (c)

Contact:
Christian Jung
christian.jung@bessy.de

The Metrology Light Source of the PTB

Status of the construction

The construction of the PTB low-energy electron storage ring Metrology Light Source (MLS) in the neighbourhood of BESSY is proceeding well. The building at Magnusstraße 9, is almost completed and will be handed over to PTB in spring 2006 (Fig. 1).

The storage ring itself, being planned and constructed by BESSY under contract of PTB, is also developing according to plan:
All major components have been designed and ordered. The magnet girders have already been delivered. The delivery of the storage ring magnets, produced by the Budker Institute of Nuclear Physics (BINP) in Novosibirsk (Russia), is scheduled for March 2006 and the injection microtron, fabricated by Danfysik A/S in Jyllinge (Denmark), will arrive in April 2006. Start of machine commissioning will be 2007, user operation is scheduled to begin in 2008.

Fig. 1:
The building accommodating the Metrology Light Source (a) and a view of the experimental hall with the storage ring bunker (b), at January 9th, 2006.

Planned Beamlines

The front end systems and many of the beamlines are already projected (Fig. 2) and first parts have been ordered. In a first stage a total of 5 front ends, including a diagnostic front end, and the IR and THz beamlines will be set up before the start of storage ring commissioning.

The planned beamlines will cover the spectral range from the FIR up to 300 eV with monochromatized bending magnet radiation. Also undispersed, calculable bending magnet radiation will be available at one beamline for the calibration of energy-dispersive detectors and radiation sources. The undulator U180, which had been operated at the BESSY storage ring for years up to its replacement by a U49 undulator, will be installed at the MLS after it has undergone a substantial renewal. The undulator will then deliver radiation to a monochromator beamline designed for the 3 eV up to 300 eV spectral range.

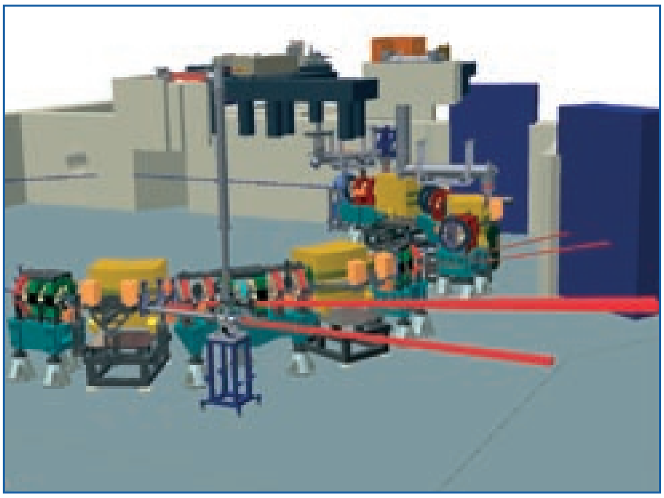

Fig. 2:
Artist view of the planned IR- and THz beamlines.

Contact:
Roman Markus Klein
roman.m.klein@ptb.de

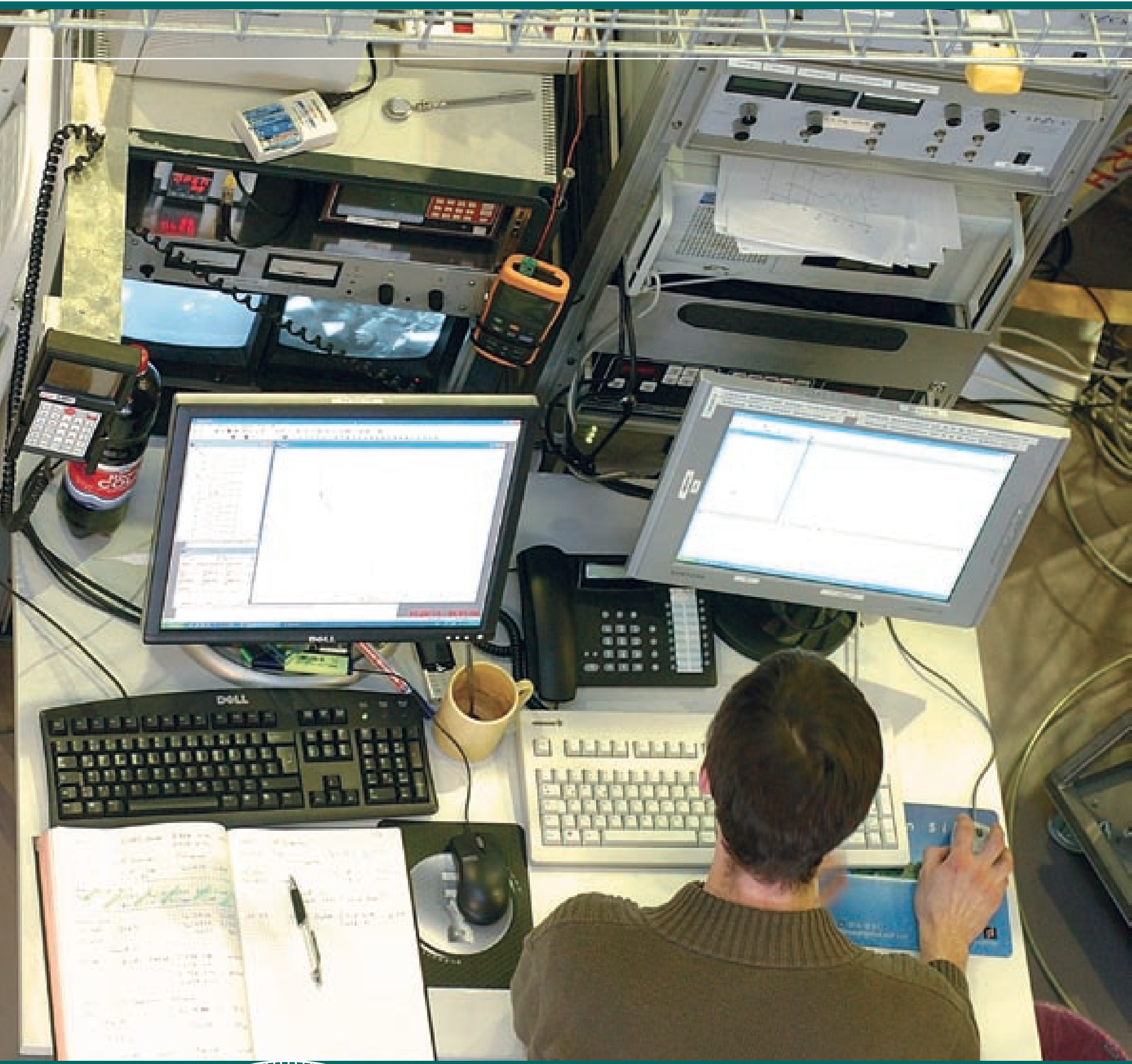

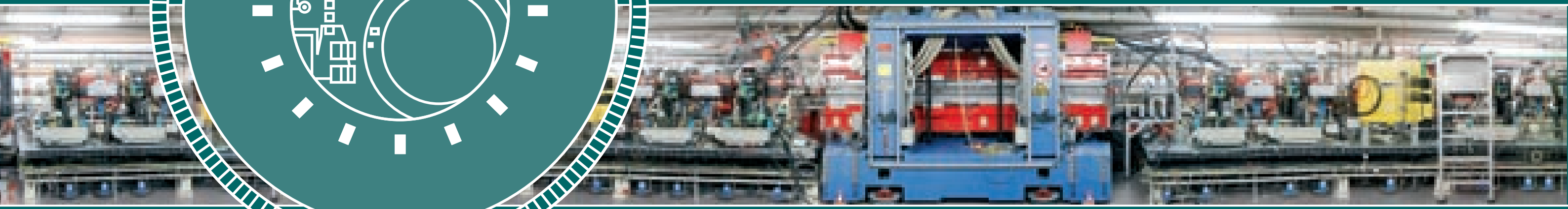

Operation Statistics

The 38 operation weeks sum up to a total of 5251.8 operation hours with 33 multi-bunch weeks, 4 single-bunch weeks and one low-α week. Additional 7 M/C weeks of 931 operation hours were available for machine studies, ID- and beamline commissioning.

Of the time devoted to user operation almost 8,000 shifts (8 hours each) at ID-beamlines and 6,035 shifts at dipole-beamlines were provided according to the beamtime calendar. The distribution among the different user categories is as indicated in the graphics. The proprietary projects within the AZM are not included.

These shifts have been distributed among 654 user runs (without PTB-projects) resulting in 18.75 shifts per user run. Due to the increased number of hard X-ray experiments (PX, 7T-MPW, BAMline) with their less time consuming set-up procedures the number of projects has increased, whereas the average beamtime per user run was reduced compared to previous years.

In 2005 more than 1,300 external scientists carried out their research projects at BESSY, among them, almost 20% from EU countries funded by EU-I3 programme and researchers from biology and life sciences now make up almost 10% of the users.

Beamtime at BESSY

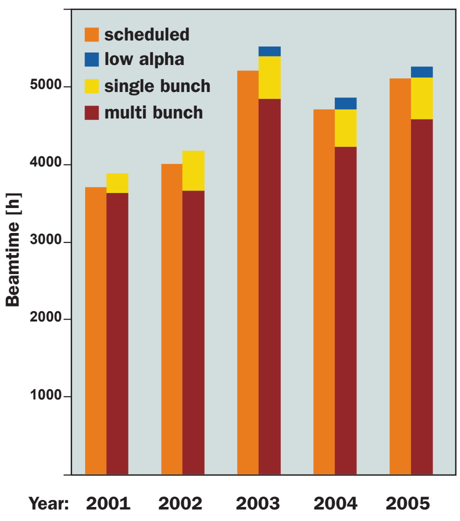

Main Research Areas

Number of Projects

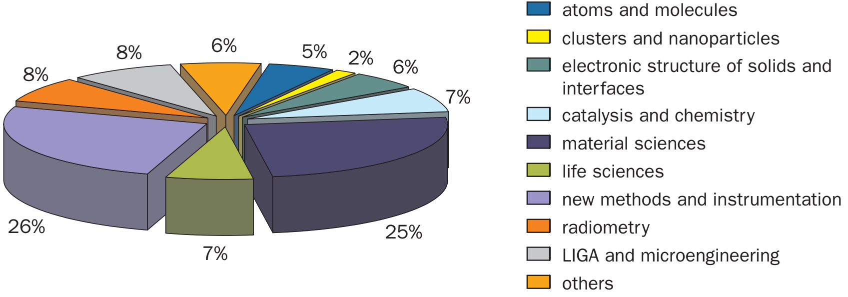

Beamtime allocation in 2005

Insertion Device Beamlines

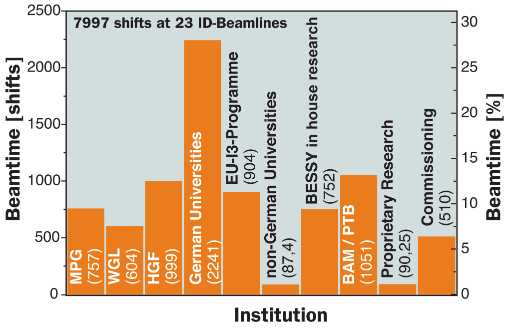

Dipole Beamlines

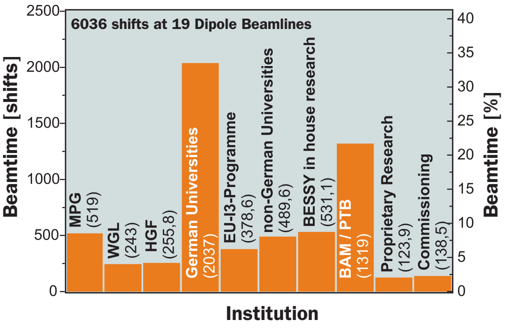

MPG = Max-Planck-Gesellschaft

WGL = Leibniz-Gemeinschaft

HGF = Helmholtz-Gemeinschaft

BAM = Bundesanstalt für Materialforschung und- prüfung

PTB = Physikalisch-Technische Bundesanstalt

Improvements for users

The new weekly schedule introduced with the start of user operation in January 2005 has improved both service work of the BESSY staff and working conditions for our users. To remind you, the rotation of user groups can take place on Monday, and measuring time is available without interruption from 7 am Tuesday till 10:30 pm Sunday. This change encouraged us to develop the beam time schedule on that basis of three shifts every day (7 am – 3 pm, 3 pm – 11 pm, 11 pm – 7am next morning) and to implement an additional operational mode beside multi-bunch-hybrid and single bunch operation.

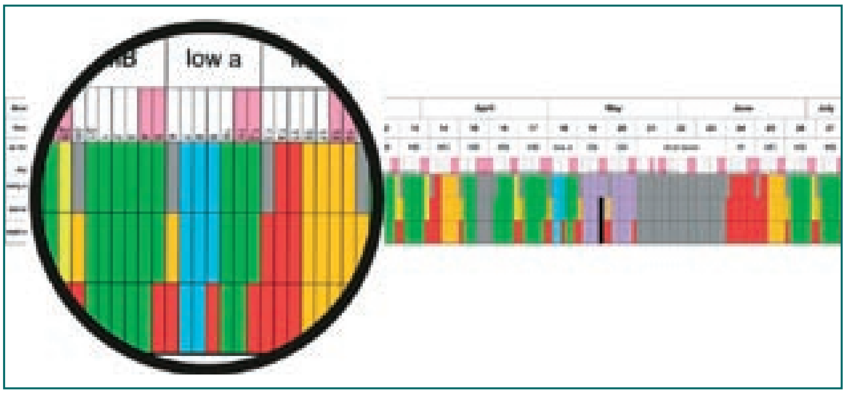

Fig. 1:
The low-α shifts (blue) in the beamtime schedule

Regular low-α beam time

In order to encourage a new user community to perform experiments on a picosecond time scale, we offer special low-α beam time for one week every quarter of the year. The beam time starts on Tuesday morning at 7 am and lasts until Thursday 11 pm. The following night shift will be used to switch back to normal user operation, which than starts on Friday 7 am. Two low-α weeks are directly linked to the single bunch shifts allowing for setting up the experiment if required (Fig. 1).

New 'Info System'

Besides the 'Hallendienst', the 'Info System' is the key player to keep our users informed about the status of the machine and what is going in the experimental area. Since this information system has been developed already a decade ago, the electronics group has revised the system completely. By the end of the fall shut down in 2005, the new 'Info System' was launched. The most important difference with respect to the old system is that the information on support and next injection is available at any time, scrolling at the bottom line of the display. Since the early days of user operation at BESSY, the history of the beam current stored in the ring over the past 4 hours is displayed. This information is completed by further relevant announcements, being sorted in categories for short term (red) and long term (blue) messages as well as for announcements related to radiation safety (yellow). Some times, the way to get the information is as important as the information itself. We thus offer different access channels to the relevant announcements:

- Monitors throughout the BESSY buildings
- Internet via infosystem.bessy.de
- Internet via messaging system RSS-feed (not yet Microsoft)
- Java-applet
- Mobile phone (WAP)

With the latter, information on the operation status of the storage ring can be obtained from anywhere.

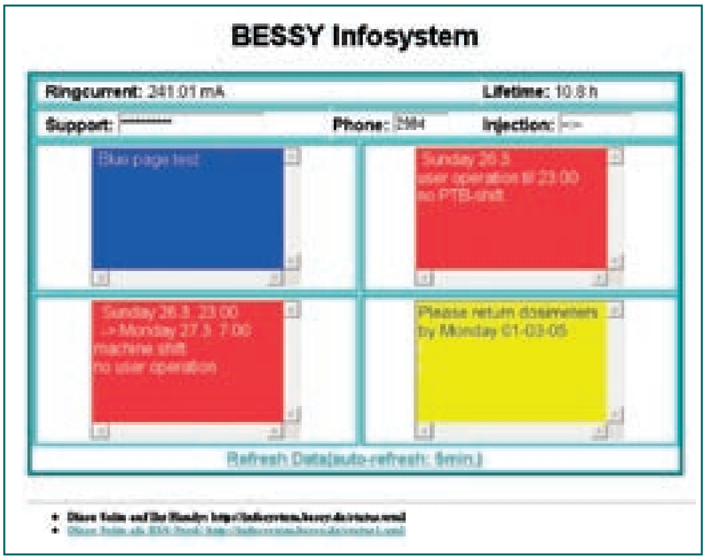

BESSY Infosystem

Ringcurrent: 241.01 mA **Lifetime:** 10.8 h

Support: ---------- **Phone:** 2584 **Injection:** --

Blue page test

Sunday 26.3
user operation til 23.00
no PTB-shift

Sunday 26.3. 23.00
-> Monday 27.3. 7.00
machine shift
no user operation

Please return dosimeters
by Monday 01-03-05

Refresh Data(auto-refresh: 5min.)

Fig. 2:
The new BESSY Info System
(infosystem.bessy.de)

Interactive safety instructions

Accidents don't just happen – they are caused. This is the central statement of the new interactive safety instructions available since the beginning of 2006. The instructions can be attended at any time after your arrival at BESSY, preferably before the experiments begin, and they have to be repeated once every twelve months. They consist of a compulsory part, covering general regulations as well as radiation protection, and they close with some tasks to be answered accordingly. In addition, modules are available if users are going to use lasers or liquid helium or if activities in the mechanical workshop or the chemical laboratory are planned. The complete instructions require about 40 minutes. The information presented in the instructions is also available via the BESSY home page (see 'user information' or directly at *www.bessy.de//safety/01_ueberblick_e.htm*). This might be of interest if questions concerning the handling of hazardous substances and/or dangerous equipment arise while preparing beam time.

BOAT News

The BESSY Online Access Tool BOAT went online, and the allocation of beam time for the first semester 2006 has been successfully carried out. By the end of the year additional features like overview of scheduled beam time for each proposal, online confirmation, allocation notes in PDF-format, overview of all required documents for each beamtime (including database supported safety declaration) and their respective status were implemented.

User Committee

Ralph Püttner (Chairperson)
Freie Universität Berlin

Birgit Kanngießer (Vice-Chairperson)
Technische Universität Berlin

Peter Baumgärtel
Universität Potsdam

Wolfgang Braun
Paul Drude Institut

Ralf Feyerherm
Hahn-Meitner-Institut

Fig. 3:
Starting page of the interactive safety instructions

Experimental hall reshuffling

In preparation of building the catalysis beam line ISISS of the Fritz-Haber-Instiue at the segment used by the Max-Planck-Society, the lifting tools for heavy loads had to be moved from their former place. Now, they are located more central than before at the heavy load entrance of the storage ring hall.

In this area, users of the µSpot- , the IR- and microscopy beam lines will also have access to the laboratory for biological samples. This new laboratory is a service mainly for users dealing with biological samples. It provides instruments for handling eukaryotic cells and will be available by the end of spring 2006.

ID Beamlines at BESSY (January 2006)

Further information on beamlines can be found on the 'user info pages' of the BESSY website

BAM
Bundesanstalt für Materialforschung und -prüfung

BTUC
Brandenburgische Technische Universität Cottbus

FUB
Freie Universität Berlin

FZJ
Forschungszentrum Jülich

HMI
Hahn Meitner Institut

Uni Gö
Universität Göttingen

MPG
Max Planck Gesellschaft

MPIKG
Max Planck Instiut für Kolloid und Grenzflächenforschung

PDI
Paul Drude Institut

ID	Monochromator	Energy range (eV)	Operated by	Contact Persons	
7T-WLS-1	KMC	6 k - 50 k	BAM/PTB	H. Riesemeier (BAM) B. Müller (BAM)	A. Erko
	µSpot	2 k - 30 k	BAM/MPIKG	H. Riesemeier (BAM) O. Paris (MPIKG)	A. Erko
U125-2	SGM	20 - 500	BUS	R. Püttner (FUB)	G. Reichardt
	KMC	6 k - 12 k	PDI/HUB	W. Braun (PDI P. Jenichen (PDI)	A. Erko
	10m-NIM	< 10 - 35	Uni KI/BESSY	G. Reichardt	I.Packe
7T-MPW	direct beam	3 k - 60 k	HMI	Ch. Genzel (HMI) I. Denks (HMI) G. Wagener (HMI)	A. Erko
	KMC	3 k - 60 k	HMI	E. Dudzik (HMI) R. Feyerherm (HMI) G. Wagener (HMI)	A. Erko
UE56-2	PGM 1	60 - 1,300	MPG	W. Mahler (MPG) B. Zada (MPG)	
	PGM 2	60 - 1,300	MPG	W. Mahler (MPG) B. Zada (MPG)	
6T-WLS 0.4T-LFD	Litho	> 2 k	BESSY	B. Löchel H.-U. Scheunemann	M. Bednarzik H. Köhrich
U49-1	-	direct beam	PTB	R. Klein (PTB)	
	13°		PTB	R. Klein (PTB) A. Gottwald (PTB)	
	PGM	20 - 1,900	PTB	B. Beckhoff (PTB	
UE49	PGM a/b	85 - 1,600	BESSY	F. Senf Ch. Jung	M. Mast J.-S. Schmidt
UE52	SGM	85 - 1,600	BESSY	K. Godehusen F. Senf	T. Zeschke
	PGM	85 - 1,600	Uni Wü	D. Batchelor (Uni Wü)	Ch. Jung
UE46	PGM	120 - 1,700	HMI	D. Schmitz (HMI) H. Rossner (HMI)	F. Senf
UE56-1	PGM a	60 - 1,300	BESSY	T. Kachel J.-S. Schmidt	Ch. Stamm
	PGM b	60 - 1,300	BESSY	T. Kachel J.-S. Schmidt	T. Zeschke
	ZP-mono	715 / 786 / 861	BESSY	A. Erko	I. Packe
	SGM	60 - 1,300	FZJ	S. Cramm (FZJ)	
U41	STXM	~250 - ~600	Uni Gö/BESSY	P. Guttmann (Uni Gö)	G. Schneider
	TXM	~250 - ~600	Uni Gö/BESSY	P. Guttmann (Uni Gö)	G. Schneider
	PGM	170 - 1,800	BESSY	Ch. Jung	M. Mast
U125-1	PGM 1	20 - 700	BESSY	O. Schwarzkopf	F. Eggenstein
	PGM 2 a/b	5 - 180	BESSY	R. Follath	J.-S. Schmidt
7T-WLS-2	KMC 1	4.5 k - 17.7 k	BESSY	U. Müller	
	KMC 2	4.5 k - 17.7 k	FUB	M. Fieber-Erdmann (FUB)	
U49-2	PGM 1	85 - 1,600	BESSY	O. Schwarzkopf	J.-S. Schmid
	PGM 2	85 - 1,600	BTUC	P. Hoffmann (BTUC)	W. Braun

Dipole Beamlines at BESSY (January 2006)

Further information on beamlines can be found on the 'user info pages' of the BESSY website

Monochromator	**Energy Range (eV)**	**Operated by**	**Contact Persons**	
Litho EUV	95	BESSY	H.-U. Scheunemann	H.Köhrich
KMC-1	1.7 k - 10 k	BESSY	F. Schäfers	M. Mertin
IR stations	Thz - 0.5	BESSY	U. Schade	
Litho	direct beam	BESSY	B. Löchel H.-U. Scheunemann	M. Bednarzik
1m-NIM 1	3 - 35	PTB	M. Richter (PTB)	
1m-NIM 2	3 - 35	PTB	R. Thornagel (PTB)	
	white beam	PTB	R. Thornagel (PTB)	
KMC	1.7 k - 10 k	PTB	M. Krumrey (PTB)	
PGM	30 - 1,800	PTB	F. Scholze (PTB)	
HE-SGM	200 -700	CRG	A. Lippitz (BAM)	O. Schwarzkopf
Optics-BL	20 - 2,000	BESSY	F. Senf	
KMC 2	4.5 k - 15 k	BESSY	A. Erko	I. Packe
PGM 3	20 - 1,900	BESSY	T. Kachel	F. Eggenstein
3m-NIM	4 - 35	BESSY	I. Packe	G. Reichardt
EDR	2 k - 12 k	Uni P	W. Leitenberger (Uni P) Y. Bodenthin (Uni P)	A. Erko
TGM 4	8 - 120	BESSY	K. Godehusen	M. Mast
TGM 7	8 - 120	HMI	C. Pettenkofer (HMI) W. Bremsteller (HMI)	
PGM-RD-BL	30 - 1,500	Uni Pet	Y. Dedkov (Uni DD) S. Molodtsov (Uni DD)	
CP-NIM	4 - 35	BESSY	F. Schäfers	M. Mertin

PTB
Physikalisch Technische Bundesanstalt

HUB
Humboldt-Universität Berlin

FUB
Freie Universität Berlin

Uni P
Universität Potsdam

BAM
Bundesanstalt für Materialforschung und -prüfung

HMI
Hahn Meitner Institut

Uni DD
Universität Dresden

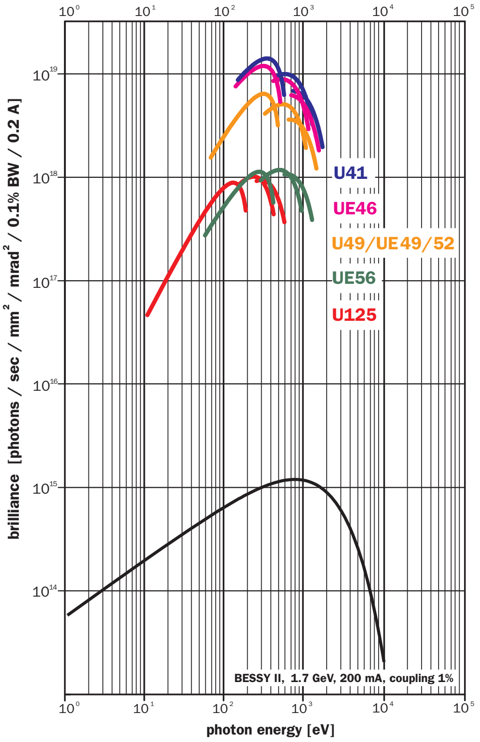

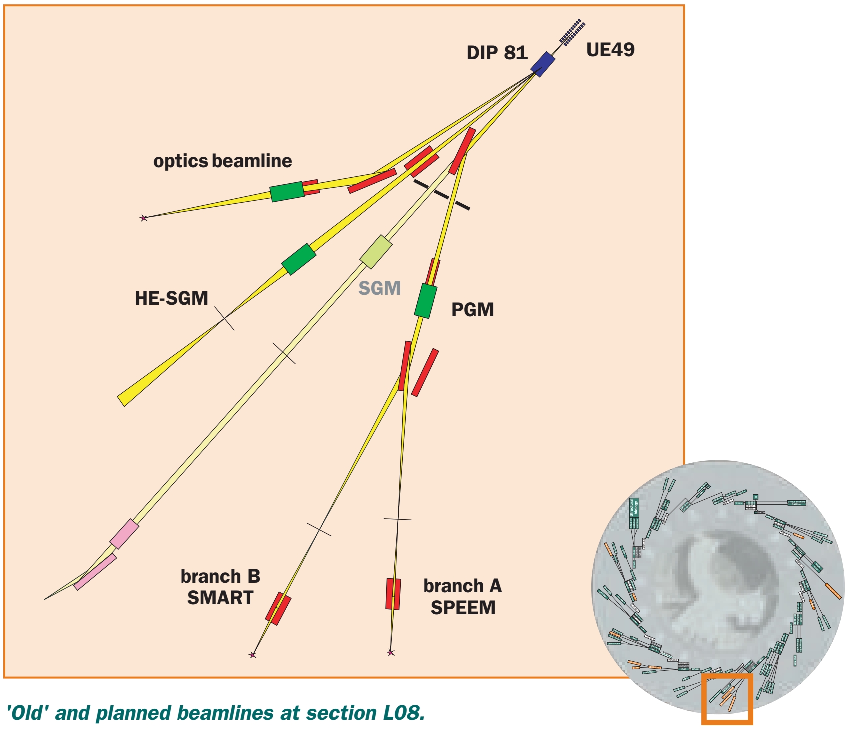

'Old' and planned beamlines at section L08.

Experimental Stations


Protein crystallography station at 7T-WLS–2.

As a dedicated third generation synchrotron radiation source, we offer unique opportunities for a large variety of experiments, covering orders of magnitude in both lateral/spatial and time resolution. To fully exploit these opportunities, BESSY's user community can roughly be devided into three categories.

- Based on BESSY’s history, a large group of users has developed their own, science driven equipment to make use of the performance of the beamlines supplied by BESSY. For these user user groups the close contact with the responsible beamline scientist guarantees to find the beamline offering optimal performance for the experiments to be carried out.
- To facilitate those scientists access to the use of synchrotron radiation, who do not have particular instrumentation on-hand, BESSY offers a variety experimental stations. These instruments are operated either by BESSY or by user groups, the latter often being funded by different institutions. As can be seen from table 1, most of these instruments allow for photoelectron spectroscopy measurements, being one of the key areas of BESSY. During the discussion with the beamtime coordinators at BESSY, the optimal combination of beam line and experimental station can be selected to meet the users requirements.
- While the first two categories express BESSY’s original mission of supplying beamlines, the third category is based on the growing demand of sophisticated state of the art end stations for experiments requiring a very high technical complexity. These instruments need to be permanently installed at a dedicated beamline – a beamline, which is tailor-made to fully meet the experiments requirements. The combination of beamline and endstations also covers storage and retrieval of the experimental data. Table 2 gives an impression of the variety of instruments already available.


Experimental station on the move.


Infrared microscope is also available for achaeometry.

The performance of the instrumentation at BESSY is subject to permanent improvement, which also includes the development of new beamlines and experimental stations. The success of this work can clearly be seen from the list of contributions to the highlights during the past years, because experiments from the latter two categories play a dominant role in this respect.

All our experienced or potential users are thus advised to contact BESSY when planning experiments to ensure that the optimal combination of instruments can be selected to guarantee a successful work.

Contact:
Christian Jung
christian.jung@bessy.de

Permanent experimental stations

Experiment	Contact	Location
THz spectroscopy$^{\mathrm{BioSR,\ Ind}}$	holldack@bessy.de	IR
IR-spectroscopy and -microscopy$^{\mathrm{BioSR,\ Ind}}$	schade@bessy.de	IR
IR ellipsometry$^{\mathrm{Ind}}$	hinrichs@isas-berlin.de	IR
UVIS - protein circular dichroism spectroscopy$^{\mathrm{BioSR}}$	baumgaer@rz.uni-potsdam.de	3m-NIM
SURICAT - photoelectron and absorption spectroscopy	antje.vollmer@bessy.de	optics beamline
Two-Photon-Photoemission Experiment	weinelt@mbi-berlin.de	U125-1 PGM-2
SAMIC - spectroscopy and microscopy integrating chamber$^{\mathrm{Ind}}$	patrick.hoffmann@tu-cottbus.de	U49-2 PGM-2
SPEEM - spin resolved photoemission microscopyplanned	florian.kronast@bessy.de	UE49 PGM a
SMART - spectro-microscope with highest spatial resolution	thomas.schmidt@physik.uni-wuerzburg.de	UE49 PGM b
Reflectometry$^{\mathrm{Ind}}$	schaefers@bessy.de	optics beamline
XM - X-ray Microscopy$^{\mathrm{BioSR,\ Ind}}$	guttmann@bessy.de	U41-XM
EUV lithography$^{\mathrm{Ind}}$	loechel@bessy.de	DIP 01
X-ray lithography$^{\mathrm{Ind}}$	loechel@bessy.de	6T-WLS, DIP 06
HIKE- Hard X-ray high kinetic energy photoelectron spectroscopy	mihaela.gorgoi@bessy.de	KMC-1
X-ray diffraction during MBE	braun@pdi-berlin.de	U125-2 KMC
µSpot micro-XANES, -EXAFS, -fluorescence$^{\mathrm{BioSR}}$	erko@bessy.de	7T-WLS-1
Diffraction, XANES, EXAFS	erko@bessy.de	KMC-2
Protein crystallography$^{\mathrm{BioSR,\ Ind}}$	umue@bessy.de	7T-WLS-2
BAMline - nondestructive testing in analytical chemistry$^{\mathrm{Ind}}$	heinrich.riesemeier@bam.de	7T-WLS-1
EDDI - energy dispersive diffraction	genzel@hmi.de	7T-MPW
MagS - resonant magnetic scattering	feyerherm@hmi.de	7T-MPW

Variable experimental stations

Experiment	Contact
HIRES - high resolution electron spectrometer	rader@bessy.de
PHOENEXS - photoemission and near edge X-ray spectroscopy	varykhalov@bessy.de
MUSTANG - multi-user stage for angular resolved photoemission	gavrila@bessy.de
High resolution spinpolarisation photoelectron spectroscopy	c.m.schneider@fz-juelich.de
Stored Nano Particels	ruehl@phys-chemie.uni-wuerzburg.de
So-Li-AS - solid-liquid-analysis system	mayerth@surface.tu-darmstadt.de
VUV/XUV ellipsometry$^{\mathrm{Ind}}$	esser@isas-berlin.de
Scattering experiments in the VUV/XUV-range	eugen.weschke@physik.fu-berlin.de
Photoemission microscope for ps time resolved spectroscopy $^{\mathrm{Ind}}$	schoenhe@mail.uni-mainz.de
EUV-lithography$^{\mathrm{Ind}}$	scheunemann@bessy.de
MPG Catalysis Beamline $^{\mathrm{planned}}$	knop@fhi-berlin.mpg.de
Soft X-ray emission spectrometer	anna.zimina@ bessy.de
CISSY - CIS- diagnostic using Synchrotron radiation	cissy@hmi.de
ROSA - rotateable spectrometer apparatus	szargan rz.uni-leipzig.de
Fluorescence spectroscopy$^{\mathrm{Ind}}$	ruediger.mitdank @ physik.hu-berlin.de
Polarimetry	schaefers@bessy.de

BioSR: suitable for biological samples

Ind: suitable for industrial users

planned: under construction

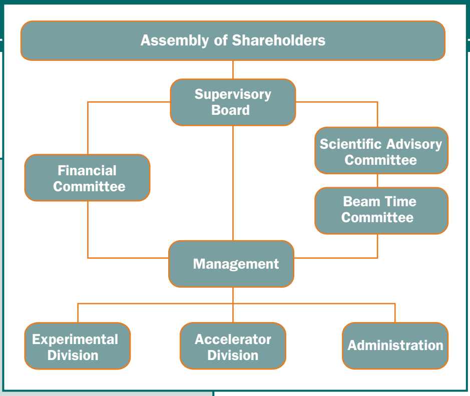

Supervisory Board:

Prof. Dr. J. Treusch (Chairman)	Forschungszentrum Jülich
Prof. Dr. E. Umbach (Vice-Chairman)	Universität Würzburg
Frau Dr. B. Vierkorn-Rudolph	Bundesministerium für Bildung und Forschung
Prof. Dr. E. O. Göbel	PTB Braunschweig
Prof. Dr. R. Maschuw	Forschungszentrum Karlsruhe
Prof. Dr. H. Braun	Max-Planck-Gesellschaft München
Frau Dr.Ulrike Gutheil	Technische Universität Berlin
Prof. Dr. J. Schneider	DESY Hamburg
Dr.-Ing. P. Szent-Ivanyi	Bundesministerium für Wirtschaft und Arbeit, Berlin
Prof. Dr. M. Steiner	HMI Berlin
Senatsdirig. W. Eckey	Senatsverwaltung für Wissenschaft, Forschung und Kultur

Scientific Advisory Committee:

Prof. Dr. Robert Schlögl (Chairman))	Fritz-Haber-Institut der MPG Berlin
Prof. Dr. E. Joseph Nordgren (Vice-Chairman)	Universitet Uppsala
Prof. Dr. Vlasta Bonacic-Koutecký	Humboldt Universität zu Berlin
Prof. Dr. Reinhard Brinkmann	DESY Hamburg
Prof. Dr. Thomas Elsässer	Max-Born-Institut Berlin
Prof. Dr. Adam Hitchcock	McMaster University Hamilton, Ontario
Priv.-Prof. Dr. Ilme Schlichting	Max-Planck-Institut für medizinische Forschung Heidelberg
Dr. Neville Smith	ALS Berkeley (Institutional Member)
Prof. Dr. Hans-Peter Steinrück	Universität Erlangen-Nürnberg
Prof. Dr. Metin Tolan	Universität Dortmund
Prof. Dr. Günther Tränkle	Ferdinand-Braun-Institut für Höchstfrequenztechnik, Berlin
Prof. Dr. Joachim Ullrich	Max-Planck-Institut für Kernphysik Heidelberg
Prof. Dr. Richard Walker	Rutherford Appleton Laboratory (Diamond), Chilton

Permanent Guests

Dr. Josef Feldhaus	HASYLAB/DESY Hamburg
Prof. Dr. Raimund Gerhardt-Multhaupt	Universität Potsdam
Prof. Dr. Helmuth Möhwald	Max Planck Institut für Kolloid- und Grenzflächenforschung, Potsdam
Prof. Dr. Jürgen Richter	BMBF
Dr. Rainer Schuchhardt	Senatsverwaltung für Wissenschaft, Forschung und Kultur Berlin

Beam Time Committee

Prof. Dr. Wilfried Wurth (Chairman)	Universität Hamburg
Prof. Dr. Lorenz Singheiser (Vice-Chairman)	Forschungszentrum Jülich
Prof. Dr. Stefan Blügel	Forschungszentrum Jülich
Prof. Dr. Ralph Claessen	Universität Würzburg
Prof. Dr. Thomas Elsässer	Max-Born-Institut Berlin
Prof. Dr. Karsten Horn	Fritz-Haber Institut der MPG Berlin
Dr. Michael Meyer	Centre Universitaire Paris-Sud
Prof. Dr. Anke Rita Pyzalla	MPI für Eisenforschung Düsseldorf
Prof. Dr. Liu Hao Tjeng	Universität zu Köln
Prof. Dr. Günther Tränkle	Ferdinand-Braun-Institut für Höchstfrequenztechnik, Berlin
Prof. Dr. Hartmut Zabel	Ruhr-Universität Bochum

Sub-Committee Protein Crystallography

Prof. Dr. Ralf Ficner	Universität Göttingen
Prof. Dr. Peter Lindley	Universität Lissabon
Dr. Matthias Wilmanns	EMBL Hamburg

Financial Committee

Ass.jur. S. Lettow (Chairman)	Forschungszentrum Karlsruhe
R. Kellermann (Vice-Chairman)	Forschungszentrum Jülich
Dr. W. Buck	PTB Berlin
M. Schleier	Max-Planck-Gesellschaft München
Dr. R. Schuchardt	Senatsverwaltung für Wissenschaft, Forschung und Kultur Berlin
H. Görres	Bundesministerium für Bildung und Forschung

User Committee

Ralph Püttner (Chairperson)	Freie Universität Berlin
Birgit Kanngießer (Vice-Chairperson)	Technische Universität Berlin
Peter Baumgärtel	Universität Potsdam
Wolfgang Braun	Paul Drude Institut
Ralf Feyerherm	Hahn-Meitner-Institut

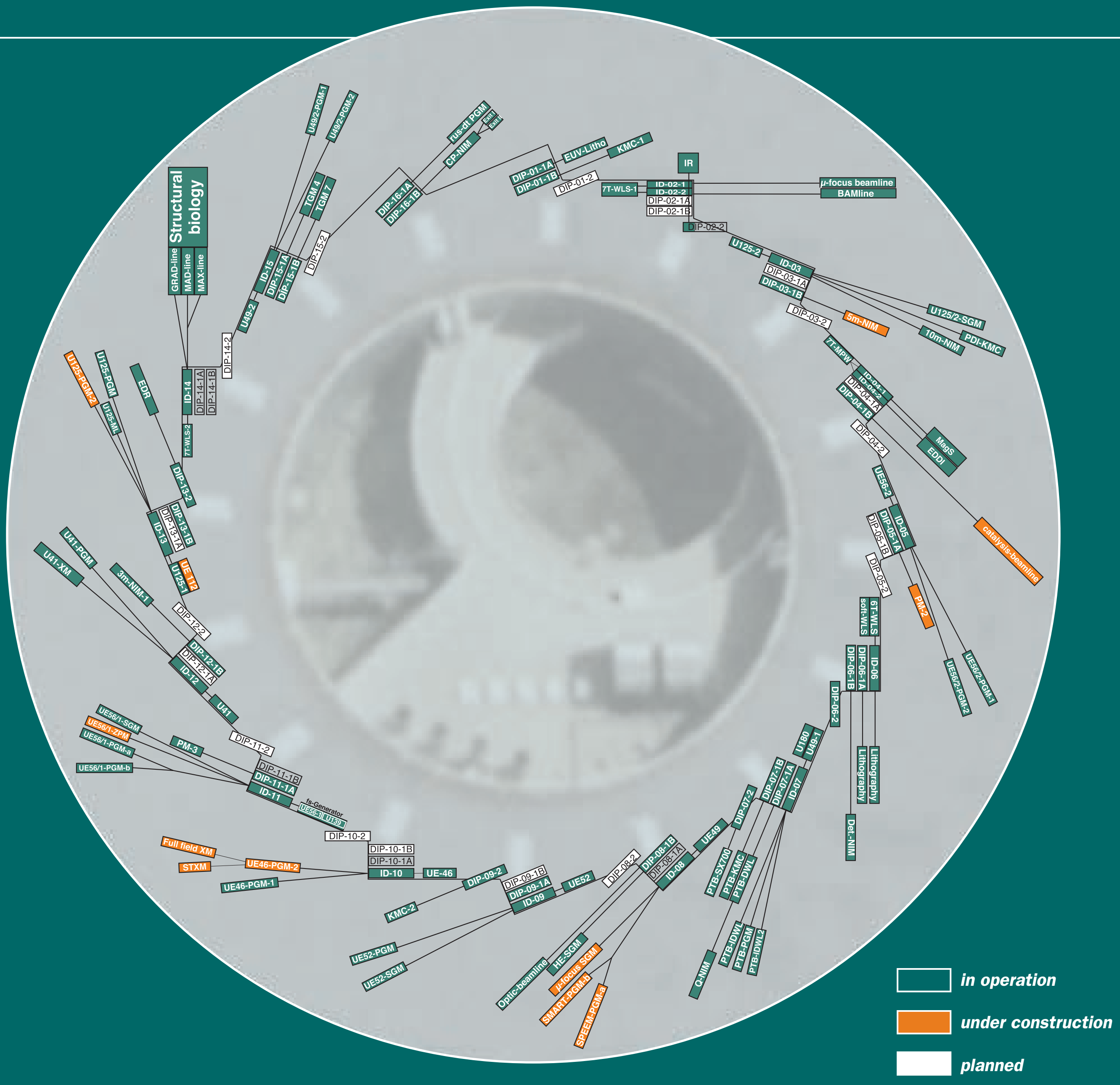

Contact

Scientific Director
Prof. Dr. Dr. h.c. Wolfgang Eberhardt
Secretary: Ines Maupetit
phone +49 (0)30 / 6392 4633
fax +49 (0)30 / 6392 2989
wolfgang.eberhardt@bessy.de,
ines.maupetit@bessy.de

Technical Director
Prof. Dr. Eberhard Jaeschke
Secretary: Dr. Nikoline Hansen
phone +49 (0)30 / 6392 4651
fax +49 (0)30 / 6392 4632
eberhard.jaeschke@bessy.de,
nikoline.hansen@bessy.de

Administration
Thomas Frederking
Secretary: Katrin Rosenblatt
phone +49 (0)30 / 6392 2901
fax +49 (0)30 / 6392 2920
thomas.frederking@bessy.de,
katrin.rosenblatt@bessy.de

Beamtime Coordination
Dr. Walter Braun, Dr. Gerd Reichardt
Secretary: Stine Mallwitz
phone +49 (0)30 / 6392 2904
fax +49 (0)30 / 6392 4673
beamtime@bessy.de

User Office
Daniela Theile, Cornelia Stürze
phone +49 (0)30 / 6392 4734
fax +49 (0)30 / 6392 4746
useroffice@bessy.de

Public Relations
Gabriele André,
Dr. Heike Henneken,
Dr. Markus Sauerborn
phone +49 (0)30 / 6392 4921
fax +49 (0)30 / 6392 4972
pr@bessy.de

Credits
For providing photographs and drawings we would like to thank:

Bernhard Schurian
Bildwerk Bers/Jankowiak
Cartoonstock.com
Chippewa Lake Water Ski Show Team
Evamaria Bohle
ESA/NASA
FMB GmbH
Hans Wiedl
Jan Röhl
Manfred E.Bayer
Paul Estrell
Physikalisch-Technische-Bundesanstalt
Raphael und Heiko Wende
Sammlung Steiner
Silko Barth
Uwe Müller
ZDF Bilderdienst

We would also like to thank Uppsala University enabling Heike Henneken to pursue her editorial work for the Highlights while staying in Sweden.